Magnetic nanoparticles: Interactions with hematopoietic cells and resulting MR imaging properties

Von der Fakultät für Mathematik, Informatik und Naturwissenschaften der RWTH Aachen University zur Erlangung des akademischen Grades eines Doktors der Naturwissenschaften genehmigte Dissertation

vorgelegt von

Diplom Ingenieur (FH), M.Sc.

Sebastian Schwarz

aus Koblenz, Deutschland

Berichter:

Universitätsprofessor Dr. Martin Zenke

Universitätsprofessor Dr. Walter Richtering

Tag der mündlichen Prüfung: 05.12.2012

Diese Dissertation ist auf den Internetseiten der Hochschulbibliothek online verfügbar

Zusammenfassung

Magnetische Nanopartikel (MNP) wurden in den letzten Jahren stetig weiter entwickelt und leisten bereits heute einen wichtigen Beitrag auf dem Gebiet der medizinischen Diagnose und Behandlung. Einsatzbereiche beinhalten sowohl "drug delivery" Systeme als auch Kontrastmittel, welche z.B. in der Magnetresonanztomographie (MRT) zum Einsatz kommen. Zellen des angeborenen Immunsystems stellen wichtige Mediatoren in sowohl der Identifizierung als auch der Beseitigung eingehender Infektionen dar und tragen merklich zur Einleitung immunologischer Wechselwege bei.

Blut-bildende Stammzellen und sich daraus ableitende Vorläuferzellen stellen wegen ihrem hohen Grad an Plastizität effektive Ziele von zell-basierenden Therapien dar. Darüber hinaus besitzen sie die Fähigkeit, den gesamten Zellpool des hematopoietischen Systems zu rekonstituieren. Auf der anderen Seite stellen terminal differenzierte Immunzellen wie z.B. Makrophagen und dendritische Zellen (DC) aufgrund ihrer immunologischen Merkmale optimale Markierungsagenzien dar. Makrophagen leisten einen besonderen Beitrag zur Identifizierung und Beseitigung eingehender Infektionen durch Unterstützung einer geeigneten Immunantwort. Professionelle Antigen-präsentierende DC spielen eine Schlüsselrolle bei der Einleitung einer primären adaptiven Immunantwort, welche in einer Antigen-spezifischen Aktivierung von B- und T-Lymphozyten in sekundären Lymphorganen resultiert. Aufgrund dieser und anderer Tatsachen stellen sie ein attraktives Ziel dar, mit dessen Hilfe zelluläre Impfstoffe und Kontrastmittel für die molekulare Bildgebung entwickelt werden können. Deshalb werden sie derzeit in vielen klinischen Studien eingesetzt.

Dennoch sind die (i) Interaktionen von magnetischen Nanopartikeln mit einer gegebenen Ziel-Zellpopulation, die (ii) Induktion eines gewünschten Zell-Phänotyps mittels gezielten Markierungsstrategien, sowohl die (ii) daraus resultierenden MNP Bildgebungseigenschaften in der MRT äußerst wichtig für den Verlauf dieser Zell-basierenden Therapieansätze. Auch wenn sie bereits zu einem gewissen Grad in klinischen Studien zur Anwendung kommen, mangelt es derzeit noch an systematischen Forschungsansätzen. Das Wissen über die grundlegenden Mechanismen der zellulären MNP Aufnahme, phenotypischen Veränderungen markierter Zellen und daraus resultierenden Bildgebungseigenschaften befindet sich noch im Anfangsstadium.

Aus diesem Grund wurden in dieser Studie synthetische MNP auf Basis von Eisenoxid entwickelt und hergestellt, welche spezifische biologisch inaktive oder aktive Oberflächen

besitzen. Diese beinhalten unter anderem Bio-Makromoleküle, poly-Elektrolyte, sowie Strukturen bakteriellen und viralen Ursprungs. Diese experimentelle Plattform ermöglichte es uns, sowohl quantitative als auch qualitative Aufnahme der MNP, phänotypische Zustandsänderungen der markierten Zellen, als auch daraus resultierende Bildgebungseigenschaften in Immunzellen zu studieren. Durch die Nutzung von bakteriellen MNPs, sogenannten Magnetosomen, war es uns möglich, Mechanismen und Wege der Internalisierung im Kontext von Toll-like Rezeptor (TLR) sowie Signalproteinen zu untersuchen. Darüber hinaus erörterten wir die Rolle des evolutionär konservierten Inflammasom-Signalweges, um immunologische Konsequenzen der verschiedenen MNP Rezepturen mittels Zellen des angeborenen Immunsystems zu erforschen.

Zusammenfassend liefert diese Studie Erkenntnisse über intrazelluläres Nanopartikel-Shuttling sowie Agglomeration, welche die MR Bildgebung signifikant beeinflussen. TLR und Signalprotein-Studien erbrachten Hinweise über alternative Aufnahmemechanismen sowie Art und Ausmaß der kompromitierten Immunantwort im Falle eines fehlenden Proteins.

Abstract

Engineered magnetic nanoparticles (MNPs) are currently emerging as promising tools in numerous applications for medical theragnostics including the development of drug delivery systems and contrast agents for magnetic resonance imaging (MRI). *In vitro* labeling of target cell populations with MNPs before therapeutic implantation shows great promise in monitoring successful cell engraftment, differentiation and migratory behavior using MRI. Depending on the desired therapeutic treatment outcome, these biological processes remain critical for the success of cell-based therapies.

Hematopoietic stem and their derived precursor cells are particularly suited for cell-based therapies due to their plasticity and ability to reconstitute the entire cell pool of the hematopoietic system in both steady-state and disease. Terminally differentiated immune cells such as macrophages and dendritic cells (DCs) represent optimal labeling agents due to their potential to initiate immune responses within the host. Macrophages are promising agents of the innate immunity and are crucial in identifying and clearing initial harmful threats through shaping subsequent immunological consequences. Professional antigen-presenting immune cells, such as DCs, play a key role in the induction of adaptive immune responses that result in the antigen-specific activation of B- and T-lymphocytes in secondary lymphoid organs. Taken together, this makes them a particularly attractive target for the development of cellular vaccines and contrast agents for MRI. Therefore, they are increasingly applied in clinical trials of today.

However, (i) the interaction of MNP formulations with a given target cell population, (ii) the induction of a desired immunological phenotype through targeted cell labeling strategies, and (iii) resulting MNP imaging properties using MRI remain largely unknown. Even though already in clinical practice, a systematic investigation of MNP uptake, phenotypic alteration of recipient cells and resulting MR imaging properties are still lacking and underlying mechanisms are poorly understood.

In this study, we engineered iron oxide based MNPs displaying distinct biologically inert or active surface coatings including bio-macromolecules, polyelectrolytes as well as shell structures of bacterial and viral origin. Given this experimental platform, we investigated quantitative and qualitative uptake of MNPs into target cells, phenotypic alterations of labeled cells and resulting imaging characteristics. Through employing bacterial magnetosome MNPs that possess pathogen-associated molecular patterns as an integral component on their surface

structures, mechanisms and routes of internalization were investigated in the context of toll-like receptors and signaling adaptor knockout mice. In addition, activation of the evolutionarily conserved inflammasome pathway was studied to investigate immunological consequences of MNP formulations in cells of the innate immune system.

Taken together, this study provides insights into MNP interactions with cells of the hematopoietic system. We provide evidence that shuttling and clustering characteristics inside target cells substantially shape MR imaging properties. Both uptake magnitude and MNP packaging properties within cells conferred MR contrast that was influenced by MNP surface chemistry. We believe these findings will aid in the future development of MNPs for cell labeling strategies designed for a pre-determined imaging purpose.

Table of Contents

Zusammenfassung ..... **I**
Abstract ..... **III**
Table of Contents ..... **V**

1 Introduction **1**
1.1 Molecular Imaging in Modern Medicine **1**
1.1.1 Bridging Biology, Chemistry, and Molecular Imaging 1
1.1.2 Labeling Agents in Molecular Imaging 2
1.2 Magnetic Resonance Imaging (MRI) **3**
1.2.1 Physical Principle of MRI 3
1.2.2 MRI Contrast Agents 4
1.2.3 Contrast Agent Development for Cell-Based Therapeutic Applications 6
1.3 Hematopoietic Stem Cells and their Progeny **6**
1.4 Immune Systems **8**
1.4.1 Innate Immunity 9
1.4.2 Adaptive Immunity 12
1.5 Dendritic Cell Biology **14**
1.6 Mechanisms of Endocytosis **16**
1.7 Pathogen Receptor Recognition Repertoire of Immune Cells **18**
1.8 Nano-Bio Interface(s) **20**
1.9 Aim of the Study **22**

2 Materials and Methods **24**
2.1 Materials **24**
2.1.1 Cell Culture Media and Supplements 24
2.1.1.1 Cell Culture Media 24
2.1.1.2 Growth Factors 24
2.1.2 Mice 25
2.2 Methods **25**
2.2.1 Cell Culture of Primary Cells 25
2.2.1.1 Isolation and Amplification of Murine Bone Marrow Cells 25
2.2.1.2 Culture of GM-CSF derived Progenitors and iDCs 25
2.2.1.3 Culture of Flt3L derived Progenitors and cDCs/pDCs 26
2.2.1.4 Cell Culture of Macrophages 27
2.2.1.5 Explantation and Culture of Primary Splenocytes 27
2.2.2 Nanoparticle Synthesis and Characterization 28
2.2.2.1 Synthesis of Poly-Electrolyte coated MNPs 28
2.2.2.1.1 MNP Core Synthesis 28
2.2.1.1.2 LbL Assembly of Poly-Electrolytes around Fe Cores 29
2.2.2.2 Oleate-Stabilized MNPs 30

2.2.2.2.1 Synthesis of Fe Core Particles ... 30
2.2.2.2.2 Oleate-Stabilized Ferrofluids ... 30
2.2.2.3 Bacterial Magnetosomes ... 30
2.2.2.4 Synthesis of Covalently linked "Stealth" MNPs ... 31
2.2.2.4.1 Synthesis of Iron Oxide Core MNPs ... 31
2.2.2.4.2 Synthesis of Anchor Moieties and Functional Groups ... 32
2.2.2.5 MNP Characterization ... 33
2.2.3 MNP Labeling with MNPs ... 33
2.2.4 MACS Cell Sorting ... 34
2.2.5 Cell Viability Assays after MNP Exposure ... 34
2.2.5.1 MTT Assay ... 34
2.2.5.2 Flow Cytometric Analysis (FACS) employing 7-AAD ... 35
2.2.6 Ferrozine Iron Assay ... 35
2.2.7 Prussian Blue Staining ... 35
2.2.8 Transmission Electron Microscopy (TEM) ... 36
2.2.9 Phenotypic Analysis using FACS ... 36
2.2.9.1 Table of Directly Labeled Antibodies for FACS Analysis ... 37
2.2.9.2 FACS Antibody Listing (Indirect: Primary + Secondary Antibodies) ... 37
2.2.10 *In Vitro* Migration Assays ... 37
2.2.11 Enzyme-linked Immunosorbent Assay (ELISA) ... 38
2.2.12 *Ex Vivo* Splenocyte Stimulation ... 39
2.2.13 Magnetic Resonance Imaging ... 39
2.2.13.1 Phantom Preparation and Immobilization of Cells ... 39
2.2.13.2 MRI Scan Parameters ... 39
2.2.13.3 MRI Data Analysis ... 40
2.2.14 Statistical Analysis ... 40
2.2.15 Software Employed ... 40

3 Results ... 41
3.1 Synthesis and Characterization of MNPs ... 41
3.2 Poly-Electrolyte and Lipid-Shell MNPs ... 44
3.2.1 Hematopoietic Progenitor Cells ... 44
3.2.1.1 Cytotoxicity Studies ... 45
3.2.1.2 Uptake and Intracellular Iron Concentration ... 46
3.2.1.3 Intracellular Iron Stainings ... 47
3.2.1.4 Phenotypic Surface Marker Composition of Labeled HSCs ... 48
3.2.1.5 *In Vitro* MRI Studies employing HSCs: Detection Limits ... 50
3.2.1.6 *In Vitro* MRI Studies employing HSCs: Relaxivity ... 51
3.2.2 Inflammatory Dendritic Cells (iDCs) ... 53
3.2.2.1 Biocompatibility Studies ... 54
3.2.2.2 Uptake and Intracellular Iron Concentration ... 55
3.2.2.3 Histological Staining of MNP-Labeled iDCs ... 56
3.2.2.4 Transmission Electron Microscopy (TEM) and Endosomal Packaging ... 57

3.2.2.5 Phenotypic Surface Marker Composition 58
3.2.2.6 *In Vitro* Migration Assay 60
3.2.2.7 *In Vitro* MRI Studies and Relaxivity 61
3.2.2.8 *In vitro* MRI Detection Limits and CNR Values 62
3.2.3 MNP stimulated Flt3L-Generated DC Subsets 64
3.2.3.1 MNP Stimulation of Flt3L Generated cDCs in the Context of Knockouts 64
3.2.3.2 MNP Stimulation of Flt3L Generated pDCs in the Context of Knockouts 66
3.2.3.3 ELISA Data of Bulk Supernatants after LbL-MNP Stimulation 68
3.2.4 Poly-Electrolyte MNP Stimulation of Macrophages 69
3.2.4.1 M-CSF derived Macrophages: FACS Profiling and Gating Strategy 69
3.2.4.2 Macrophages: Phenotype in the Context of TLR4 Knockouts 70
3.2.4.3 ELISA Cytokine Secretion in the Context of TLR4 Knockouts 71
3.2.5 Mixed Splenocyte Responses after Poly-Electrolyte MNP Stimulation 72
3.2.5.1 T-Cell Proliferation Capacity after LbL-MNP Stimulation 73
3.3 Immunological Properties of Bacterial Magnetosomes 74
3.3.1 Hematopoietic Progenitor Cells 75
3.3.1.1 Biocompatibility Studies of Bacterial Magnetosomes using HSCs 75
3.3.1.2 MSR-1 Uptake Studies employing HSCs 76
3.3.1.3 Phenotypic Profiling of MSR-1 pulsed HSCs 77
3.3.1.4 Molecular Imaging Properties Employing MSR-1 77
3.3.2 Inflammatory Dendritic Cells (iDCs) 78
3.3.2.1 Uptake Properties of Bacterial Magnetosomes into Inflammatory DCs 78
3.3.2.2 Phenotypic iDC Cytometry Profiling of Bacterial Magnetosomes 80
3.3.2.3 *In Vitro* Migration Assay using iDCs and MSR-1 Stimulation 81
3.3.3 MSR-1 stimulated Flt3L-Generated DC Subsets 83
3.3.3.1 FACS Profiling of MSR-1 Pulsed cDC Populations 83
3.3.3.2 FACS Profiling of MSR-1 Pulsed pDC Populations 84
3.3.3.3 Cytokine Release of Bulk Flt3L derived DC after Magnetosome Exposure 84
3.3.4 Bacterial Magnetosomes in the Context of Macrophages 86
3.3.4.1 Phenotypic Analysis Employing Cytometry 86
3.3.4.2 Macrophage ELISA Data 86
3.3.5 Mixed Splenocytes in the Context of MSR-1 87
3.3.6 Macrophages in the Context of Innate Immunity 88
3.3.6.1 Magnetosomes and the Inflammasome Pathway 88
3.3.6.2 IL-1ß Sequestration and ASC Adaptor Protein Dependency 89
3.4 Concept of "Stealth" Particles and their Properties 90
3.4.1 Inflammatory Dendritic Cells (iDCs) in the Context of "Stealth" MNPs 91
3.4.1.1 Iron Oxide Uptake Properties and Quantification 91
3.4.1.2 Phenotypic Cytometry Analysis using iDCs 92
3.4.2 "Stealth" MNP in the Context of Flt3L-Generated DCs 93
3.4.2.1 Phenotypic Surface Marker Analysis of Flt3L-Generated cDCs 93
3.4.2.2 "Stealth" Particles in the Context of Flt3L Derived pDCs 94
3.4.2.3 Cytokine Release of Bulk DCs in the Context of "Stealth" Particles 95

3.4.3 "Stealth" MNP Pulsed Macrophages 96
3.4.3.1 FACS Profiling of "Stealth" MNP Pulsed Macrophages 96
3.4.3.2 ELISA Cytokine Secretion of M-CSF Generated Murine Macrophages 97
3.4.4 Splenocyte Responses to "Stealth" MNPs 98
3.5 Influence of Serum Components on MNP-iDC Interactions 99
3.5.1 Serum-Dependent Uptake Kinetics of MNPs 99
3.5.2 Serum-Dependency of Intracellular Iron Concentration 101
3.5.3 Impact of Protein "Corona" on MR Imaging Properties 101
3.6 Concept of Functionalized Acryl-MNPs 103
3.6.1 FACS Data of pDCs and Bulk Supernatant ELISA 103
3.6.2 ELISA Cytokine Secretion of Flt3L-Generated Bulk DCs 105

4 Discussion 107
4.1 Chemical Stability and Biocompatibility of MNP Formulations 108
4.2 Uptake Properties and Intracellular Iron Deposition 110
4.3 MRI Contrast Agent Potential 113
4.4 Immunological Consequences after Contrast Agent Exposure 114
4.5 Concluding Remarks 117

5 References 119

6 Appendix 134
6.1 Abbreviations 134
6.2 List of Tables and Figures 138
6.3 Scientific Publications and Presentations 141

Acknowledgements 143
Eidesstaatliche Erklärung 146

1 Introduction

1.1 Molecular Imaging in Modern Medicine

Molecular imaging emerged in the early twenty-first century as a discipline at the intersection of molecular biology and *in vivo* imaging. Although it lacks a universal definition, molecular imaging is often considered the non-invasive, quantitative, and repetitive imaging of targeted macromolecules and biological processes in living organisms[1]. Today, the most common molecular imaging techniques used in both research settings as well as clinical practice are positron emission tomography (PET), optical imaging, computed tomography (CT), ultrasound and magnetic resonance imaging (MRI)[2,3].

The multiple and numerous potentialities of these imaging modalities are applicable to the diagnosis of diseases (e.g. cancer) through altered molecular profiles and/or cell behavior prior to visual anatomic alterations[4]. Therefore, the employment of molecular imaging could potentially allow for (i) early detection of disease, (ii) more accurate prognoses and personalized treatments, (iii) the ability to monitor the effectiveness of therapeutic treatment regimes, and (iv) improvements in our understanding of how cells behave and interact within their micro-environment in living subjects[5].

Furthermore, PET and MRI have recently gained much interest in the field of medical research due to the fact that they allow the study of molecular mechanisms non-invasively[4]. This permits researchers to gain valuable knowledge of functional processes in health and their alterations in disease states that in turn lead to the development of more sophisticated imaging agents.

1.1.1 Bridging Biology, Chemistry and Molecular Imaging

Cells, either being normal or aberrant, cannot easily be distinguished from each other by *in vivo* imaging. In order to enhance imaging contrast of biological target structures from surrounding tissues, chemically synthesized contrast agents are being employed[6]. These molecular imaging vectors aid the visualization of biological processes and range from fluorescent probes (optical imaging) to α-radiation emitters (PET, single-photon emission computed tomography (SPECT)) up to nano-scale contrast agents (MRI)[3,7]. In therapeutic

and diagnostic applications of today, these vectors are obligated to fulfill distinct criteria to permit imaging of specific molecules *in vivo*, in particular: (i) the availability of high affinity probes with reasonable pharmacodynamics, (ii) the ability of these probes to overcome biologic delivery barriers (vascular, interstitial, cell membrane), (iii) the use of amplification strategies (chemical or biological), and (iv) the availability of sensitive, fast, high resolution imaging techniques[8].

1.1.2 Labeling Agents in Molecular Imaging

Potential labeling agents for applicable molecular imaging modalities possess functionalities related to their respective imaging goal and imaging modality at hand. In brief, three categories of labeling agents are being employed today: genetic reporters, injectable contrast agents and exogenous cell trackers[2]. These vectors allow targeting of a specific tissue, cell or even molecule, and thus, facilitate direct interaction and/or binding with ligand moieties that ultimately enhances molecular imaging characteristics.

Although still limited to experimental mouse models, genetic reporters are cloned into the promoter or enhancer region of a gene of interest to be expressed concomitantly[9]. The type of imaging protein expressed is related to both (i) the research question at hand and (ii) the imaging modality to be employed, e.g. fluorescent markers in optical imaging[10].

Injectable contrast agents on the other hand are more widely used even in clinical settings[7]. However, due to stringent design criteria to minimize background signals and yield high local concentrations at the intended sites, a lot of research is devoted to understanding the molecular mechanisms involved in vector accumulation and clearance[10,11,12]. This process will aid in the future optimization of systemically administered contrast agents to maximize their target-to-background ratios, and thus, improve their imaging potential[2].

Exogenous cell trackers are being increasingly employed using adoptive cell transfer therapies, including immunotherapeutic strategies[13]. In order to monitor therapeutic progression, exogenous cell trackers allow a specific *ex vivo* targeting of distinct cell populations prior to re-administration. To non-invasively track fate and localization of implanted target cells *in vivo* after vector targeting, molecular imaging modalities such as MRI have been the method of choice[14,15,16].

1.2 Magnetic Resonance Imaging (MRI)

MRI has been widely used in both diagnostics and treatment regimes. Due to its capability to non-invasively monitor target tissues within their detailed anatomical context, MRI has advanced to an indispensable imaging tool in molecular medicine[17,18].

1.2.1 Physical Principle of MRI

Magnetic resonance tomography is based on the absorption and emission of energy in the radio frequency range of the electromagnetic spectrum and was first characterized in 1946[19]. Produced images derive from spatial variations in the phase and frequency of the radio energy being absorbed and emitted by the imaged object[20]. Biological systems such as rodents and humans mostly consist of water molecules composed of hydrogen and oxygen atoms. Nuclei of hydrogen protons possess a quantum mechanical property - the nuclear spin angular momentum (I) - that can be quantified using the Plank constant h as follows:

$$|I| = \frac{h}{2\pi}\sqrt{I(I+1)}$$

Hydrogen possesses a nuclear spin quantum number of ½. Placed in an external magnetic field (B_0), the hydrogen spin will precess about B_0 with the Larmor frequency (ω) in a discrete direction. The spin of ½ enables two possible alignments corresponding to the energy level of the nucleus. The distribution of the spins between the two possible energy states follows a Boltzmann distribution, which is dependent on the temperature T and the energy difference ΔE between the allowed states. The Boltzmann constant is represented by *k*.

$$\frac{N_{-1/2}}{N_{+1/2}} = exp\left(-\frac{\Delta E}{kT}\right)$$

For hydrogen, the two energy states are $N_{+1/2}$ spin 'up' (low energy) and $N_{-1/2}$ spin 'down' state (high energy). The Boltzmann distribution shows that at 37°C (average body temperature) slightly more spins occupy the lower energy state, thus generating the net magnetization vector M. These excess spins are used to generate the MR signal. The energy difference between the high and low energy states is proportional to the strength of the externally applied magnetic field B_0. Thus, the greater the strength of the external field, the greater the energy difference between the two spin states.

A second radiofrequency pulse, which is perpendicular to B_0, can now be applied to generate field B_1 (**Figure 1.1**). This field causes spins to flip off the z-axis and turn the net magnetization towards the transverse plane (x and y axis). The precessing about the z-axis in a xy-plane generates a detectable field. After switching off the previously applied pulse, the

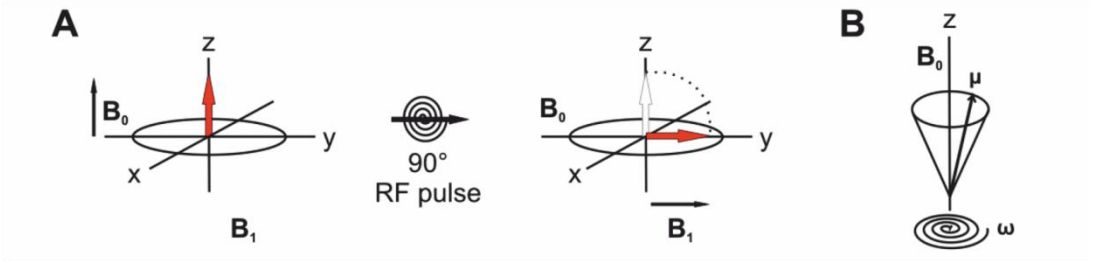

Figure 1.1 Physical principle of MRI relaxation. Radiofrequency pulses (RF) employed to alter initial magnetic vector B_0. Once turned off, the physical proton micro-environment determines both T1 and T2 relaxation patterns used in MR image aqcuisition. **A)** 90° flipping of magnetic field vector B_0 into resulting B_1 after introduction of the radio frequency pulse results in complete abrogation of magnetic vector along z-direction. Equilibrium state re-acquired after pulse is turned off again. The time interval needed until initial state B_0 is reached is termed spin-spin relaxation (T2). **B)** Precession (ω) of individual spins around the z-axis. Spin-lattice relaxation (T1) represents the time required for all individual spins to return to equilibrium state B_0.

generated B_1 ceases to exist and the nuclear spins return to their ground state. This process is called relaxation. The time required to return to the ground state is termed relaxation time. Relaxation time data of measured samples are used to produce the MR image.

Relaxation can be subdivided into two physical phenomena occurring simultaneously: The recovery toward equilibrium alignment and the transverse decay[20]. The return of the M alignment around the z-axis to equilibrium by a time constant is termed the spin-lattice relaxation T1. Duration of the return from transverse decay is described as spin-spin relaxation T2. T1 and T2 are properties of the water milieu due to the presence of physicochemical microenvironments, the biological composition such as water mobility, the presence of microstructures, macromolecules and membranes[21,22]. These parameters provide MRI its power to distinguish between different tissues.

1.2.2 MRI Contrast Agents

Since hydrogen protons are naturally present in biological specimens, MR imaging can be performed without employing contrast agents. However, these agents are often being used to enhance imaging of target structures within their anatomical background to improve disease diagnosis and therapeutic monitoring[23]. MRI contrast agents are a class of pharmaceuticals

that enhance the image contrast between tissues in which the agent accumulates and their anatomical surroundings. This provides superior differentiation of normal from aberrant tissues and delivers information about the status of e.g. organ function or blood flow[22].

Generally speaking, contrast agents can be divided into two categories, namely paramagnetic and superparamagnetic compounds[6]. Most commonly, Gadolinium (III) (Gd) chelates are employed as paramagnetic contrast agents that predominantly reduce T1 relaxation times (spin-lattice relaxation). They are referred to as positive MRI contrast agents because they enhance signal intensity compared to their unlabeled surroundings. Gd represents a lanthanoid that belongs to the group of rare earth metals that is frequently employed in molecular imaging regimes. However, as free solubilized aqueous ion, Gd possesses high cellular toxicity, potentially leading to e.g. anaphylactic shock, renal dysfunction and possibly, lethality. In order to harness its potential as MRI contrast agent, it is frequently chelated to e.g. di-ethylene-tri-amine-pent-acetate (DTPA) or similar compounds. The resulting stable contrast agents such as Magnevist® (DTPA stabilized) are frequently used in MRI scans to enhance imaging of e.g. vasculature[24].

Superparamagnetic contrast agents on the basis of iron oxide are comprised of metallic core structures and surrounding layer(s) of coating to confer particle biocompatibility, monodispersity and stability[25]. Cores are typically composed of magnetite (Fe_3O_4) and/or maghemite (γFe_2O_3), with maghemite resembling the oxidized form of magnetite. Iron oxide based contrast agents are further sub-divided according to their overall size, namely: oral-SPIO (small particles iron oxide) (300nm - 3.5µm), SPIO (60 - 150nm), ultra-small SPIO (USPIO) (10 - 40nm), and monocrystalline iron oxide nanoparticles (MION) (10 - 30nm). In general, SPIO exceeding a hydrodynamic size of 50nm are comprised of multiple iron oxide crystals. Their mode of action underlies their ability to elicit substantial disturbances in the local magnetic field. This is achieved through large magnetic moments that lead to a rapid dephasing of adjacent protons, thus generating a detectable change in MR signal. Iron oxide MNPs represent ferromagnetic materials that reduce T1, T2 and T2* relaxation times. However, in contrast to T1 contrast agents, they lead to an enhanced decrease of the MR signal, and thus, are being referred to as negative contrast agents[26].

1.2.3 Contrast Agent Development for Cell-Based Therapeutic Applications

Even though MRI represents a powerful imaging tool, its molecular detection limit is not superior when compared to other imaging modalities such as PET or optical techniques. To overcome its inherent lack of sensitivity, constant optimization of contrast agents is crucial for the improvement of disease diagnosis and treatment regimes in the future. A lot of interdisciplinary research is being devoted to develop contrast agents that are able to target specific cell types via distinct uptake routes as well as enhancing physico-chemical imaging characteristics, thereby optimizing imaging potential[27,28].

In a given clinical or research setting, both size as well as the surface decoration of contrast agents add up to yield (i) systemic half-lives and clearance, (ii) preferred sites of vector accumulation, and (iii) specific cell/tissue targeting. Shell structures of contrast agents are designed to facilitate targeted uptake or evade clearance mechanisms, thus extending their circulation time or being accumulated at sites of interest. This in turn leads to a significant improvement of MR imaging contrast.

In diseases of the modern age, such as cancer, cardiovascular, autoimmune diseases and allergies, cells of the immune system and their precursors have been utilized as biological targets for intervention/therapeutic strategies in combination with exogenous cell trackers[13,29,30,31]. This includes $CD34^+$ stem cells, their immediate progenitors and terminally differentiated immune cells. Due to their plasticity and inherent biological functions, they represent a promising tool for research as well as diagnostic and therapeutic applications[32,33]. Recent development in the field of nanotechnology allows the labeling and monitoring of these therapeutically administered cellular vectors in combination with molecular imaging modalities such as MRI. It has been widely established that these techniques in combination with administered contrast agents are crucial for the success to such cell-based therapies[14,34].

1.3 Hematopoietic Stem Cells and their Progeny

Stem cells can be defined as cells that retain both self-renewing capabilities as well as the potential to give rise to clonal progeny with the ability to differentiate[35,36]. All adult blood cells, including red blood cells, platelets, and terminally differentiated immune cells, derive from hematopoietic stem cells (HSCs). These multipotent HSCs reside in specialized microenvironments termed “niches” that nourish and sustain their existence within the bone

marrow[37]. By undergoing both symmetric and asymmetric cell division events, HSCs either maintain a constant pool of identical progeny on the one hand, while developing into downstream progenitors and eventually into terminally differentiated "effector" cell types on the other[38]. Effector cells arise as a result of successive restriction and commitment events that are tightly regulated by both the action of transcription factors and the local cellular micro-environment provided by the stem cell niche[39,40].

Successive differentiation events can be envisioned as a branching family tree that diverges with progressing levels of cellular commitment steps (**Figure 1.2**). Within this hierarchy,

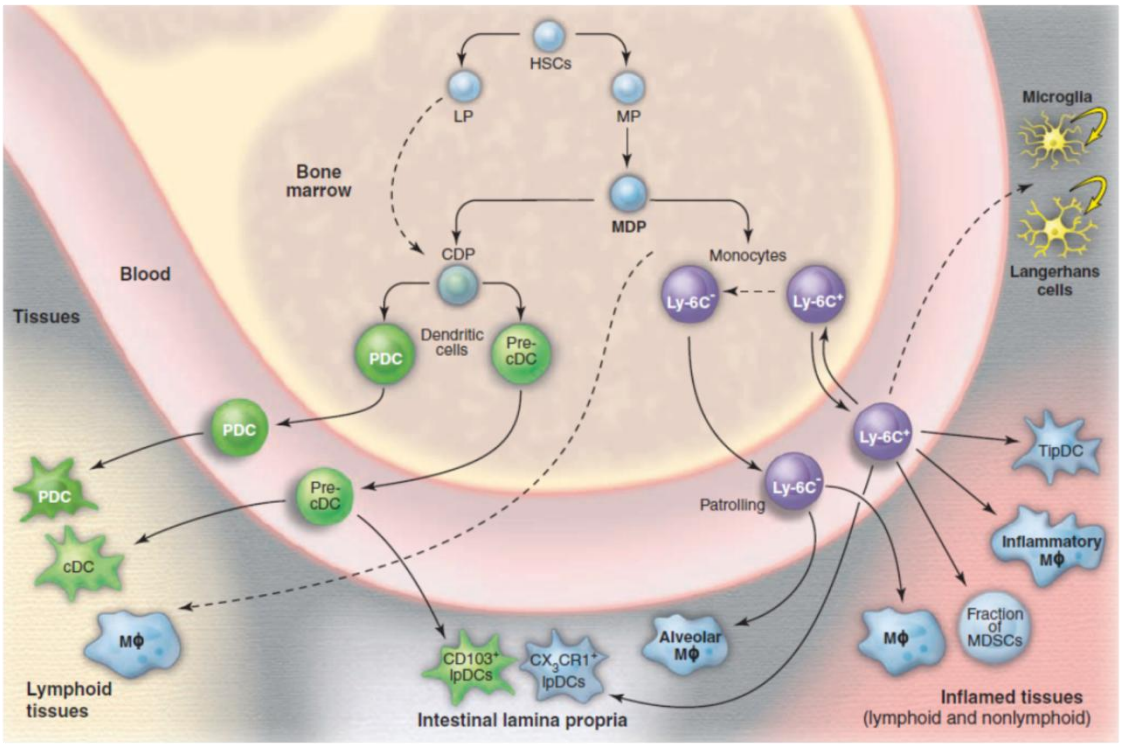

Figure 1.2 Developmental pathways originating from HSCs. Bone marrow derived stem cells undergo a series of both myeloid and lymphoid commitment steps before circulating within the blood stream. Upon encountering chemotactic signals, they further differentiate into distinct DC subsets and tissue-resident macrophages after extravasating into organs and tissues. Reproduced from Geissmann et al., 2010[41].

HSCs represent the upper-most entity that is capable of giving rise to immediate precursor cells of the myeloid (MP) and lymphoid (LP) lineage of blood cells[41]. In turn, these partially committed precursors further differentiate into MDPs (monocyte, macrophage and dendritic cell (DC) precursors) and CDPs (common DC precursors), potentially capable of giving rise to the different subsets of monocytes, macrophages, and DCs. After the initial differentiation steps, terminally differentiated immature immune cells as well as late stage precursor cells leave the bone marrow to home into their final destination. As illustrated in Figure 1.2, crosstalk between the two separated branches of commitment ultimately leads to the

generation of the entire cellular blood pool, allowing the immune system to replenish cells in steady-state and react to arising inflammatory conditions[42].

1.4 Immune System

Throughout evolution, biological systems had to develop a sophisticated means of coping with the constant threat of invading pathogens such as e.g. bacteria and viruses. Depending on the nature, number, and entry point of the invaders, immune systems need to be capable of initiating an appropriate enzymatic, cellular, and/or humoral counter-measure to fight and eliminate any potential exogenous environmental hazards or endogenous cellular abberations[43,44]. To accomplish this difficult task, most biological systems have developed two distinct divisions within their immune system, the so-called innate and adaptive immunity[45,46,47].

Innate immune systems provide immediate defense mechanisms against numerous infectious agents and are present in all living organisms[48]. In jawed vertebrates, evolution has led to the formation of the so-called acquired or adaptive immunity based on specialized cell pools that allow antigen-specific recognition and long-term protective immunity against encountered antigens[49].

As illustrated in **Figure 1.3**, both immune branches consist of distinct cell types responsible for the recognition, engagement and subsequent clearing of pathogens. Non-cellular protein components such as the complement system or immunoglobulins exist in both arms of immunity and have evolved to aid in cellular counteractive measures that restore health.

Innate and adaptive immune countermeasures co-exist and mechanisms are interconnected to ensure proper functionality, even though the molecular diversity of pathogens is confronted in fundamentally different ways[43].

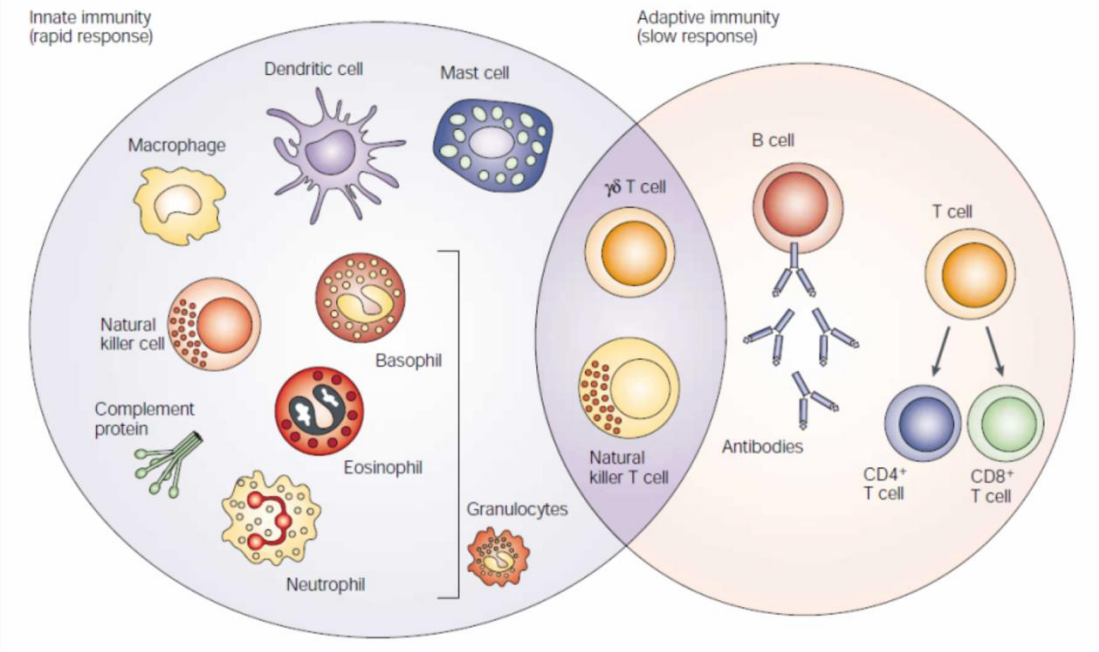

Figure 1.3 Graphical depiction of terminally differentiated immune cells of both innate and adaptive immunity. Cellular components of innate immunity comprised of phagocytic cells derived from bone marrow resident HSCs and their immediate downstream precursors. Adaptive countermeasures include T- and B-lymphocytes and their respective effector phenotypes. Adopted from Dranoff et al., 2004[44].

1.4.1 Innate Immunity

Agents of the innate immunity are represented by physical barriers such as the skin and mucosal surfaces lining potential entry points as found in the respiratory and gastrointestinal tract. Desquamation of the skin, antimicrobial enzymes present in saliva and tears, and the acidic pH milieu of the stomach represent the non-cellular components of the innate immune system[49]. Another hallmark of the innate immune defenses is the complement system, which represents yet another versatile defense machinery of non-cellular countermeasures[50]. It provides the capability to (i) opsonize antigens and (ii) release soluble chemotactic molecules attracting various cell types of both innate and adaptive immunity and (iii) lyse invading cells through actions of the "membrane attack complex"[51]. Dedicated scavenger cells clear sights of primary invasions as well as eliminating cell debris and dying cells, thereby also contributing to physiological homeostasis[41,52].

Recognition of pathogens is achieved through germline encoded pattern recognition receptors (PRRs) present on all cell types of the innate immune system. Throughout evolution, these trans-membrane signaling receptors have co-evolved with pathogen-associated molecular patterns (PAMPs) present on e.g. bacteria to recognize a broad spectrum of evolutionary

conserved and invariant antigens[46]. However, in contrast to the antigen receptor repertoire of the adaptive immune system, innate PRRs are only capable of limited antigen recognition.

Innate defense mechanisms are always turned on, and, unlike acquired immunity, do not need a series of events and time leading to their full capacity[53]. Therefore, it is being referred to as rapid response system that is capable of engaging potentially harmful invading pathogens without a lag or adaptation phase based on the actions of both cellular factors as well as protein complexes such as e.g. the complement cascade[54].

The immune cells of the innate defense are mainly comprised of professional phagocytes, among them monocytes, macrophages, and DCs (Fig. 1.3)[55]. Neutrophils, a specialized short-lived population of granulocytes, also exert a very high phagocytic potential[56]. In combination with basophils and eosinophils, they aid in both the (i) destruction of invading pathogens and (ii) immune cell recruitment to sites of inflammation through the action of e.g. histamine and prostaglandins[57]. Furthermore, both granulocytes and natural killer (NK) cells are potent direct killers of certain pathogens once opsonized by antibodies, complement proteins or after PAMP recognition[58,59]. In addition, NK cells are crucially involved in defense strategies against viral infections[60]. Through a continuous sensing of "self" protein motifs on somatic cell membranes in the context of Major Histocompatibility Complex class I (MHC I) molecules, NK cells are capable of detecting and destroying invaded cells by recognizing a concept termed "missing or altered self"[61]. Mast cells represent tissue-resident cells involved in inflammation and recruitment of additional immune cells to sites of antigenic contact. They highly express FcεRI receptors capable of irreversibly binding Fc regions of IgE antibodies produced by plasma cells. Upon antigen contact and antibody cross-linking they release the content of their intracellular granula into the interstitium[62].

As depicted in **Figure 1.4**, monocytes give rise to a variety of tissue-resident cell types of the immune system[63]. They are known to originate directly from the bone marrow as a consequence of asymmetric HSC divisions that give rise to a $Ly6C^+$ common myeloid progenitor which is released into the peripheral blood[64]. After circulating for up to several days they enter the tissues in order to replenish e.g. tissue macrophage and DC populations in steady-state. Danger signals elicit increased recruitment of monocytes to sites of inflammation in a CCR2/CCR7 dependent manner prior to differentiation into macrophages and DCs that contribute to host defense, tissue remodeling and subsequent repair[65].

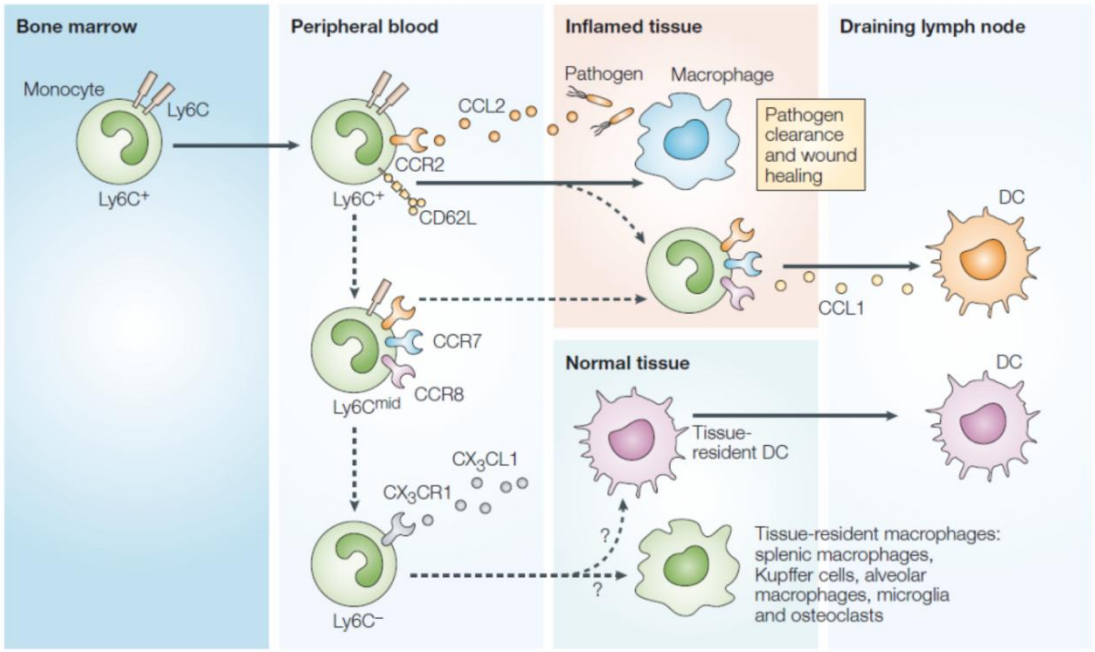

Figure 1.4 Origin and differentiation capacity of bone marrow derived monocytes. DCs and tissue-resident macrophages of the reticulo-endothelial system (RES) survey their immediate environment for potential hazards such as exogenous (PAMPs) and endogenous danger signals (DAMPs). Upon stimulation of resting monocytes, appropriate immunological consequences are triggered. Modified from Gordon and Taylor, 2005[63].

Upon encountering various chemotactic signals that strongly depend on the composition of inflammatory mediators secreted within the local micro-environment, blood-borne monocytes differentiate into macrophages and extravasate into sites of potential danger. In steady-state, they populate virtually all tissues, where they reside and sense potentially harmful antigens within their immediate environment[63]. These tissue-specific macrophages constitute the reticuloendothelial system (RES), which is responsible for the physiological clearance of particles, apoptotic cells and pathogens. Macrophages display remarkable plasticity allowing them to efficiently respond to environmental signals[66]. In order to do this, they are equipped with PRR surface receptors that recognize evolutionary conserved protein motives on pathogens including toll-like receptors (TLRs) and interleukin-1 receptor[67]. The most important phenotypes of macrophages resemble M1 and M2 activation states[68,69]. M1 macrophages are being activated via IFNγ and TLR stimulation, resulting in elevated expression of MHC II, IL-12, and TNFα. These in turn lead to the generation of reactive oxygen species (ROS) and nitric oxide (NO) that are involved in the destruction of pathogens or aberrant cells[70]. On the contrary, the presence of IL-4 and IL-13 results in the differentiation of macrophages into M2 that is involved in Th2 immune responses including humoral immunity and wound healing[71].

Dendritic cells on the other hand represent the bridge between innate and adaptive immunity because they serve as sentinels in peripheral tissues as well as being professional antigen-presenting cells that stimulate naïve T- and B cells in secondary lymphoid organs[72]. They possess a high phagocytic and macropinocytic activity when in an immature phenotype in peripheral tissues[73]. DCs are also critically involved in both central as well as peripheral tolerance by presenting "self-antigens" to naïve T- and B cells in a mature, but non-activated state[72,74].

1.4.2 Adaptive Immunity

Although the innate immune system is able to clear most emerging infections before the onset of colonization, not all threats are recognized. This is due to the fact that pathogens co-evolved and developed new ways of overcoming immunological barriers imposed on them throughout evolution[49]. To recognize unknown pathogen motifs, evolution has led to the formation of antigen receptors capable of sensing novel antigenic encounters. This is achieved through somatic recombination events on the genomic level. Variable (V), diversity (D), and joining (J) gene fragments encoding for these T- and B cell receptors are segmented and randomly assembled together with a fixed constant domain during cellular maturation events. This process, termed VDJ recombination, leads to a diverse repertoire of receptors with random but narrow specificities and is considered the hallmark of adaptive immunity[75].

The two major effector cell types comprising the adaptive immune system are B- and T-lymphocytes. Both cell types are responsible for translating the peptide information acquired through professional antigen-presenting cells (APCs) into an effector immune response.

B cells on the one hand produce a distinct type of immunoglobulin upon stimulation that solely depends upon the nature of the stimulus[76]. They mature in the bone marrow to ensure that "self"-reactive cells are not propagated in order to exclude potential auto-immune reactions. T cells mature to aid in adaptive immune responses through differentiating into several effector T-phenotypes (Th1, Th2, Th17, Treg)[77,78]. From the bone marrow, T cell precursors migrate into the thymus where they are either propagated or deleted from the functioning T cell pool to avoid "self" reactivity. This step is particularly important to ensure tolerance to "self" both in central as well as peripheral immunity[79,80]. After their selection process, both cell types migrate to secondary lymphoid organs where they reside as naïve cells within B- and T cell areas, respectively[81]. Upon contact with an activated APC

displaying a matching antigen for their specific B- or T cell receptor, cellular maturation is induced that results in the initiation of an appropriate adaptive immune response.

It is important to note that B- and T cells recognize different forms of antigens. B cells on the one hand possess a membrane-bound immunoglobulin that is potentially targeted by foreign antigens, and thus, elicits activation of the respective B cell clone. The bound antibody on the surface of the B cell mimics a trans-membrane receptor and therefore is called B cell receptor (BCR)[82]. Once activated and matured into a plasma cell, the B cell is capable of releasing vast amount of soluble antibodies that possess the same specificity and binding affinity towards the initial activating antigen. In contrast to the T cell receptor (TCR), however, BCRs are able to bind soluble antigenic moieties presented to them via the lymph. Antigens presented to T cells through this route are not capable of eliciting cellular maturation and effector function unless accompanied by additional stimuli originating from professional APCs[83]. Furthermore, antigenic peptides loaded onto MHC molecules prior to extracellular presentation are cleaved within late endosomal structures of APCs. T cell maturation is only induced in the context of these structures in addition to discrete co-stimulatory molecules such as CD80 and CD86 that are sequestered or presented through APCs[84].

Unlike the innate immune response, information gathered in form of recognizable antigens has to be presented to effector cells in secondary lymphoid organs. Professional antigen-presenting cells, which are responsible for the identification, storage and delivery of these antigens, pass on the acquired information via processed protein residues on MHC class I and II molecules acquired in peripheral organs[85]. Subsequently, (depending on the nature of the signal) a specific type of adaptive immune response is initiated in secondary lymphoid organs.

Yet another hallmark of the adaptive immune system is the immunological memory. Infections that have been successfully cleared once lead to the formation of memory cells that store the antigenic information over a long period of time. If a given biological system is challenged with the same antigen again, re-activation of these dormant differentiated B cells, termed memory cells, lead to a rapid and enhanced immune response[86].

1.5 Dendritic Cell Biology

DCs represent professional antigen-presenting cells and are considered one of the most important immune cell types due to their pivotal role in determining the balance between immunity and tolerance induction[87,88]. Through their phagocytic and pinocytic activity, they are capable of ingesting vast amounts of extracellular material, including both self-antigens as well as foreign, potentially harmful, particles[73,89]. The capability for phagocytosis, macropinocytosis, and the expression of receptors mediating adsorptive endocytosis (e.g. C-type lectin receptors and Fcγ and Fcε receptors) render DCs particularly effective in antigen uptake[72,90,91]. This also includes their expression of numerous receptors recognizing evolutionary conserved protein motifs on bacteria and viruses, such as TLRs[92,93].

DCs represent the most potent T cell activator, which provides them with the capability of initiating an appropriate adaptive immune response after antigenic contact. This is achieved through processing of antigens and presenting the acquired biological information to naïve T-lymphocytes in the context of MHC molecules. Through the fusion process of phagosomes originating from endocytosed material with early lysosomes emerging from the endoplasmatic reticulum (ER), the invariant peptide chains of MHC II molecules are replaced with the appropriate foreign peptide chain (length 15-25 amino acids)[94]. Intracellular antigens originating from self-proteins or viral origin are processed in the cytosol and bind to MHC class I molecules directly for presentation on the cell surface[95]. The target for MHC I peptide presentation are $CD8^+$ cytotoxic T cells, whereas MHC II loaded peptides confer activation of $CD4^+$ helper T cells. The local cytokine milieu and co-stimulatory molecule expression on APCs polarizes naïve T cells toward an effector function (T helper (Th) 1, Th2, Th17 or regulatory T cells (Treg)) depending on the type and magnitude of the stimulus[96].

DCs that capture self-antigens in steady state are not being activated. Instead, presentation of acquired self-antigens leads to the maintenance of peripheral tolerance by silencing T cells potentially reacting against those antigens[97,98].

DCs are present primarily at sites of pathogen entry points such as skin, lung, and the gastrointestinal tract as well as in the circulatory system and internal organs, in particular lymphoid tissues[72,91,99].

Due to the fact that DCs are considered one of the most important cell type of the immune system, a lot of research has been devoted to understanding their biological function and origin[89]. It has been shown by several independent studies that DCs can be divided into

several subsets according to their localization, phenotype and function[100]. Both myeloid and lymphoid derived DCs originate from a common precursor within the bone marrow compartment expressing the receptor for fms-like tyrosine kinase 3 (Flt3)[101,102]. Asymmetric cell division events of $Flt3^-$ HSCs result in $Flt3^+$ progenitors capable of giving rise to both myeloid and lymphoid committed common progenitors that retain the potential to further differentiate into the various types of DCs (as previously depicted in Figure 1.1).

The main DC subsets are non-lymphoid tissue migratory DC that are spread throughout peripheral organs, the conventional DCs (cDC) and plasmacytoid DCs (pDC) found in lymphoid tissue such as spleen and lymph nodes[99,103].

Interstitial DCs (DCs of e.g. dermis, mucosa and lung) and epidermal Langerhans cells (LCs) are both regarded as tissue DCs and represent the classical antigen presenting cells. In order for them to present antigens taken up and processed in the periphery, they constantly migrate from peripheral tissues via the lymphatics to draining lymph nodes[104,105,106]. Tissue DCs possess morphological characteristics such as membrane protrusions (dendrites) to constantly survey their immediate surroundings. After cellular activation due to antigen uptake, they acquire a migratory phenotype and present this immunological information to naïve T cells in lymphoid organs. Therefore, they are considered the true migratory DCs[89].

Due to different developmental origins and phenotypic characteristics, various subsets of tissue DCs have recently been studied in great detail. Especially skin DCs are well characterized and can be divided into epidermal LCs, $CD103^+Langerin^+CD11b^{low}$ and $CD11c^+CD11b^+$ DCs of the dermis[107,108,109]. Similarly, DCs in other non-lymphoid tissues are classified into $CD103^+$ and $CD11b^+$ DCs[110,111].

Conventional DCs on the other hand reside within lymphoid organs and constantly monitor lymph-borne antigens. cDCs are also capable of initiating an adaptive immune response via the stimulation of lymphoid tissue resident naïve T cells. According to novel classifications, they can be subdivided into $CD8\alpha^+$ and $CD8\alpha^-$ DCs[112,113]. The different cDC subsets have specialized functions, namely the ability to cross-present soluble and cell-associated antigens on MHC class I molecules to $CD8^+$ T cells ($CD8\alpha^+$ DCs)[114,115] as well as presenting antigens on MHC class II to $CD4^+$ T cells ($CD8\alpha^-$ DCs)[116,117]. For this reason, $CD8\alpha^+$ and $CD8\alpha^-$ cDCs display a distinct cytokine production repertoire to differentially regulate immune responses[118].

pDCs are found in blood and in many organs such as the thymus, bone marrow and within T cell areas of lymphoid organs and possess a plasma cell-like phenotype in steady state[119,120]. They are involved in the recognition of viral infections and are known to produce vast amounts of type I interferons (IFN) upon stimulation. Activated pDCs are capable of priming T cells against viral antigens, although they are poor T cell activators compared to tissue DCs and cDCs[121,122].

Inflammatory DC (iDC) represent a specific DC subset that develop from circulating $CD11b^{+}Ly6C^{+}CCR2^{+}$ monocytic precursors only under inflammatory conditions and that have no steady state counterpart. Amongst them are the so-called "tip-DCs" due to their potential to produce tumor necrosis factor α (TNFα), inducible nitric oxide synthase (iNOS) and oxygen radicals after microbial infection[123]. However, the exact function of inflammatory DC is still being elucidated, although they have been shown to be involved in antigen presentation to T cells or direct killing of pathogens[41,124].

1.6 Mechanisms of Endocytosis

Endocytosis encompasses several diverse mechanisms by which cells internalize macromolecules and particles into transport vesicles derived from the plasma membrane through processes of engulfment, invagination and pinching. It controls entry into the cell and has a crucial role in development, immune responses, neurotransmission, intercellular communication, signal transduction, as well as cellular and systemic homeostasis[125]. Lipids, integral proteins and extracellular materials are transported to various intracellular compartments for further processing and recycling within the endosomal compartment[126].

Several forms of uptake are known that strongly depend upon particle size and antigenic surface makeup of the respective target cell and can be subdivided into two broad categories, phagocytosis and pinocytosis. Phagocytosis encompasses the uptake of larger structures and is usually confined to specialized cell types, whereas pinocytosis occurs in virtually all cells[127]. Pinocytosis includes four distinct mechanisms that depend on the size and structure of the ingested material: macropinocytosis (> 1μm), clathrin-mediated endocytosis (~ 120nm), caveolae-mediated endocytosis (~ 60nm), and clathrin- and caveolin-independent endocytosis (~ 90nm) (**Figure 1.5**)[125].

The constitutively activated clathrin-mediated endocytosis (CME) permits the continuous uptake of nutrients by cells and the intercellular communication by rapid regulation of surface receptor levels. CME is also critically involved in serum homeostasis by regulating the

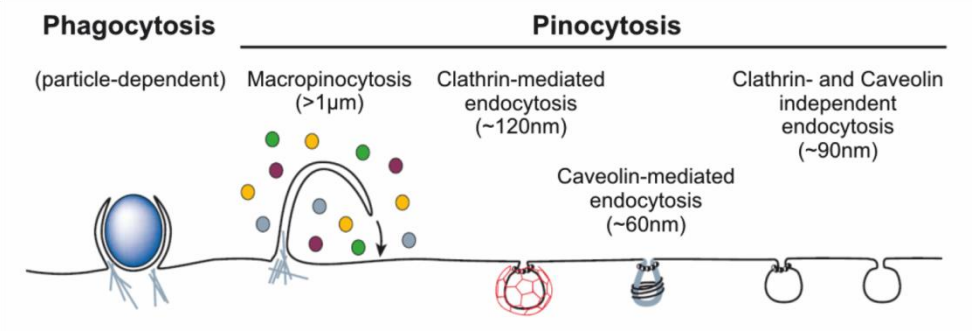

Figure 1.5 Endocytic pathways of extracellular particle uptake. Endocytic uptake routes differ with regard to the size of the endocytic vesicle, the nature of the cargo (ligands, receptors, and lipids) and the mechanism of vesicle formation. Pinocytic release and uptake represent crucial components of cell homeostasis and inter-cellular crosstalk. Receptor-mediated phagocytosis is limited to professional phagocytic cells of the immune system such as DCs and macrophages. Modified from Doherty and McMahon, 2009[126].

internalization of membrane pumps that control the transport of small molecules and ions across the plasma membrane[128]. CME involves the concentration of high-affinity transmembrane receptors and their bound ligands into 'coated pits' on the plasma membrane, which are formed by the assembly of cytosolic coat proteins, the main assembly unit being clathrin[129]. Coated pits invaginate and pinch off to form endocytic vesicles that are encapsulated by a polygonal clathrin coat and carry concentrated receptor-ligand complexes into the cell.

Caveolae-mediated endocytosis has been shown to be involved in the confinement of cholesterol and sphingolipid-rich microdomains of the plasma membrane, thereby contributing to overall lipid homeostasis[130].

Clathrin- and caveolin independent endocytosis are characterized by 40-50 nm cholesterol-rich rafts. Their unique lipid composition provides a physical basis for specific sorting of membrane proteins and/or glycolipids based on their transmembrane regions[131,132]. These small rafts can presumably be captured by, and internalized within any endocytic vesicle.

The second mechanism of endocytosis, namely phagocytosis, is involved in the clearing of pathogens, large debris and apoptotic cells[133]. Only professional phagocytes of the immune system such as monocytes, macrophages, and DCs are capable of employing this receptor-dependent mechanism of uptake and subsequent signaling. This highly regulated process involves specific cell surface receptors with redundant and non-overlapping recognition

repertoires[134], signaling cascades mediated by Rho-family GTPases and strong reorganization of the actin cytoskeleton[135].

1.7 Pathogen Recognition Receptor Repertoire of Immune Cells

Pathogens are typically decorated by antibodies, complement factors, and mannose-binding lectin in a process called opsonization. In combination with PAMPs present on their surface structures, cell binding and pathogen uptake is facilitated. These processes are mediated by immunoglobulin receptors (FcRs), complement receptors, and the mannose receptor[136].

Furthermore, evolution has led to the formation of PRRs that are capable of recognizing evolutionary conserved structural motifs on i.e. bacteria and viruses[43]. These include scavenger receptors (SRs), lectins, and TLRs, that are capable of enhancing cellular binding and trigger a defined intracellular signaling cascade that initiates an appropriate immunological response[92,137]. Evolutionarily conserved receptors are widely expressed on virtually all immune cells. PRRs represent the arm of the innate immune defense system through sensing evolutionary conserved structures present on e.g. bacteria and viruses such as sugar residues, bacterial cell wall components, and DNA/RNA molecules. Up to now, four different classes of PRR families have been identified. These include transmembrane proteins such as the TLRs, C-type lectin receptors (CLRs), and cytoplasmatic proteins such as the retinoic acid-inducible gene RIG-I-like receptors (RLRs) and NOD-like receptors (NLRs)[138].

The toll-like receptor family represents one of the best characterized PRR family. It recognizes a vast number of bacterial and viral protein moieties both on the cell surface and within confined endosomal vesicles. First discovered in Drosophila, the Toll protein was found in both immune and non-immune cells of vertebrates, including fibroblasts, epithelial and endothelial cells[139]. Each TLR recognizes its specific ligand(s) and has a specific sub-cellular localization. TLR1, TLR2, TLR4, TLR5, TLR6 and TLR11 are located on the cell surface, whereas TLR3, TLR7, TLR8 and TLR9 are found in endosomal compartments (**Figure 1.6**)[139,140]. At least eleven members of the TLR family have been identified in mammals[141].

TLRs are characterized by N-terminal leucine-rich repeats and a trans-membrane region followed by a cytoplasmic Toll/IL-1R homology domain (TIR). All TLRs except TLR3 signal through a cardinal adaptor protein called myeloid differentiation primary response 88

(MyD88). TLR3, however, signals exclusively through the TIR-domain-containing adaptor inducing IFN-ß (TRIF) protein. TLR4, which mainly recognizes LPS, induces a dual signaling pathway involving both MyD88 and TRIF[142,143].

In innate immune cells, stimulation of TLRs activates transcriptional factors including NF-κB

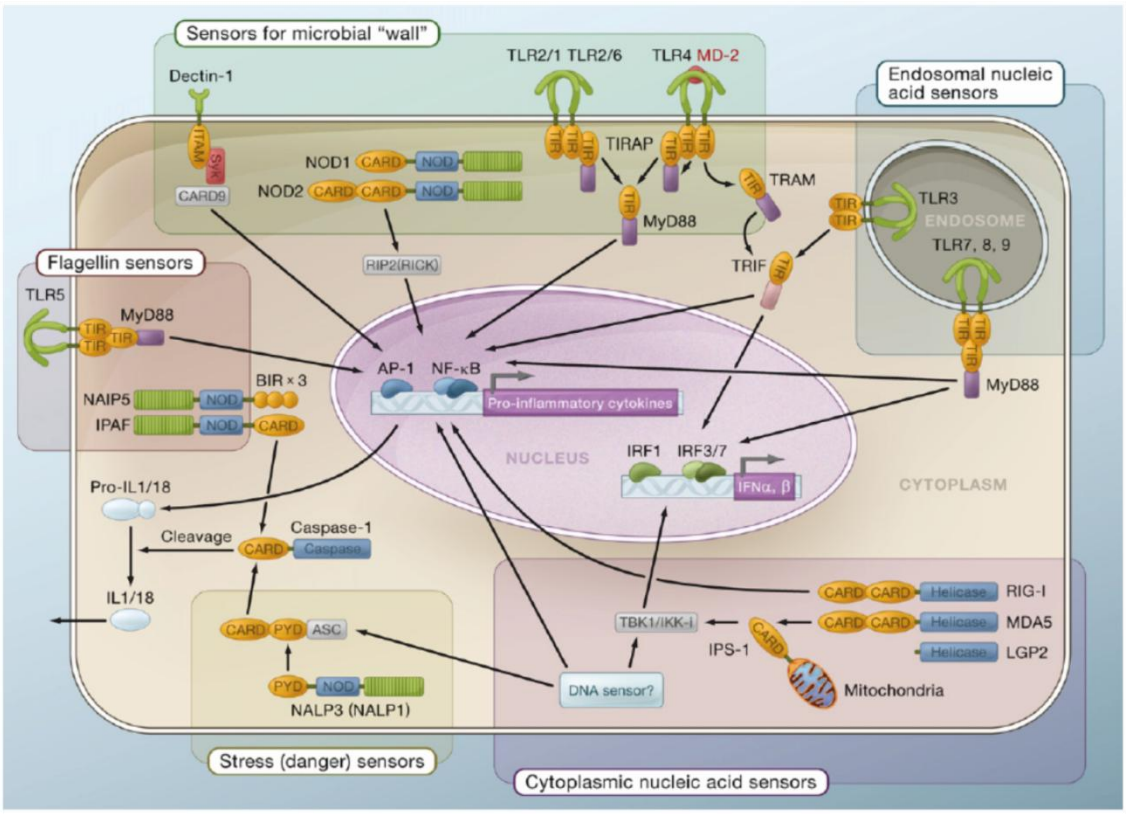

Figure 1.6 PRRs and their intracellular signaling mechanisms. Recognition of PAMPs and DAMPs lead to the induction of discrete NF-κB-related signaling events that result in the secretion of a distinct cytokine repertoire. Various membrane-bound as well as intracellular receptors displayed sense different forms of exogenous and endogenous danger signals. Adopted from Ishii et al., 2008[137].

which results in morphological alterations, phagocytic respiratory burst, and up-regulation of co-stimulatory molecules and pro-inflammatory cytokines[92,141].

NLRs are the cytoplasmic counterparts of TLRs that recognize a set of cytosolic PAMPs and endogenous ligands and induce the activation of NF-κB in a TLR-independent manner[144,145]. Among the 14 members of NLRs belonging to the NACHT, LRR and PYD domains-containing protein (NALP) family, NALP1 and NALP3 are the most significant. These NALP proteins contribute to the assembly of a structure termed inflammasome, which is crucial for the processing and activation of caspase-1[146]. NALPs regulate the production and release of IL-1ß, one of the most important pro-inflammatory cytokines, by recruiting the adaptor protein ASC (apoptosis-associated speck-like protein containing a CARD)[147,148]. It has been

shown that bacterial and viral RNA induce IL-1ß and IL-18 secretion in murine macrophages in a NALP3-dependent manner[149,150].

Cytoplasmic RIG-I-like RNA helicase (RLH) receptors are involved in TLR-independent recognition of dsRNA, which results in activation of IRFs and NF-κB transcription factors[151]. The RIG-I receptor recognizes the 5'-triphosphate terminus of viral RNA that is usually capped by adding 7-methylguanosine during posttranslational RNA modifications in eukaryotes[152]. Therefore, "self" RNA does not trigger receptor detection[153].

Through the aid of these various PRRs, immune cells are capable of "sensing" foreign or potentially harmful structural moieties and initiate appropriate counter-measures. It can be envisioned that exogenous substances such as magnetic nanoparticles employed in molecular imaging techniques are detected in similar ways. Furthermore, surface functionalization responsible for the recognition, subsequent cellular uptake and vector accumulation within target tissues are designed to fulfill a specific imaging or treatment goal. Therefore, modern research aims at endowing imaging or therapeutic probes with recognizable surface ligands. These structures either mimic PRR ligands or are designed to avoid cellular uptake that leads to prolonged circulation times through evading immune detection, and thus, allow enhanced imaging.

1.8 Nano-Bio Interface(s)

Recently, interdisciplinary research has been evaluating the possible impacts of various interfaces that emerge at the intersection of nanoparticles and biological entities such as media and cellular membrane structures[154]. Most importantly, it is believed that these interfaces alter the properties of the MNP being employed, including overall size and surface properties due to protein absorption and resorption effects. The nano-bio interface comprises three dynamically interacting components, namely (i) the nanoparticle surface, which characteristics are determined by its physico-chemical composition, the (ii) solid-liquid interface and the changes that occur when the particle interacts with components present in the surrounding medium, and (iii) the solid-liquid interface contact zone with biological substrates or structures of cellular membranes (as illustrated in **Figure 1.7**)[155].

The basis of the underlying forces ultimately resulting in a change of surface parameters on MNP formulations rely on physico-chemical molecule interactions between particle shell

components, soluble proteins and other reactive molecules. Van-der-Waals, electrostatic, solvation, solvophobic and depletion forces are considered to be critically involved in this context[156]. However, the sum of interaction forces is subject to change depending on temporal interaction kinetics, fluid mechanics and molecular localization patterns[157].

Understanding these physical and chemical properties is crucial when optimizing contrast agents for molecular imaging techniques in the future. Targeted approaches solely rely on the

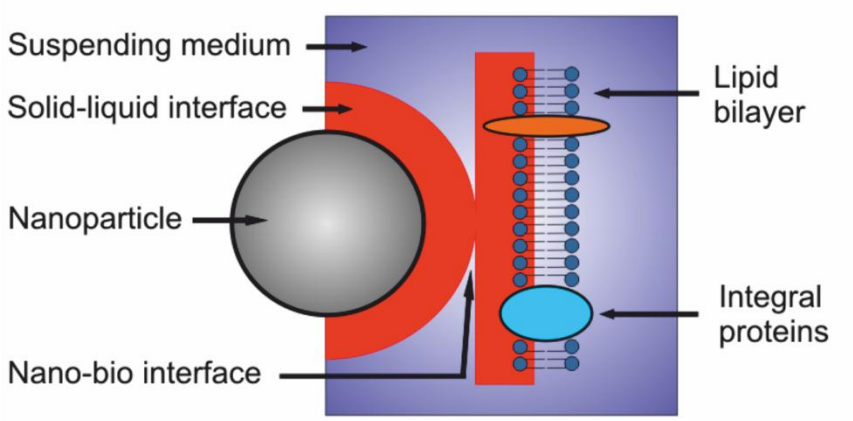

Figure 1.7 Components comprising the Nano-bio interface. Graphical visualization of the various interfaces between MNP surface structures and biological entities such as proteins (serum fluids, cell culture media). Both particle surface and external cell membrane structures are covered with a biofilm of proteins that dramatically shape and alter chemical MNP properties. Various forces exerted from MNPs, cellular structures and surrounding molecular components shape the overall interaction potential. Modified from Nel et al., 2009[155].

surface characteristics of employed nanomaterials to be interacting with designated target structures on specialized cell types or tissue components. Therefore, nanoparticle surface characteristics have to be designed accordingly to either (i) evade the formation of protein soft-shells around MNP formulations that could potentially shield reactive sites important for cellular recognition and uptake, or (ii) exploit protein adhesion through promoting the binding of specific soluble factors beneficial for subsequent cellular and/or tissue accumulation. “Stealth” particles covalently decorated with molecules such as PEG have been shown to avoid protein accumulation around contrast agents whilst in circulation, and thus, extend half-life and imaging times during MRI scans[12,158]. On the other hand, MNPs being opsonized by the actions of serum constituents are cleared from the biological system rather quickly, thus reducing both vector accumulation times and resulting imaging performance[159].

However, scientists are just beginning to fully comprehend the mechanisms involved in particle decoration, resulting alteration of designed MNP properties, and the modified cellular interactions resulting as a consequence[156,160]. Further knowledge has to be attained to ensure

MNP functionality, and consequently, imaging characteristics to further improve medical diagnosis and treatment in the future.

1.9 Aim of the Study

Engineered magnetic nanoparticles are currently emerging as promising tools in numerous applications for medical therapy and diagnostics including the development of drug delivery systems and contrast agents for magnetic resonance imaging. *In vitro* labeling of target cell populations with MNPs before therapeutic implantation shows great promise in monitoring successful cell engraftment, differentiation and migratory behavior using MRI. Depending on the desired therapeutic treatment outcome, these biological processes remain critical for the success of such cell-based therapies.

Hematopoietic stem and their derived precursor cells are particularly effective targets for cell-based therapies due to their plasticity and ability to reconstitute the entire cell pool of the hematopoietic system in both steady-state and disease. On the other hand, terminally differentiated immune cells represent optimal labeling agents due to their potential to initiate appropriate immune responses within the host. In combination with molecular probes, these cells are already being used in clinical research applications. However, the principles governing cellular interactions with MNPs that lead to the recognition, subsequent uptake and resulting imaging properties are largely unknown.

Therefore, the primary objective of this study was to investigate uptake characteristics of synthetic MNPs of various origins and surface modifications into HSCs and their downstream effector cells including DCs and macrophages. This included LbL-synthesized nanoparticles, lipid-shell coated MNPs, covalently functionalized and biogenic magnetosome MNPs. Through altering chemical properties of employed MNPs such as overall particle size, surface charge, and shell chemistry, a solid experimental platform was generated to study the involvement of these parameters in the context of cellular interactions and subsequent uptake processes. Since MRI properties are based on the capacity of MNPs to alter their immediate proton environment, TEM studies of labeled immune cells were performed prior to assessing contrast agent potential using MRI.

Immunogenicity of medical probes such as MNPs remains of great interest to current research. Shaping reactive MNP moieties to confer (i) receptor-mediated uptake and subsequent

signaling, or (ii) evasion of clearance mechanisms represent powerful tools to enhance imaging and targeting of specialized cell types or tissues in both health and disease. To address these concepts, possible PRR involvement in the recognition and signaling after MNP exposure was addressed through employing discrete knockout models. Phenotypic alterations arising as a direct consequence of particle uptake were investigated through assessing both the cell surface molecule repertoire as well as the release of pro-inflammatory cytokines, which both represent a direct consequence of primary immune reactions.

We expect these findings to be highly valuable in understanding MNP-cell interactions that ultimately shape molecular imaging characteristics.

2 Materials and Methods

2.1 Materials

2.1.1 Cell Culture Media and Supplements

2.1.1.1 Cell Culture Media

If not otherwise indicated, all cell culture media were purchased from Invitrogen.

Basic DC and splenocyte growth medium:
RPMI 1640 containing 2 mM l-glutamine, 100 U/ml penicillin, 10 µg/ml streptomycin (all Invitrogen), 50 µM β-mercaptoethanol (Sigma-Aldrich), and 10% FCS (PAA, heat inactivated for 20 min at 42°C (core temperature)).

Basic macrophage growth medium:
DMEM containing 100 U/ml penicillin, 10 µg/ml streptomycin, 50 µM β-mercaptoethanol, and 10% heat-inactivated FCS.

Serum-free DC medium:
Gibco Macrophage-SFM medium supplemented with 100 U/ml penicillin, 10 µg/ml streptomycin.

2.1.1.2 Growth Factors

Growth factor	Source
GM-CSF, murine	Peprotech, Produced in E. coli in house or purchased from Pharmedartis GmbH, Aachen *[1]
IGF-1, long range human	Sigma-Aldrich
IL-6/IL-6 receptor fusion protein	provided by S. Rose-John, Kiel
M-CSF, human	Peprotech
SCF, murine	recombinantly produced in CHO cells *[2]
Dexamethasone	Sigma-Aldrich
Flt3L, human	Peprotech

*[1] Using plasmid pETH2aHISmGM-CSF (S.M. Kurz, PhD thesis, 2000).

*[2] Using the pETH2a HIS-mSCF plasmid (S.M. Kurz, PhD thesis, 2000).

2.1.2 Mice

C57BL/6 Wt and MyD88^{ko} mice were bred and maintained under specific pathogen free conditions in the central animal facility of the University Hospital, Aachen, Germany. MyD88^{ko}, ASC^{ko}, TLR4^{ko}, and TLR9^{ko} were bred and maintained under specific pathogen free conditions in the World Premier Institute IFReC, Osaka, Japan. Mice used for experiments were between 7-14 weeks of age. All animal experiments were approved by local authorities in compliance with the German or Japanese animal protection law.

2.2 Methods

2.2.1 Cell Culture of Primary Cells

All primary cell types were grown in a humidified incubator at 37°C and 5% CO_2 under sterile conditions. Aseptic methods as well as good laboratory practice were employed at all times to avoid possible contaminations that might potentially alter experimental outcomes.

2.2.1.1 Isolation of Murine Bone Marrow Cells

Bone marrow cell suspensions were prepared from femur and tibia of mice. Animals were anesthetized and sacrificed using cervical dislocation and incisions were made into the abdominal skin to expose hind legs. Muscle tissue was removed from bones using mechanical force and gentle scraping. Aseptic removal and disinfection of relevant bones with 70% EtOH was performed prior to flushing the red marrow using a 23G needle with basic growth medium. This process was repeated several times prior to washing twice using growth medium to obtain a homogenous single cell suspension of bone marrow cells. Cell numbers were counted employing an electronic counting device (CASY 1, Roche) and stored until further experimental procedures.

2.2.1.2 Culture of GM-CSF derived Progenitors and iDCs

After explantation, progenitor cells were seeded into 100 mm cell culture plates (Nunc) using a concentration of $2x10^6$ cells/ml in basic DC growth medium supplemented with 30 U/ml muSCF, 5 ng/ml hyperIL-6, 25 ng/ml Flt3L, 40 ng/ml huIGF-1 long range, 25 U/ml muGM-

CSF, and 1 µM Dexamethasone[101]. After three days of culture, a Ficoll-Hypaque density gradient centrifugation (PAA, density 1.077 g/ml) was performed to remove dead cells and debris from the culture. Complete exchange of growth medium was carried out every second day thereafter employing basic DC growth medium with supplemented growth factors outlined above until differentiation was initiated. Depending on experimental endpoint studies and cell numbers required, differentiation was initiated on day 5-9 of amplification. For this purpose, basic DC growth medium supplemented with 200 U/ml muGM-CSF was used. Cells were counted and seeded as before, replenishing medium and adjusting cell concentration to $2x10^6$ cells/ml. Differentiation medium was exchanged every second day thereafter as previously outlined. Cytometric analyses were performed to consistently monitor differentiation status of cells throughout the differentiation period until immature iDC phenotype was acquired on day 7-9. Endpoint experiments were conducted accordingly.

2.2.1.3 Culture of Flt3L derived Progenitors and cDCs/pDCs

Following explantation from the bone marrow, progenitor cells were seeded into 100 mm plates (Nunc) at a final concentration of $2x10^6$ cells/ml in a volume of 10ml using basic DC growth medium supplemented with 30 U/ml muSCF, 5 ng/ml hyperIL-6, 25 ng/ml Flt3L, and 40 ng/ml huIGF-1 long range[161]. After three days of culture, a Ficoll-Hypaque density gradient centrifugation (PAA, density 1.077 g/ml) was performed to remove dead cells and debris from the culture. Complete exchange of growth medium was performed every second day thereafter employing basic DC growth medium with supplemented growth factors outlined above until differentiation was initiated on day 7 of culturing. For this purpose, Flt3L-derived progenitors were seeded into 6-well plates on day 0 of differentiation using a concentration of $1x10^6$ cells/ml (2 ml final volume) in basic DC growth medium supplemented with 100 ng/ml Flt3L[161]. Differentiation medium was partially exchanged without disturbing cell clusters on day 3 and 5 of culturing. Phenotypic progression was monitored using FACS starting on day 5 of culturing. On day 7, cells were pooled and seeded into appropriate culture dishes prior to experimental stimulation. Experimental endpoint studies were carried out on day 8 accordingly.

2.2.1.4 Cell Culture of Macrophages

1-step bone marrow derived macrophages were cultured in the presence of M-CSF. Isolation of bone marrow progenitor cells was conducted as outlined in 2.2.2.1. No Ficoll density gradient was performed on day 3 of culture due to adherently growing target cells and lack of amplification period in this culturing system. Instead, red blood cell lysis was carried out after obtaining single cell suspensions from bone marrow explants according to manufacturer's guidelines (ACK Buffer, Lonza) after explantation. Subsequently, cells were seeded at $1x10^6$ cells/ml in a total volume of 2 ml of basic macrophage growth medium supplemented with 20 ng/ml human M-CSF onto 12-well plates. Macrophage growth medium was exchanged without disturbing adherently growing cells on day 3 and 5 of culturing. On day 5, cells were gently flushed twice using 1 ml of PBS to remove loosely attached and suspending cells (unwanted DC precursors) prior to the addition of supplemented macrophage growth medium as previously outlined. On day 7, cells were washed again using PBS and resuspended in macrophage growth medium in addition to stimulating the bulk culture with MNPs and respective controls. Cells remained in identical plastic dishes during the entire course of differentiation to avoid growth delays and potential cell death arising as a result of dislodging and re-seeding of adherently growing cells. Prior to gentle cell detachment using acutase (Millipore) according to manufacturer's guidelines on day 8, cell supernatant was collected and frozen for further ELISA studies. To ensure the completion of the dislodging process, cells were periodically monitored under the microscope until all cells were in suspension. Macrophages were washed twice with growth medium to terminate the action of acutase. Cytometric evaluation of macrophage lineage and activation markers was performed thereafter.

2.2.1.5 Explantation and Culture of Primary Splenocytes

Animals were sacrificed employing cervical dislocation after being anesthetized. Spleen was carefully explanted without compromising organ integrity. After explantation, spleen tissue was mechanically dissociated and passed through a 70 µm cell strainer to exclude connective tissue. To obtain a single cell suspension thereafter, cells were repeatedly passed through a 23G needle and washed several times in washing buffer (PBS + 2% FCS) before red blood cell lysis was performed according to manufacturer's guidelines (ACK Buffer, Lonza). After

several washing steps using basic DC growth medium, cells were kept at +4°C until further experimental procedures.

2.2.2 Nanoparticle Synthesis and Characterization

2.2.2.1 Synthesis of Poly-Electrolyte coated MNPs

Poly-electrolyte MNPs were all designed and synthesized using Layer-by-Layer technologies in the Institute of Physical Chemistry, RWTH Aachen, Germany. Experimental procedures were carried out by Wong and co-workers as outlined in the following sections[162].

2.2.2.1.1 MNP Core Synthesis

In order to synthesize MNP core structures, the following adapted co-precipitation technique was employed. A Fe^{3+} solution was prepared by dissolving 4.86 g ferric chloride hexahydrate ($FeCl_3 \cdot 6H_2O$, Sigma-Aldrich) in 30ml distilled water as well as preparing an Fe^{2+} solution by dissolving 2.98 g ferrous chloride tetrahydrate ($FeCl_2 \cdot 4H_2O$, Sigma-Aldrich) in a mixture of 10ml water and 1.5 ml 37% hydrochloric acid. Both solutions were placed in an ultrasonic bath for 5min to homogenize the mixture. The Fe^{3+} and Fe^{2+} solutions were then mixed and allowed to stand in the ultrasonic bath for 2 min just prior to precipitation. To precipitate the iron oxide, the resulting mixture of Fe^{3+} and Fe^{2+} was added drop-wise to a flask containing 240 ml water and 60 ml 25% NH_3 under vigorous stirring (500 rpm). A black suspension was formed immediately and MNP formation was allowed to proceed for 30 min at RT with constant stirring to produce a stable, water-based suspension. Aggregates were first separated from the reaction mixture using a strong magnet, and subsequently washed three times with 0.3M NH_3 solution. The washed precipitate was peptized by washing twice with 60 ml of 2M HNO_3 solution. Peptizing is the process by which anionic charges on the nanoparticle surface are neutralized. Three cycles of centrifugation at 5000 rpm for 10 min were carried out and the precipitate dissolved in 120 ml of ddH_2O water to yield a stable ferrofluid. Exposure of this ferrofluid to a magnetic field revealed no phase separation, confirming a complete re-dispersion. This unmodified MNP is positively charged.

Furthermore, MNPs on the basis of the fluidMAG technology were employed to serve as core particle structures in subsequent coating steps (kind gift from ChemiCell GmbH). Negatively

charged fluidMAG-PAS (carboxylated (COO^-) terminal groups) and fluid-MAG-PS (sulfonated (SO^{3-}) terminal groups) were employed in coating strategies using positively charged polymers. On the other hand, positively charged fluidMAG-Q (terminal amino (R_4N^+) groups) and fluid-MAG-UC/C (cationic (O^+) terminal groups) MNPs were used in case of negatively charged poly-electrolyte coating strategies.

2.2.2.1.2 LbL Assembly of Poly-Electrolytes around Fe Cores

Layer by layer technology was adopted to deposit opposingly charged layers of poly-electrolytes onto charged core MNPs previously discussed. Positively charged MNPs were coated with poly(styrene sulphonate) (PSS, MW 70 kDa, Sigma-Aldrich) and negatively charged MNPs were modified with poly(diallyldimethylammonium chloride) (PDAD, MW 100-200 kDa, Sigma-Aldrich) or poly(ethyleneimine) (PEI, MW 750 kDa, Sigma-Aldrich). In principle, 20 ml of a 1:100 diluted dispersion of MNPs (either positively or negatively charged) was added to 40 ml of an aqueous solution (conc. 1 g/l) of the oppositely charged polyelectrolyte to prepare the initial layer. The solution was first allowed to mix in an ultrasonic bath for 30 min. To ensure that saturation adsorption of the poly-ions on the colloid particles was reached, additional incubation for 12 h was performed. The products were separated from the excess poly-electrolyte twice through magnetic separation. The precipitate was briefly subjected to an ultrasonic treatment to yield a stable solution.

Dextran sulfate (Dex, MW 100 kDa, BioChemica) and chitosan (Chit, MW 50-190 kDa, 85% deacetylated, Sigma-Aldrich) represent weak poly-electrolytes, whose degree of charge can be varied according to the pH. Dextran (pKa ~ 4.0) was diluted in an aqueous solution without pH adjustment (pH ~ 6), thereby ensuring its negative charge. Chitosan is a cationic polymer containing 15% N-acetyl-D-glucosamine. A solution was obtained by dissolving chitosan in an aqueous solution of 25% acetic acid (pH ~ 1.3). The pKa of chitosan is ~ 6.0, ensuring that the chitosan prepared is positively charged and thus endows MNPs with a positive surface layer. LbL assembly of dextran and chitosan was performed just as described for the synthetic poly-electrolytes[162].

2.2.2.2 Oleate-Stabilized MNPs

Lipid shell MNPs employing sodium oleate as stabilizing shell component were designed and synthesized in the Institute for Applied Medical Engineering (AME), RWTH Aachen, Germany. Superparamagnetic magnetite lipid–shell core MNPs were obtained by co-precipitation of Fe^{2+} and Fe^{3+} ions with NH_3. Stabilization was achieved using cis-9-octadecenoic acid sodium salt (oleate). Experimental procedures were carried out by Hodenius and co-workers as outlined in the following sections[163].

2.2.2.2.1 Synthesis of Fe Core Particles

Initial core particle synthesis followed a technique previously published by Khalafalla and Reimers[164]. 8.25 ml starting volume of an aqueous solution that contains 2 g $FeCl_3$ x $6H_2O$ (7.5 mmol) and 1 g $FeCl_2$ x $4H_2O$ (5 mmol) resulted in a Fe^{3+}/Fe^{2+} molar ratio of 3/2. Subsequently, 4.18 ml of a 25% NH_3 solution was added drop-wise at RT under continuous stirring. Iron oxide was formed immediately, resulting in a black, magnetizable suspension. The reaction mixture was stirred for an additional 5 min to allow completion of the reaction. The black precipitate was separated from the clear supernatant by magnetic decantation.

2.2.2.2.2 Oleate-stabilized Ferrofluids

After removal of the excess chloride ions, stabilization of the individual iron oxide cores was achieved through peptization using cis-9-octadecenoic acid sodium salt (oleate). In practice, 0.75 g sodium oleate (2.5 mmol) was added to the iron oxide precipitate, heated to 90°C, while stirring with a glass rod for 5 min. After peptization with oleate, transformation of the iron oxide cores into colloidal particles of ferrofluid was completed by a sonication treatment (titanium probe-tip sonicator UP 200 S, Hielscher).

2.2.2.3 Bacterial Magnetosomes

Magnetosomes were isolated and purified from an actively growing magnetotactic bacterial strain *Magnetospirillum gryphiswaldense* MSR-1 (DSM6361) by Schueler and colleagues in the Institute of Microbiology, LMU, Munich, Germany. Experimental procedures followed a

protocol previously described by Gruenberg et al.[165,166]. The strain was grown under microaerobic conditions in an oxystat fermentor.

Experimental conditions used to isolate magnetosomes followed the protocol previously described, with minor modifications. Briefly, 10 g (wet weight) of *M. gryphiswaldense* cells suspended in 50 ml of 50 mM HEPES – 4 mM EDTA (pH 7.4) was disrupted by three passes through a French pressure cell (20000 lb/in^2). All buffers used for magnetosome isolation contained 0.1 mM phenyl-methyl-sulfonyl-fluoride (PMSF) as a protease inhibitor. Unbroken cells and cell debris were removed from the sample by centrifugation (5 min, 680 x g). The cell extract was passed through a MACS magnetic separation column (Miltenyi). Columns were placed between two Sm-Co magnets, which generated a magnetic field that magnetized the column wire matrix and produced strong magnetic field gradients near the wires that resulted in entrapment of the magnetic particles. Bound magnetic particles were initially rinsed with 50 ml of 10 mM HEPES – 200 mM NaCl (pH 7.4) followed by 100 ml of 10 mM HEPES (pH 7.4). After removing the column from the magnet, magnetic particles were eluted from the column by flushing with 10mM HEPES buffer. Finally, the magnetosome suspension was loaded on top of a sucrose cushion (55% (wt/wt) sucrose in 10mM HEPES (pH 7.4)) and subjected to ultracentrifugation in a swinging bucket rotor. The pellets were analyzed by SDS-polyacrylamide gel electrophoresis (PAGE) after extensive washing and re-suspended in buffer solution and stored under N_2 atmosphere until further use.

2.2.2.4 Synthesis of Covalently linked "Stealth" MNPs

Covalently linked "stealth" particles were designed and synthesized in the Department of Nanobiotechnology, Laboratory for Supramolecular Materials, ETH Zurich, Switzerland. Additional details of the experimental design used to generate particle formulations have been published in Amstad et al., 2009[167,168,169].

2.2.2.4.1 Synthesis of Iron Oxide Core MNPs

To synthesize iron oxide MNPs by aqueous precipitation methods the protocol established by Massart was followed[170]. A typical batch was synthesized out of 198.8 mg (1.2 mmol) $FeCl_2$ and 540.6 mg (2.3 mmol) $FeCl_3$. Black precipitates indicated the immediate iron oxide MNP formation after the pH was shifted >10 using concentrated NaOH. The resulting MNPs were

neutralized through washing with 10 mM HEPES solution. To accelerate MNP agglomeration especially at high pH used to electrostatically stabilize MNPs, 160 mM NaCl was added to the HEPES buffer.

2.2.2.4.2 Synthesis of Anchor Moieties and Functional Groups

Synthesized core MNPs were stabilized within 4 h after the synthesis was completed. To a typical batch of iron oxide MNPs obtained from 1.2 mmol $FeCl_2$ and 2.3 mmol $FeCl_3$, 24 mmol of PEG(0.55)-gallol or PEG(5)-gallol dissolved in 25 ml Millipore water was added. MNPs were dispersed in this solution by pulsed sonication (5 min, P = 10^5 / cm^2, pulse frequency = 1 s on, 1 s off, UP260s, Hierschler GmbH). To stabilize MNPs with a mixture of biotin-PEG(3.4)-gallol and mPEG(0.55)-gallol, 25 ml Millipore water containing 2.4 mmol of the former dispersant was added to uncoated MNPs before they were sonicated and back-filled with 21.6 mmol mPEG(0.55)-gallol. MNPs were sonicated a second time according to the above described procedure. Excessive dispersants were removed by ultracentrifugation using a filter with a cut-off of 30 kDa (vivaspin, Epson). The filter cake was re-suspended in Millipore water before the dispersion was freeze-dried. MNPs were re-suspended in PBS, HEPES or Millipore water, sonicated for 30 min, and centrifuged for 10 min at 25000 x g (Eppendorf centrifuge 5417R) to eliminate agglomerates. The dispersed MNPs in the supernatant were freeze-dried a second time.

Since especially PEG-based dispersants are poorly soluble in EtOH, they were first aliquotted in DMF at a concentration of 100 mg/ml. This dispersant solution was pipetted into an eppendorf tube containing EtOH or DMF, respectively, before the MNP dispersions were added. MNPs were stabilized at 50°C for 24 h under constant mechanical stirring. MNPs which were functionalized e.g. with biotin or acrylate terminated dispersants were first incubated with the functionalized dispersants (10 mol % unless stated otherwise) at 50°C for 30min under constant mechanical stirring at 500 rpm. Un-functionalized dispersants were added to this dispersion and MNPs were incubated for another day at 50°C under constant mechanical stirring at 500 rpm. To exchange EtOH with water and to partially remove excessive dispersants, stabilized MNPs were dialyzed for 24 h against Millipore water. Approximately 5 ml MNP dispersion was dialyzed against 50 ml Millipore water and the Millipore water was exchanged twice. Fe_3O_4 MNPs synthesized were dialyzed using 14-16 kDa cut-off dialysis tubings (Spectra/Por dialysis membrane, spectrum labs).

Synthesized MNPs were stabilized within 6 h after the MNP synthesis was completed. 6 mg palmityl-nitroDOPA dissolved in DMF at a concentration of 100 mg/ml was added to 0.5 ml EtOH before 0.5 ml of the Fe_3O_4 MNPs synthesized was added. Palmityl-nitroDOPA was adsorbed for 24 h at 50°C under constant mechanical stirring at 500 rpm (Thermomixer comfort, Vaudaux-Eppendorf). To remove excessive dispersants, MNPs were washed three times by centrifugation for 30 min at 14000 rpm before the supernatant was exchanged with 1 ml fresh EtOH. MNPs were centrifuged a fourth time where EtOH was exchanged with 1 ml Millipore water before these MNPs were freeze-dried.

Acrylated MNPs were functionalized similar to biotinylated MNPs. Briefly, iron oxide core particles (synthesized as previously described herein) were stabilized with 10 wt% (0.6 mg dispersant per mg MNP) acrylate-PEG-nitroDOPA in EtOH at 50°C for 30 min prior to back-filling using 90 wt% (5.4 mg dispersant per mg MNP) mPEG-nitroDOPA. Dispersants were adsorbed onto the MNP surface for 24 h and washed thereafter employing dialysis and centrifugation as previously outlined before freeze-drying MNPs for further use. A 1:1.5 molar ratio of MNP to CpG was finally used to functionalize acrylated MNP moieties. Particles and CpGs were mixed and incubated at 30°C for 24 h. Magnetic separation at 4°C for additional 24 h was employed thereafter to purify particle solutions. The resulting clear supernatant containing Millipore water and unbound CpG was carefully removed and an equal amount of fresh H_2O was added prior to resuspending particles. This washing process was repeated a total of three times.

2.2.2.5 MNP Characterization

The zeta (ζ-) potential and hydrodynamic diameter (D_h) of MNP formulations were measured and calculated by cumulant fits using a Zetasizer 3000HS (Malvern) at 25°C with a dilute dispersion of the MNP in pure water.

2.2.3 Cell Labeling with MNPs

Sterile solutions of MNPs were sonicated for 30 min prior to cell labeling and used at a final iron concentration of 10 μg/ml if not otherwise indicated. DC subsets were seeded at $2x10^6$ cells/ml and incubated with respective MNPs for 24 h. In case of adherently growing macrophage populations, semi-confluent dishes were labeled on day 7 of culturing,

corresponding to approximately 80% of confluence. $1x10^6$ explanted mixed splenocytes were labeled in a total volume of 1ml. Cells were harvested by gentle pipetting and subsequent centrifugation (1400 rpm, 4 min) and washed in PBS containing 2% FCS for further experimental procedures. In case of macrophages, adherent cell populations were gently dislodged after incubation time using acutase as previously described.

2.2.4 MACS Cell Sorting

MNP-labeled cell populations were subjected to magnetic separation to evaluate uptake properties (MACS, Miltenyi Biotech) as previously reported[171,172]. After 24 h of MNP exposure, cells were extensively washed twice in MACS buffer (PBS + 2% FCS) to remove unbound particles from suspension prior to their application onto magnetic columns. Cells were resuspended in 1 ml of buffer and gently applied to magnetic columns. Columns were subsequently washed twice using 500 µl of buffer solution containing unlabeled cell population. Retained cell fraction was subsequently eluted employing MACS buffer using mechanical force after removal of the magnetic field. This step was performed twice using 500 µl for each elution step. Both fractions were counted using a cell counting device (CASY 1, Roche) and stored at 4°C until further use.

2.2.5 Cell Viability Assays after MNP Exposure

2.2.5.1 MTT Assay

Cytotoxicity of MNP labeled bulk cultures was evaluated using a photometric MTT assay. Progenitors and differentiated DCs were seeded in 24-well plates at a concentration of $1x10^5$ cells/ml and incubated with MNPs for 24 h. To assess cell viability, MTT reagent (3-[4,5-dimethylthiazol-2-yl]-2,5-diphenyl tetrazolium bromide, Sigma-Aldrich) was added to cell culture for an incubation period of 3 h according to the manufacturer's protocol (Sigma-Aldrich). To dissolve resulting crystal structures otherwise interfering with subsequent photometric analyses, MTT solubilizing solution (10% Triton X-100 plus 0.1 N HCl in anhydrous isopropanol) was added. After dissolving crystals through rigorous pipetting, absorbance was measured at 570 nm (FLUOstar OPTIMA, BMG Labtech).

2.2.5.2 Flow Cytometric Analysis (FACS) employing 7-AAD

In order to investigate cytotoxicity of MNP formulations within labeled cell fractions alone, fluorescent 7-AAD (7-amino-actinomycin D) stainings were employed. In brief, $2x10^5$ cells were washed with PBS after incubation with respective MNPs and incubated with 50 ng/ml 7-AAD (eBioscience) for 20 min at +4°C in the dark in a total volume of 50 µl. After additional washing in PBS to remove unbound dye, cells were analyzed by flow cytometry as described in 2.2.9. Untreated cells as well as positive controls treated with 0.3% H_2O_2 for 30 min were included in the studies.

2.2.6 FerroZine Iron Assay

Intracellular iron concentration was determined using a colorimetric ferrozine iron assay as previously described[171,173]. Briefly, $1x10^6$ DCs were lysed in 100 µl 50 mM NaOH. 100 µl of a 10 mM HCl solution was added to neutralize alkaline pH. Subsequently, 100 µl of freshly prepared iron releasing agent consisting of 1.4 M HCl and 4.5% (w/v) potassium permanganate ($KMnO_4$) was added. The resulting suspension was thoroughly mixed and incubated for 2 h at 60°C under constant shaking. After cooling to RT, 30 µl of iron detecting agent (6.5 mM ferrozine, 6.5 mM neocuproine, 2.5 M ammonium acetate, and 1 M ascorbic acid (all from Sigma-Aldrich)) was added and incubated for 30 min at RT under constant shaking. Ascorbic acid is used to reduce Fe^{3+} to Fe^{2+} ions that form a chelate with ferrozine (3-(2-pyridyl)-5,6-bis(phenyl sulfonic acid)-1,2,4-triazine; Sigma-Aldrich). Neocuproine scavenges copper ions that otherwise interfere with subsequent reactions. 280 µl were pipetted into 96-well plates (Greiner, flat-bottom) and absorbance of Fe^{2+}-ferrozine was measured at 550 nm (FLUOstar OPTIMA, BMG Labtech) and compared to the absorbance of $FeCl_3$ standards. The minimum detection limit for Fe^{2+} ions was 250 µmol/l, corresponding to 5 pg of iron per cell.

2.2.7 Prussian Blue Staining

To visualize total iron uptake, $1x10^5$ cells labeled with MNPs were centrifuged (4 min at 1500 rpm) onto a glass slide using a cytospin centrifuge (Thermo Fisher Scientific). After washing in double-distilled (dd) H_2O, glass slides were subjected to Prussian blue staining using a 1:1 solution (v/v) of 10% potassium ferrocyanide $K_4[Fe(CN)_6]$ (Sigma-Aldrich) and 20% HCl for

20 min. After washing in ddH_2O, glass slides were counter-stained with Neutral Red dye (Roth) for 5 min and mounted with cover slips using mounting medium (Dako). Sample images were obtained using a Leica DM6000B microscope (Leica) and Diskus acquisition software (Hilgers). Images were processed using Adobe Photoshop and ImageJ.

2.2.8 Transmission Electron Microscopy (TEM)

Transmission electron microscopy was performed in collaboration with the TEM Facility of the Institute of Pathology at the RWTH Aachen. Briefly, $1x10^6$ magnetically sorted DCs were fixed with 3% (w/v) glutaraldehyde and embedded in 2% agarose. Samples were stained with OsO_4, embedded in Epon and cut into 70 nm thick slices. Samples were either analyzed with or without further contrast enhancement using a Philips EM 400T electron microscope at 60 kV equipped with a CCD camera (MORADA, Olympus).

TEM images were analyzed using NIH ImageJ software. Electron densities of MNP-containing sub-cellular compartments were calculated from pixel intensities within defined regions of interest (ROIs) obtained in ImageJ. Normalized values were calculated as $(signal_{MNP} - signal_{Background})$ x $area_{ROI}$ $[nm^{-2}]$. A total of 30 different MNP-containing areas within compartmental structures were evaluated.

2.2.9 Phenotypic Analysis using FACS

Flow cytometry was used to analyze cellular phenotype prior to and after experimental procedures. Single cell suspensions from different sources (bone marrow, spleen, cultured cells) were prepared for flow cytometry through extensive washing and re-suspension in FACS staining buffer (PBS supplemented with 2% FCS) prior to staining. Approximately $2x10^5$ cells were then incubated with the respective antibody combination in a volume of 50 µl for 30 min at +4°C in the dark. After repeated washing using FACS staining buffer, cell pellets were resuspended in 200 µl prior to experimental endpoint studies. Stained cells were analyzed employing FACS Calibur, FACS Canto II, or FACS LSR II Fortessa flow cytometers (BD Bioscience) and data evaluated using Cell Quest Pro, FACS Diva (BD Bioscience) or FlowJo software (Tree Star). Purified antibodies or antibodies directly conjugated to biotin, FITC, PE, PerCP-Cy5.5, PE-Cy5, PE-Cy5.5, PE-Cy7, Texas Red, APC, APC-Cy7, Alexa Fluor 700 or Pacific Blue were used. Streptavidin-FITC (eBioscience),

Streptavidin-PE (Jackson Lab), Streptavidin-PerCP-Cy5.5 (BD Bioscience) and Streptavidin-APC (eBioscience) were used to detect biotin-conjugated antibodies. Purified antibodies were detected with a secondary goat anti-rat antibody conjugated to PE (Invitrogen). Routinely, staining with the respective isotype (armenian hamster IgG, rat IgG2a, rat IgG2b, or streptavidin without primary antibody) and fluorochrome was used as control to monitor unspecific background staining.

2.2.9.1 Table of Directly Labeled Antibodies for FACS Analysis

Name	Alternative name	Clone	Company
B220	CD45R	RA3-6B2	BD, Abcam
CD11b	Mac-1	M1/70	BD, eBioscience
CD11c	Integrin-α_x	N418 or HL3	BD, eBioscience
CD80	B7.BB1	16-10A1	BD
CD86	B7.BB2	GL1	BD, eBioscience
MHC II	I-A/I-E	2G9	BD
CD3ε	CD3ε	145-2C11	BD
CD4	Ly-4	RM4-5	BD
CD8α	Ly-2	53-6.7	BD
F4/80	F4/80	BM8	BioLegend
PDCA-1	CD317	eBio927	eBioscience
Mac-3	CD107b	M3/84	eBioscience

2.2.9.2 Table of Antibodies and Secondary Reagents for Indirect FACS Stainings

Name	Specificity	Fluorochrome	Company
Biotin CD80	Biotinylated, murine CD80	-	BD
Biotin CD86	Biotinylated, murine CD86	-	BD
Biotin CD11b	Biotinylated, murine CD11b	-	eBioscience
Biotin CD11c	Biotinylated, murine CD11c	-	eBioscience
Streptavidin FITC	Streptavidin conjugated	FITC	eBioscience
Streptavidin PE	Streptavidin conjugated	PE	eBioscience
Streptavidin PE-Cy7	Streptavidin conjugated	PE-Cy7	eBioscience
Streptavidin APC	Streptavidin conjugated	APC	Invitrogen
Streptavidin eFluor 450	Streptavidin conjugated	eFluor 450	eBioscience

2.2.10 *In Vitro* Migration Assays

Transwell migration assays were performed essentially as previously described[101]. To analyze migration of DC towards a chemokine gradient after MNP exposure, $2x10^5$ cells,

which had been treated with MNPs or activated using LPS overnight, were seeded in the upper compartment of Transwell migration plate and CCL19/ELC or CXCL12/SDF-1 chemokines (100 ng/ml, Peprotech) were added to the lower compartment. Transmigration of DCs through Transwell inserts was analyzed after 90 min. In order to relate measured volume to cells counted in subsequent flow cytometric experiments, $1x10^4$ Dynabeads (equal concentration in all samples) were added to each sample retained from the lower chamber before analysis. Cells and beads were recovered and analyzed using flow cytometry by recording a fixed number of Dynabeads within each sample along migrated cells.

2.2.11 Enzyme-linked Immunosorbent Assay (ELISA)

Cytokine levels of frozen supernatant samples were analyzed according to the manufacturer's protocols (R&D Systems, Duoset® and Quantikine®). Release of pro-inflammatory molecules IL-6, IL-12p40, and TNFα as well as the functional IL-1ß were investigated. For this purpose, 96-well plates were either coated using an appropriate capture antibody (Duoset® probes) or samples were directly added into wells of a pre-coated plate (Quantikine® probes). In order to remove unbound antibodies or otherwise interfering molecules, wells were thoroughly washed using buffer solution (PBS + 2% Triton X-100) after each reaction step. After protein binding and secondary detection antibody reaction, a 1:1 mixture of H_2O_2 and tetramethylbenzidine was added. The resulting color shift due to bound HRP enzyme was measured quantitatively using a commercial plate reader (Molecular Devices) at 450 nm. The unknown protein concentration within supernatant samples was calculated in relation to the absorbance of known concentrations of recombinant protein standards.

Table of ELISA Capture Antibodies:

Detection	Specificity	Origin	Probe Set
IL-6	goat anti-mouse	R&D Systems	Duoset
IL-12p40	goat anti-mouse	R&D Systems	Duoset
TNFα	goat anti-mouse	R&D Systems	Duoset
IL-1ß	anti-mouse enzyme	R&D Systems	Quantikine

2.2.12 *Ex Vivo* Splenocyte Stimulation

Explanted splenocytes were labeled with 5 µM carboyfluoresceine diacetate succinimidyl ester (CFSE, Molecular Probes) for 10 min at RT in the dark according to manufacturer's guidelines (CellTrace^{TM}, Molecular Probes) under continuous stirring. Subsequent quenching using FCS ensured equal labeling efficiency and increased viability of target cells. CFSE-labeled splenocytes were seeded out at a concentration of $1x10^6$ cells/ml prior to MNP or control stimulation for 72 h in basic DC medium. Cells were kept in a cell culture incubator at 37°C, 5% CO_2 in the dark until further experimental procedures. After incubation, cells were prepared for counting and FACS analysis as outlined in 2.2.9.

2.2.13 Magnetic Resonance Imaging

2.2.13.1 Phantom Preparation and Immobilization of Cells

100 mm and 35 mm cell culture plates (Nunc) were used in MRI studies. For the purpose of *in vitro* phantom preparation, plates were filled with 2% agarose (Invitrogen) and allowed to solidify. Using a commercial drill (Proxxon) fitted with a stand to control drilling depth and speed, boreholes with a diameter of 3.5 mm were drilled (depth 5 mm). Residual agarose was carefully removed to avoid the formation of air inclusions in later immobilization steps. Dilution series of magnetically pre-selected labeled cells were prepared, including final phantom concentrations of 10^5, 10^4, 10^3, 10^2 cells/ml and unlabeled control populations. Appropriate cell numbers were re-suspended in 20 µl PBS and mixed with an equal volume of low-melting agarose (Lonza) at RT and carefully pipetted into defined bore holes. After solidification, holes were sealed again using 2% agarose and phantoms were stored at 4°C until final MR measurements.

2.2.13.2 MRI Scan Parameters

MR images of agarose phantoms were acquired using a Bruker Biospec 11.7 T experimental, horizontal bore MRI scanner (Bruker Biospin) equipped with actively shielded gradient coils (16 cm diameter, 750 mT/m). A purpose built transmit-receive coil (4 cm diameter) was used for image acquisition. T2 relaxation times were determined using two-dimensional multi-slice multi-echo sequences (echo spacing = 11 ms, TE = 11-176 ms, TR = 5000 ms). Relative

signal intensities were determined using T2*-weighted 3D gradient echo FLASH sequences (TE = 15 ms; TR = 200 ms; flip angle 30°; Field-of-view 3.8 x 3.8 x 0.65 cm; isotropic resolution 74 μm).

2.2.13.3 MRI Data Analysis

MR images were processed using the Bruker software ParaVision 4.0. Numerical map scan data was fitted using the following ParaVision software algorithm: T2 relaxation = A + C * exp (-t / T2), with A representing the absolute bias, and C referring to the signal intensity. Additional image analyses and numerical calculations needed to acquire i.e. contrast-to-noise ratio (CNR) were performed using NIH ImageJ.

2.2.14 Statistical Analysis

Statistical analysis of numerical data was performed using two-tailed and unpaired Student's t test with GraphPad Prism 5.0 software (GraphPad Software Inc.). P-values below 0.05 were considered to be significant.

2.2.15 Software Employed

Microsoft Office software was employed in combination with most initial data acquisition hardware used throughout this study. GraphPad Prism 5.0 was used for primary data entries, subsequent statistical calculations, and basic figure layouts. The vector-based software CorelDraw was employed to finalize and adapt figures for best visual presentation and clarity. Adobe Photoshop and CorelPaint used for picture adaptation and noise-cancelations. In order to acquire raw numerical data sets from grey-scale and pseudo-color images, NIH ImageJ software and appropriate plugins were employed.

Hardware-based software solutions were used accordingly and are outlined in the respective experimental section above.

3 Results

3.1 Synthesis and Characterization of MNPs

Magnetic nanoparticles on the basis of iron-oxide have long been recognized as vectors for biomedical applications such as MRI[23,174]. They provide superior T2 and T2* contrast enhancement and thus contribute to an enhanced clinical diagnosis and therapeutic treatment outcome. However, even though many iron oxide contrast agents are already approved for their use in clinical diagnosis, the mechanisms of interaction with and subsequent uptake into biological entities such as cells still remain elusive today[7].

To investigate these and other crucial parameters vital for therapeutic, diagnostic and research applications to come, MNPs displaying various surface properties such as charge, chemistry, as well as overall particle size were synthesized. Surface properties of engineered MNPs were custom-manufactured to yield a wide range of parameters to be investigated in conjunction with hematopoietic cells of various nature, developmental stages and origin. Shell components of MNPs not only stabilize magnetic cores and therefore provide biocompatibility, but also shape the interaction, subsequent uptake processes and resulting imaging characteristics within biological targets. It has been demonstrated in numerous studies that these chemical properties impact on interactions with biological systems[154,175,176].

Layer-by-Layer technology (LbL) was adopted to endow MNPs with a charged surface to enhance cell membrane interactions or invoke repulsive forces. The underlying principle of this novel technology is based on the coating of charged substrates onto an already existing layer of opposingly charged surfactant, thereby altering both the chemical surface properties as well as the overall diameter of particles[162,177,178].

Both positively charged poly-electrolytes such as poly-diallyl-dimethyl-ammonium-chloride (PDAD) and poly-ethylene-imine (PEI) and negatively charged poly-styrene sulfonate (PSS) were employed. PDAD represents an organic polymer that is being industrially used to reversibly bind and immobilize anionic substances[179]. Similarly, positively charged PEI is being employed to trap anionic colloids and macromolecules such as DNA, especially within acidic and neutral pH ranges[180]. In biological applications, both compounds are being deployed as cellular adhesion and transfection agents. On the other hand, the negatively

charged polymer PSS is frequently adopted in the context of ion exchange systems crucial for distinct industrial purposes[181].

In order to demonstrate practicability and ease-of-use of this novel technology platform, poly-saccharides such as chitosan and dextran were included in this study. Both substrates are often used in clinical studies because of their inherent biological features as coating materials of MNPs[182,183].

Lipid-shell MNPs are already used in clinical practice and represent promising agents for drug delivery systems, and hence, oleate-stabilized MNPs were synthesized as control particles[184]. They are comprised of an iron core structure that is entrapped within a fluid lipid bilayer membrane consisting of oleate which confers both stability and biocompatibility[185].

The third group of nanoparticles is represented by molecules covalently bound to MNP anchor moieties such as PEG and Biotin. To investigate the impact on surface decoration

MNP	Shell structures	Type of modification	References
PEI-MNP	poly-ethylene-imine	poly-electrolyte LbL	157, 170
PDAD-MNP	poly-diallyl-dimethyl-NH_4Cl	poly-electrolyte LbL	157, 170
PSS-MNP	poly-styrene sulfonate	poly-electrolyte LbL	157, 170
Chit-MNP	chitosan poly-aminosaccharide	poly-electrolyte LbL	170
Dex-MNP	dextran poly-saccharide	poly-electrolyte LbL	170
OLS-MNP	oleate-stabilized	lipid shell	158, 166, 170
PEG 0.8kDa	poly-ethylene glycol	covalent linkage	162, 163, 164
PEG 5.0kDa	poly-ethylene glycol	covalent linkage	162, 163, 164
Biotin 1%	biotin	covalent linkage	162, 163, 164
Biotin 10%	biotin	covalent linkage	162, 163, 164
Acryl-MNP	functionable acryl-groups	covalent linkage	unpublished
Nitro-DOPA	PEG + biotin anchor	covalent linkage	162, 163, 164
MSR-1	bacterial magnetosome	biogenic nature	160, 161

Table 3.1 Summary table of MNPs and their designed shell structures. Displayed are MNP abbreviations used throughout this study and their respective chemical shell modifications. Four different categories of MNPs were employed to assess biological impact on immune target cells including poly-electrolyte MNPs, lipid-shell MNPs, particles containing covalently linked shell moieties, and biogenic bacterial MSR-1 magnetosomes. Synthesized particle formulations allowed the investigation of possible biological consequences arising as a consequence of exposure that ultimately shape resulting molecular imaging characteristics. Relevant references are displayed in right column.

density, various concentrations of coatings were synthesized and their impact recorded. Both substrates are known to avoid protein adhesion, and thus, reduce particle uptake by cells and evade systemic clearance mechanisms[186,187].

Furthermore, biogenic magnetosomes of bacterial origin were included to investigate their potential to induce immunological responses within target immune cells. These magnetic nanoparticles are synthesized within certain bacterial strains in a process called biogenesis. Respective bacteria are endowed with the ability to orientate themselves with respect to the earth's magnetic field in a process termed magnetotaxis. Substrates and synthesis modifications used to coat iron-oxide core particles are listed in **Table 3.1**.

Chemical properties of MNPs such as their hydrodynamic diameter and zeta potential are important regarding cellular interactions, in particular uptake and shuttling routes employed by cells. Therefore, the analysis of distinct chemical parameters ensured particle homogeneity prior to the engagement of further experimental procedures (**Table 3.2**). In addition, both dynamic light scattering and zeta sizing technologies allow the investigation of particle stability and mono-dispersity following particle synthesis[188,189].

MNP	Mean core diameter (nm)	Hydrodynamic diameter (D_h/nm)	Zeta potential (ζ/mV)
PEI-MNP	5	117	+ 51
PDAD-MNP	5	230	+ 50
PSS-MNP	10	165	- 53
Chit-MNP	10	n.d.	n.d.
Dex-MNP	10	n.d.	- 9
OLS-MNP	10	313	- 8
PEG 0.8kDa	5	30	uncharged
PEG 5.0kDa	5	45	uncharged
Biotin 1%	5	35	uncharged
Biotin 10%	5	40	uncharged
Acryl-MNP	5	30	uncharged
Nitro-DOPA	5	25	uncharged
MSR-1	30-45	361	- 3

Table 3.2 Physico-chemical characterization of MNP formulations. Displayed are mean core diameters of MNPs assessed through TEM as well as hydrodynamic diameter and Zeta potential measured using Dynamic Light Scattering (DLS) and Zeta Sizing technologies, respectively. Various particle sizes, net surface charges and their magnitude resulted after linkage of target moieties to core MNP structures. The potential impact on biological functions of target cell populations were subsequently investigated.

Covalently linked MNPs (Biotin, PEG) exhibited a neutral charge and very small overall diameter when compared to other MNP formulations employed in this study. All covalently linked MNPs showed a narrow size-range between 25-45 nm. In contrast, poly-electrolyte-coated MNPs varied with respect to both their size and net surface charge. PDAD displayed

an average hydrodynamic diameter of 230 nm, yielding the largest poly-electrolyte MNP. As intended, PEI and PDAD showed very high positive zeta potentials of +50 ζ/mV, endowing particles with a strong positively charged interaction surface. On the other hand, PSS proved to be highly negatively charged (-53 ζ/mV) in zeta potential measurements.

As outlined in Table 3.2, chemical parameters of Chit-MNP and Dex-MNP could not be determined successfully. During dynamic light scattering measurements, both MNPs resulted in multiple species ranging in size and net charge, thus prohibiting discrete and reproducible experimental outcomes. This finding can most likely be attributed to incomplete synthesis or particle agglomeration effects in aqueous solution.

In general, synthesized iron-oxide based MNPs provided reproducible and stable chemical properties, allowing the investigation of their interaction with specialized hematopoietic cells that ultimately shape uptake and immunological consequences.

3.2 Poly-Electrolyte and Lipid-Shell MNPs

3.2.1 Hematopoietic Progenitor Cells

Hematopoietic stem cells and their immediate downstream precursors are already in clinical use due to their therapeutic potential and plasticity to differentiate into all cell types of the blood[39]. In particular, cell replacement therapies prove to be promising therapeutic modalities in the treatment of i.e. leukemia[190,191].

Hematopoietic differentiation represents a regulated, continuous, and multi-linear process in which HSCs give rise to cells of different lineages through progressively limiting developmental options and a successive decline in self-renewal potential[192]. In this study, a myeloid $CD11b^{+}Flt3^{+}$ committed hematopoietic bone marrow progenitor cell was propagated and maintained *in vitro* using defined growth factors and culturing conditions as previously described[101].

Unlike true bone marrow resident HSCs, this amplified precursor has lost its long-term stem cell properties. However, this culturing system of explanted bulk bone marrow cells results in a homogenous population of myeloid committed progenitor cells that prove to be lacking lymphoid lineage markers such as CD3ε, CD4, CD8α, CD14, B220, and Ter119[101]. On the other hand, molecular markers conferring myeloid lineage commitment such as CD11b and

Gr-1 (Ly6C/G) are being expressed. Therefore, this experimental platform allowed a thorough investigation of the impact of MNPs on a homogenous stem cell-like progenitor population amplified to large numbers.

3.2.1.1 Cytotoxicity Studies

Biocompatibility can be defined as the ability of a biomaterial to perform its desired function with respect to a medical therapy, without eliciting any undesirable local or systemic effects within the recipient. The generation of the most appropriate beneficial cellular or tissue response, as well as the optimization of the clinically relevant performance of that therapy are thus not compromised[193,194].

Biological systems exposed to nanomaterials such as synthetic contrast agents potentially suffer from side effects elicited by components either integrated or released over time by such materials. Biodegradable macromolecules and polymers potentially trigger apoptosis, growth arrest, formation of reactive oxygen species (ROS) and similar adverse effects due to their presence[154,195]. Therefore, it remains crucial to exclude cytotoxicity within target cells by studying the degree of MNP biocompatibility prior to further experimental procedures.

For this reason, both the effect of long-term MNP-treatment of HSCs for up to 72 h on their proliferative capacity as well as possible adverse effects arising from increased contrast agent concentration of up to 200 µg/ml were tested. As outlined in **Figure 3.1**A, HSC cell counts resembling the proliferative capacity after 72 h of continuous incubation with MNP formulations did not lead to decreased population numbers when comparing different MNP formulations.

In addition, increased iron load did not yield significantly elevated rates of cell death as measured through a colorimetric MTT assay, thus proving a high degree of biocompatibility of all MNPs employed. Only Chit-MNP showed decreased numbers of surviving HSCs at very high labeling concentrations (200 µg/ml) when compared to other MNPs. However, 200 µg/ml is far beyond the standard labeling concentration of 10 µg/ml for these experimental procedures, and thus, a reduction in cell viability is to be expected and within tolerable parameters (Figure 3.1B)[196].

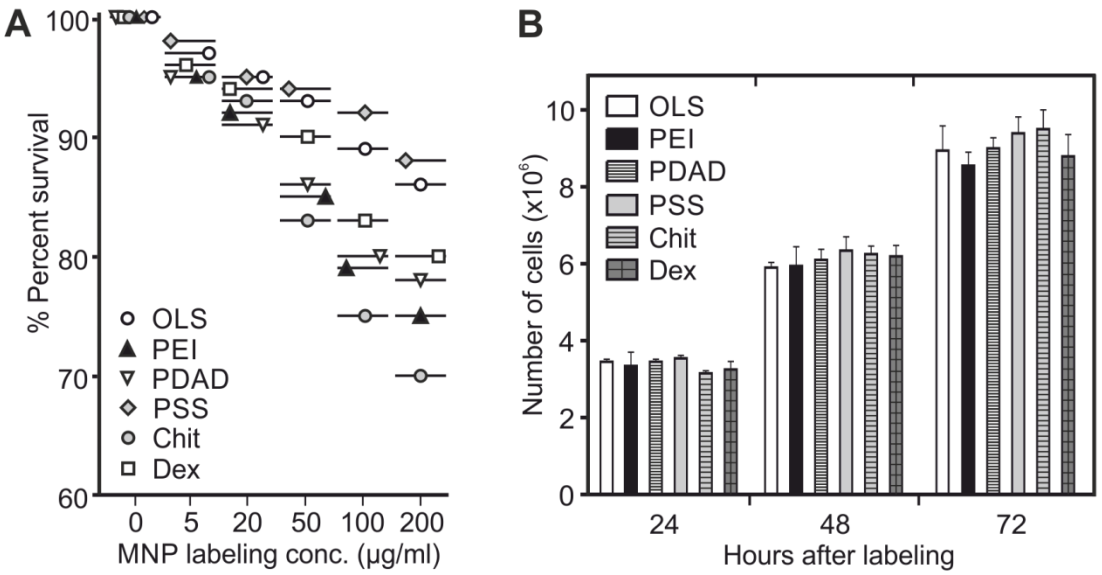

Figure 3.1 Biocompatibility studies of MNP formulations using HSCs. A) Cytotoxic effects of increasing MNP labeling concentrations on proliferating HSCs. Iron oxide concentration ranged from 0-200 µg/ml. Displayed is one representative experiment (n=3). **B)** Long-term cytotoxic assessement of MNP-labeled HSCs for up to 72 h to address possible adverse effects on cell proliferation arising as a consequence of extended MNP exposure. Target cells were seeded at $2x10^6$ prior to MNP labeling and left untreated for the remainder of the assay. Experimental data in A) used to optimize labeling concentration in further studies. Shown are mean values ± SD (n=3).

3.2.1.2 Uptake and Intracellular Iron Concentration

Due to their inherent localization and function within a biological system, HSCs and their immediate downstream progenitors are not phagocytic in nature. However, MR contrast agents need to accumulate within target cells to confer imaging potential. In order to test uptake properties of MNPs into HSCs after 24 h of incubation, both efficiency and magnitude of iron oxide particles taken up by cells were investigated. MNP labeled HSCs acquire magnetic properties after MNP integration, and thus, can be separated using an external magnetic field.

As illustrated in **Figure 3.2**A, only a fraction of cells adopted magnetic properties due to successful poly-electrolyte MNP integration. Notably, positively charged MNPs such as PEI and PDAD were taken up to a higher extent then negatively charged poly-electrolytes (PSS) and poly-saccharides (Chit-MNP, Dex-MNP). Poly-saccharide MNPs were taken up the least, with Chit-MNP and Dex-MNP yielding only 8 and 13% of labeling efficiency, respectively.

Intracellular iron content within endosomal vesicles is crucial for MR imaging properties. To investigate uptake quantity of contrast agents, a colorimetric assay on the basis of FerroZine was utilized (Figure 3.2B). This organic salt forms a stable compound with Fe^{2+} of

magnetically separated HSC lysates, and therefore, allows the quantification of the average amount of iron taken up by target cells[173].

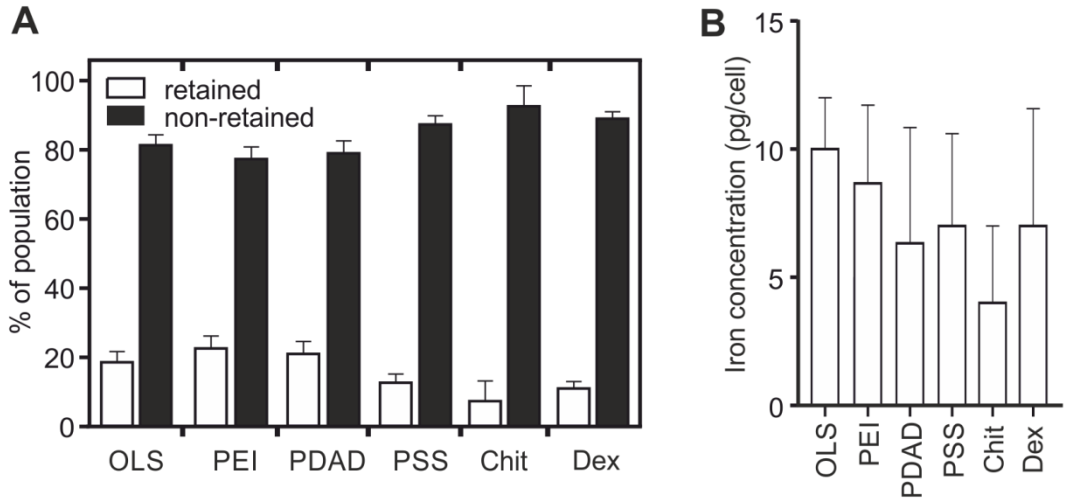

Figure 3.2 Quantitative and qualitative uptake studies employing poly-electrolyte MNPs. A) Magnetic separation techniques of HSC bulk cultures were employed to separate cell populations that acquired magnetic properties due to iron oxide incorporation from their unlabeled counterparts after 24 h of MNP incubation. Both fractions of labeled and unlabeled cells yielded total cell counts and the percentage of retained and non-retained cells was calculated. **B)** Iron assay displaying average amount of molecular iron taken up by magnetically pre-selected MNP-labeled HSCs in pg/cell. Displayed are mean values ± SD (n=3) normalized against background iron levels present in unlabeled control samples.

Quantitative measurements of previously selected cells showed an average iron incorporation of up to 5-10 pg/cell. Values depicted in Figure 3.2B were normalized against unlabeled controls. Only Chit-MNP showed slightly lower uptake quantities, however, all values are in good agreement with similar studies previously conducted[10,197]. In summary, all poly-electrolyte and lipid-shell MNPs employed were successfully taken up by HSCs, although to a lower magnitude when compared to their terminally differentiated effector cells.

3.2.1.3 Intracellular Iron Stainings

To visualize iron deposition within HSCs, Prussian blue staining was performed. This histological staining procedure is frequently employed to detect iron residues within i.e. biopsy specimens. During the course of staining, an acid solution of potassium ferrocyanide combines with ferric iron (Fe^{3+}) present in biological samples and results in the formation of a bright blue pigment called Prussian blue. This patho-histological staining technique allows the visualization of single iron granules within cells and represents one of the most sensitive detection assays for iron.

As illustrated in **Figure 3.3**, all particles proved to be localized within cytosolic structures inside HSCs. No adherence was noted on the outer membrane and within nucleic regions, confining iron deposition to the cytosol.

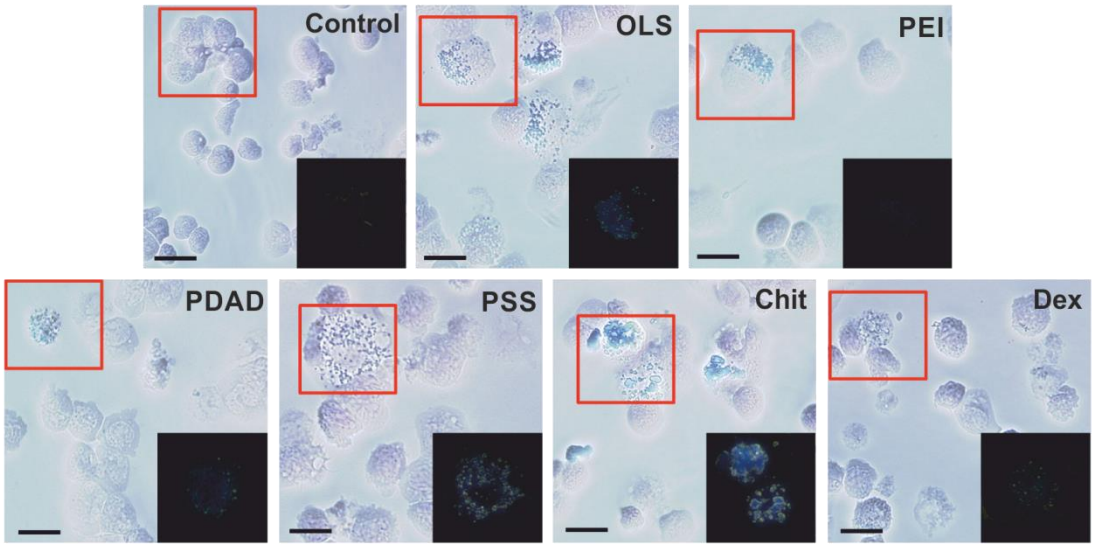

Figure 3.3 Histological iron staining of MNP labeled HSCs. Prussian blue stainings of 4% PFA-fixed cytospins that correspond to intracellular iron deposits (blue areas). Cells were centrifuged onto glass slides after harvesting and magnetic separation and subsequently stained. Counter-staining of membrane structures using Neutral Red dye prior to mounting (pink areas). Boxed areas shown in upper left corner are displayed using dark field microscopy (400x). Scale bars 20 µm.

However, larger aggregates were formed in case of Chit-MNP, most likely due to agglomeration effects prior to cellular uptake. Due to their size and overall inhomogeneous three-dimensional structure, these agglomerates were not taken up into cells successfully. Dark field microscopic inlets in Figure 3.3 show good localization of particles to confined areas and prove intracellular storage of MNPs within endosomal vesicles.

3.2.1.4 Phenotypic Surface Marker Composition of Labeled HSCs

Hematopoietic cells of various developmental stages cannot easily be discriminated from each other using conventional microscopic techniques. To assure that only target populations are being examined, surface marker stainings employing cytometry were performed. Distinct cell types display a specific repertoire of surface antigens that allow a conclusion as to their (i) developmental origin and lineage commitment, (ii) their current maturation state, as well as their (iii) viability state potentially being compromised due to MNP labeling procedures.

To analyze possible phenotypic alterations of labeled HSCs due to MNP incorporation, levels of CD11b, CD11c, CD24 and Flt3 were examined (**Figure 3.4**A). CD11b represents an

integrin present on myeloid committed precursors, monocytes and differentiated innate immune cells[198]. CD11c is a hallmark protein of differentiated DCs and was used as a negative control in cytometric experiments of HSCs[91]. CD24, a glycosyl-phosphatidylinositol-anchored protein, is expressed on immature cells of most, if not all, major hematopoietic lineages[199]. Flt3 represents a cytokine receptor expressed on the surface of hematopoietic progenitor cells[103]. Representative surface marker expressions are displayed in Figure 3.4A.

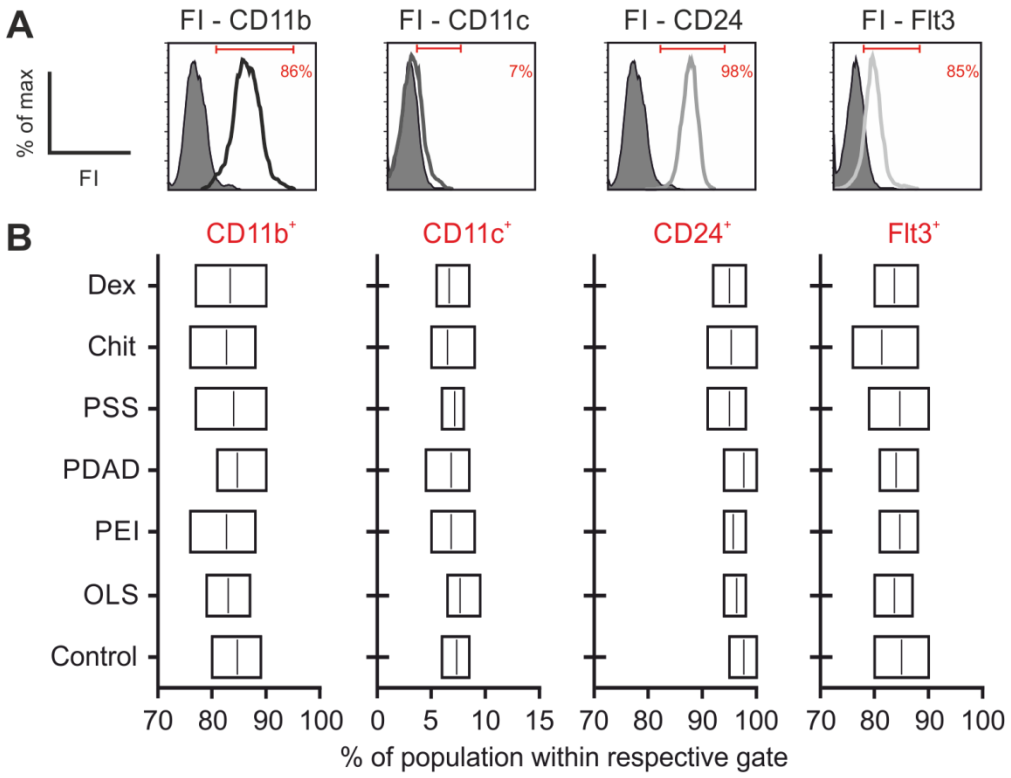

Figure 3.4 Phenotypical FACS analysis of MNP-pulsed HSCs. A) 2-D histograms depicting fluorescence intensity (FI) of surface stainings for CD11b, CD11c, CD24 and Flt3 using bold empty curves. Cells pre-gated on viable cell fractions. Isotype staining controls shown in grey tainted areas. Red areas indicate gating strategy used in numerical analysis depicted in B). Displayed is one representative experiment (n=3). **B)** Numerical evaluation of gates shown in A). Depicted are mean values (vertical lines) ± min/max values (boxed) of three independent experiments.

As expected, expression levels for CD11b and CD24 were found to be very high and provided information about the lineage commitment and the undifferentiated phenotypic state of propagated HSCs, respectively. No alterations regarding status of differentiation were observed after MNP labeling procedures. Faint surface protein levels of CD11c did not exceed 9% of total gated cells, and thus, were considered neglectable. Furthermore, the increase in fluorescence intensity (FI) was considered neglectable, since only a minor intensity shift resulted after staining procedures when compared to isotype background

staining controls. Levels of Flt3 were elevated, undermining the undifferentiated nature of progenitor cell populations even after MNP-pulsing.

As outlined in Figure 3.4B, none of the MNP formulations employed changed the surface marker makeup of the cells significantly when compared to unlabeled control stainings. This proved that successful uptake of particles does not result in change of cellular phenotype as would be the case during differentiation, cellular activation, or even apoptosis.

3.2.1.5 *In Vitro* MRI Studies employing HSCs: Detection Limits

Iron-oxide based MNPs are known to alter T2 and T2* MRI characteristics that enhances imaging of labeled cell populations when compared to their unlabeled counterparts. Reduction of signal intensity through shortening of relaxation times increases image contrast drastically.

To test employed MNP formulations with regard to their potential as MRI contrast agents, *in vitro* phantom studies were performed. Cellular distribution within agarose phantoms proved to be very homogenous and uniform, allowing a quantitative comparison of different MNPs. Since iron oxide particles induce hypo-intense regions due to their potential of generating local magnetic field inhomogeneities, areas of contrast agent accumulation within cells show pronounced signal loss. To compare T2* signal reduction patterns and resulting maximum/minimum detection limits between contrast agents employed, 3D image stacks were mounted and results are displayed in **Figure 3.5**.

All particles employed could be tracked down to a concentration of 10^3 cells. However, Chit-MNP proved to be the least effective contrast agent that was only traceable down to the lowest cell seeding density of 10^4 cells. The maximum seeding density that still provided decent contrast between individual signal reduction areas proved to be 10^5 seeded HSCs in case of OLS and Dex-MNP. Most likely, other MNPs would have required a higher seeding density to achieve similar T2 signal reduction patterns.

In summary, all particles used in this study were effectively imaged within HSCs after cellular incorporation using T2* weighted MR scans. However, especially PEI-MNP proved to be superior when compared to other poly-electrolyte and OLS-MNP imaging agents employed.

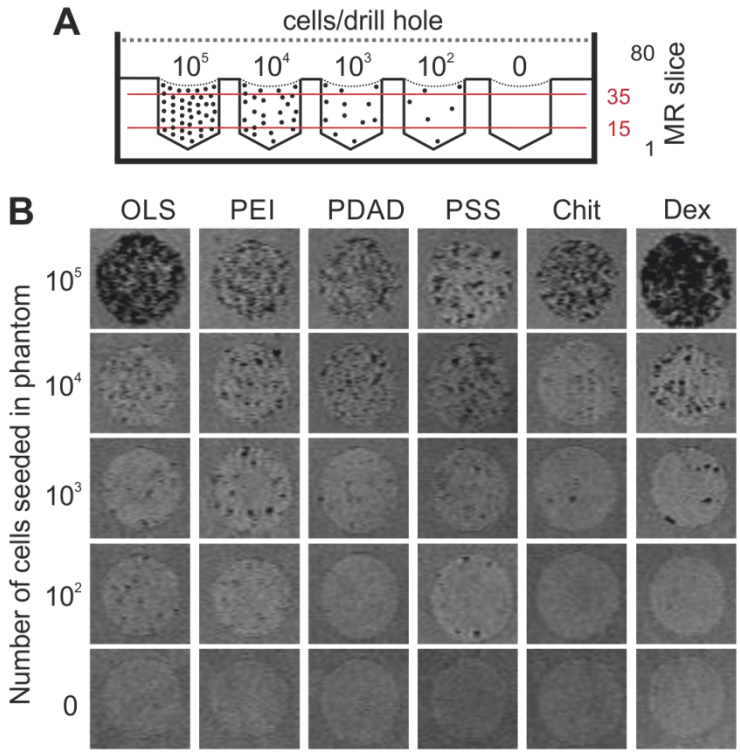

Figure 3.5 ***In vitro*** **MRI phantom studies using MNP-labeled HSCs. A)** Cross-sectional schematic of agarose phantoms harboring labeled HSCs. Scan slices 15-35 (red horizontal lines depict cut-offs) used to mount 3D image stacks depicted in B). Inhomogenous volumes outside of cut-offs were not used in further data processing. **B)** MNP-labeled HSCs were embedded in agarose and T2*-weighted 3D MRI gradient echo scans were performed to evaluate hypo-intense regions of signal-loss due to iron oxide MNPs inside HSCs. Minimum and maximum detection limits were evaluated and corresponding phantom pictures with respective seeding density depicted. Displayed are resulting 3D image stacks of individual scan slices (15-35) merged using ImageJ software .

3.2.1.6 *In Vitro* MRI Studies employing HSCs: Relaxivity

In molecular imaging, relaxivity provides valuable information about the contrast of target structures compared to their unlabeled adjacent environment[200]. To provide numerical data of the respective MNPs using MRI, map scans were performed and resulting T2* signal reduction patterns were plotted against pre-defined but varying echo times.

As outlined in **Figure 3.6**, signal intensities of aqueous MNP solutions (Figure 3.6A) (iron conc. 10 µg/ml) were substantially lower when compared to values obtained after incorporation of MNPs into viable HSCs (Figure 3.6B). In particular, PSS and OLS-MNP

represented strong contrast agents inside HSCs due to their capacity to decrease T2* signal intensity at very low echo times (5-15 ms) when compared to control levels. Since surrounding tissues do not provide such a strong negative impact on MRI signal, contrast can be expected to be enhanced markedly. On the other hand, the polysaccharide-coated MNPs

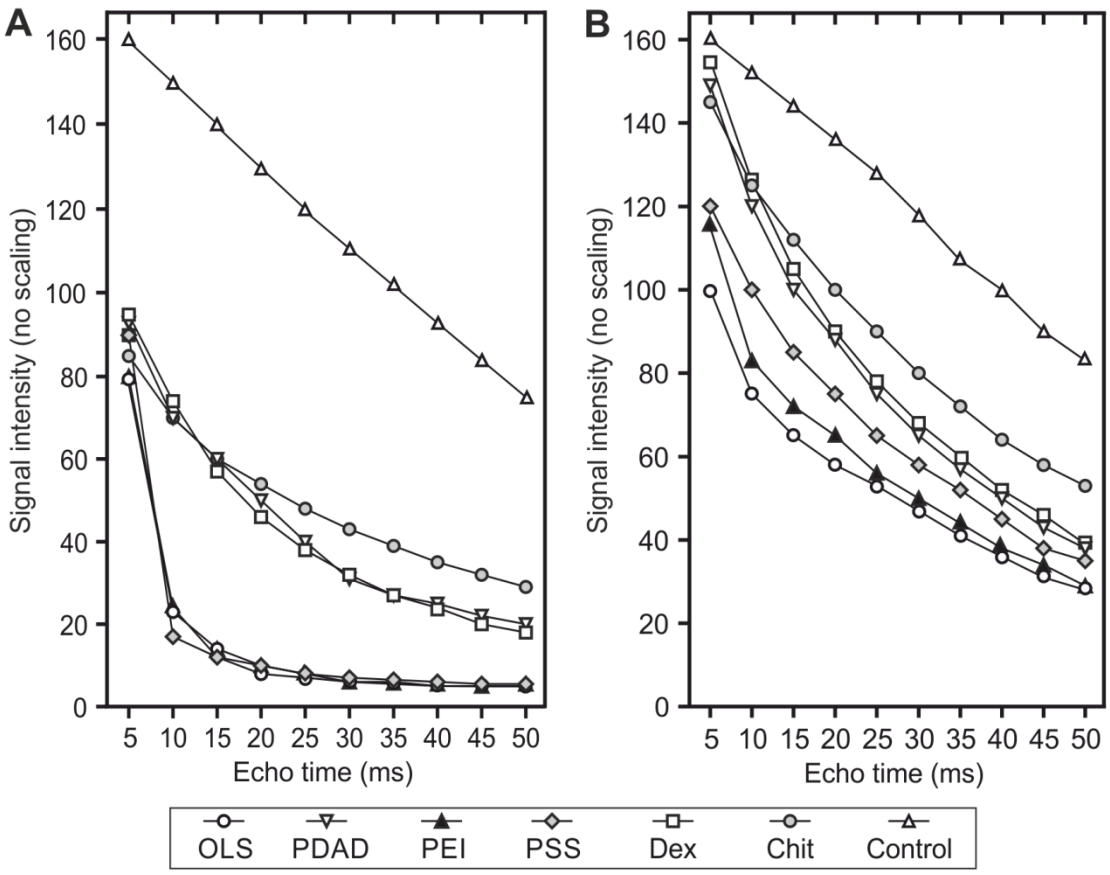

Figure 3.6 Numerical evaluation of *in vitro* MRI phantom studies using MNP-labeled HSCs. Map scans were performed by consecutively increasing echo times (5 ms increments) and recording remaining signal intensities. **A)** T2* relaxation kinetics of aqueous MNP solutions alone. MNP solutions equilibrated to final concentration of 10 µg/ml prior to seeding into phantoms. **B)** Depiction of map scan kinetics after cellular uptake of poly-electrolyte MNPs by HSCs. Initial labeling concentration of cells: 10 µg/ml. Magnetic separation was employed prior to agarose immobilization of cells to exclude unlabeled cell fractions. Displayed are respective signal intensities at various echo times pre-defined during map scan protocol design. Residual signal mitigations observed as a result of hypo-intense regions within agarose phantoms due to local iron incorporation. Shown is one representative experiment out of three.

and PDAD-MNP did not appear to lower signal intensity to such a high degree, making them less efficient at imaging lower numbers of HSCs. In summary, however, all of the employed MNPs proved to be suitable intracellular HSC contrast agents in MR imaging.

After fitting raw map scan data to numerical values, T2 relaxation times of each individual MNP were obtained. **Table 3.3** provides information about the capacity of synthesized nanoparticles to serve as MRI contrast agents. Individual data points of curves shown in Figure 3.6 were fitted using both ParaVision and ImageJ software to allow the calculation of

T2 relaxation times under the given experimental conditions. As previously demonstrated, PSS and OLS-MNP showed T2* relaxation times below 40 ms, and thus, represent the most

MNP	T2* relaxation time (ms)	
	MNP solution	MNP within HSCs
PEI-MNP	14 (± 3)	46 (± 17)
PDAD-MNP	18 (± 5)	55 (± 13)
PSS-MNP	10 (± 3)	30 (± 9)
Chit-MNP	40 (± 13)	74 (± 23)
Dex-MNP	20 (± 5)	58 (± 11)
OLS-MNP	14 (± 3)	37 (± 7)

Table 3.3 Relaxation properties of MNPs. Depicted are extracted numerical T2* values as fitted by software algorithm as a result of map scan protocols (see Fig. 3.6). Shown are aqueous MNP suspensions alone (center column) and after magnetic separation of labeled HSCs (right column) by employing a T2* weighted MRI map scan. Values fitted and calculated using Bruker ParaVision software. Averaged numbers represent mean values of three independent experiments ± SD.

efficient contrast agents for tracking HSC in this study. On the other hand, Chit-MNP provided high T2* relaxation times in both aqueous solution and within target cells, making it less efficient at detecting embedded target cells.

3.2.2 Inflammatory Dendritic Cells (iDCs)

Propagated myeloid committed precursors can be differentiated into inflammatory DC-like cells of the myeloid lineage using GM-CSF[101]. Under continuous administration of GM-CSF growth factor, cells undergo consecutive differentiation steps until acquiring an immature DC phenotype. In particular, inflammatory DCs are believed to arise as a consequence of circulating monocyte stimulation and subsequent differentiation similar to macrophages[41]. Due to the prior amplification of myeloid committed progenitor cells, iDCs, macrophages and granulocytes all arise throughout the remainder of the culture. Since DCs represent the bridge between innate and adaptive immunity due to their pivotal role in the induction of adaptive immune responses, they were included in this study to investigate the immunological consequences of MNPs employed. DCs represent highly phagocytic cells in their immature state prior to their activation, making them a particularly attractive target cell type to investigate MNP uptake and imaging properties in both research and clinical applications[13].

3.2.2.1 Biocompatibility Studies

Biocompatibility studies utilizing immature inflammatory DCs were performed using both MTT colorimetric assays as well as cytometry employing 7-aminoactinomycin (7-AAD). MTT assays only allowed the analysis of bulk cultures that were stimulated with respective MNP formulations for 24 h, whereas 7-AAD staining permitted a cytotoxic screening of magnetically pre-selected as well as cytometrically gated iDC populations. 7-AAD resembles an organic peptide that intercalates into DNA of dead or dying cells after crossing the disrupted cellular membrane[201]. Using flow cytometry, it is possible to detect the 7-AAD fluorescence signal inside individual cells that allows a monitoring of dye incorporation.

As outlined in **Figure 3.7**A, all MNPs provided superior biocompatibility even when subjected to high contrast agent concentrations (200 µg/ml). As previously discussed, Chit-MNP showed slightly elevated levels of cytotoxicity when compared to other MNP formulations employed. Figure 3.7B graphically illustrates the gating strategy of data presented in Figure 3.7C.

Biocompatibility in general is decreased after increasing MNP labeling concentration and results obtained further substantiate data gathered in Figure 3.7A. OLS-MNP and PDAD-MNP represented the most biocompatible MNP formulations with only about 15% of iDCs displaying adverse cellular effects at the highest labeling concentration of 200 µg/ml. Within commonly used labeling concentration ranges used in literature[202], however, all particles proved to be highly biocompatible.

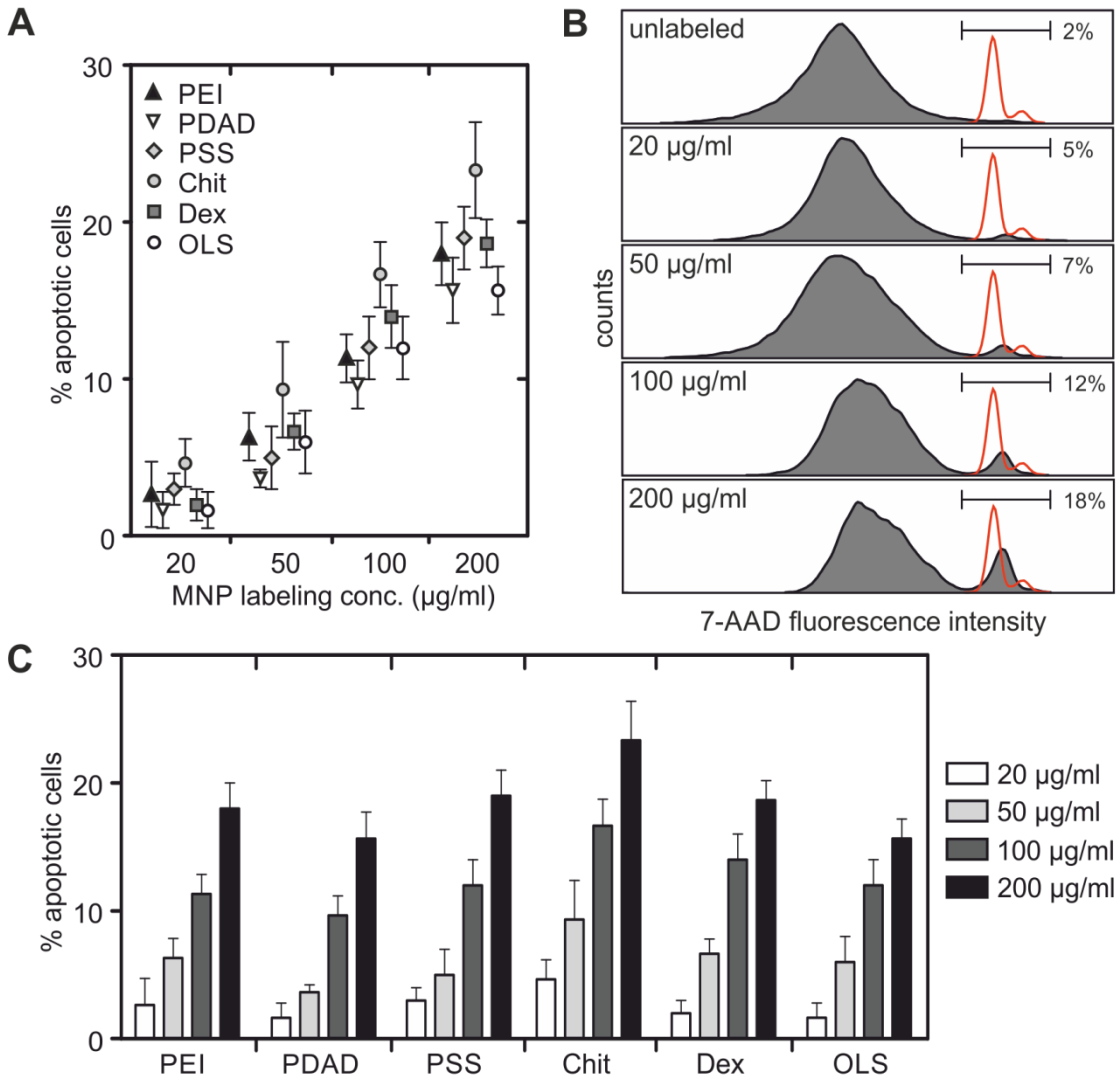

Figure 3.7 Cytotoxic effects of various poly-electrolyte MNP concentrations on inflammatory DCs (iDCs). A) MTT-based colorimetric assay displaying cytotoxic effects of increasing MNP labeling concentrations on bulk cultures. Cells were incubated with respective MNP formulations for 24 h using increasing iron concentrations of 20-200 µg/ml as displayed. **B)** Intracellular 7-AAD stainings employing flow cytometry. This reagant intercalates into the DNA of dying cells only, thus allowing a quantitative measurement of apoptotic cell fractions. Displayed is one representative experiment using OLS-MNP and underlying gating strategy employed. **C)** Fraction of cells within gate outlined in B). Unlike the MTT assay in A), 7-ADD tests were performed employing magnetically separated cells. Displayed are mean values obtained from three independent experiments ± SD.

3.2.2.2 Uptake and Intracellular Iron Concentration

Magnetic separation techniques were utilized to part the unlabeled cell fraction from their labeled counterparts. This allowed a qualitative estimation of the degree of uptake as well as a quantification of iron deposition.

In contrast to HSCs, iDCs readily take up all MNP formulations to a high degree (**Figure 3.8**A). Chit-MNP resembled the only exception, as it was only successfully integrated by 40%

of total cells. Charged MNPs and OLS-MNP were taken up to the highest extent, with more than 75% of total iDCs being labeled after 24 h of incubation.

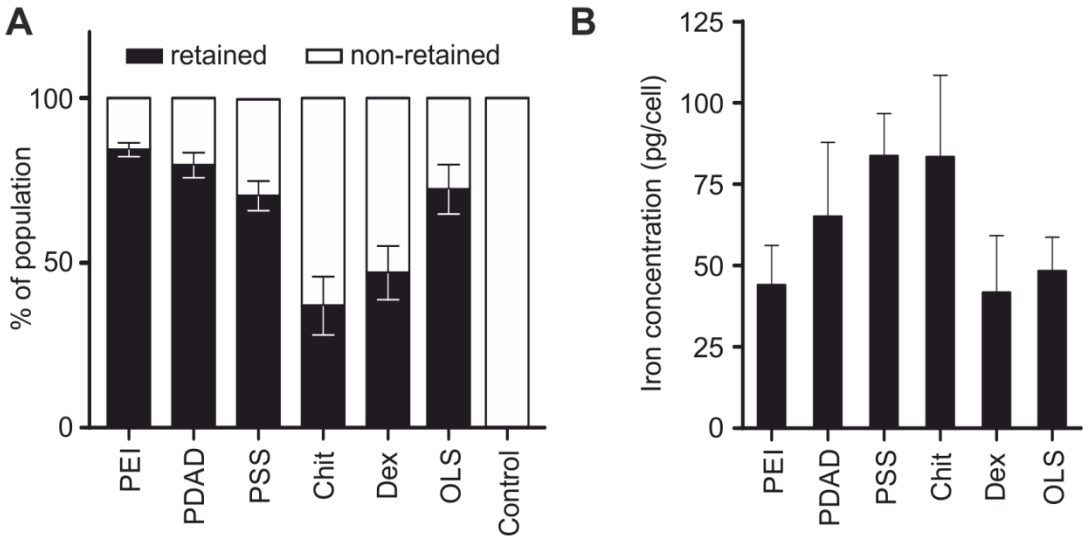

Figure 3.8 Uptake properties of MNPs into iDCs. **A)** Magnetic separation data of respective MNP formulations after 24 h of incubation using immature GM-CSF derived inflammatory DCs. Displayed are mean values ± SD (n=3). **B)** FerroZine iron assay to determine intracellular iron load within DCs. Numbers correspond to average iron concentration in pg/cell. Lower detection limit proved to be 5 pg/cell. Displayed are mean values of three independent experiments ± SD.

Magnetically separated iDCs were subjected to FerroZine iron assay to determine intracellular iron load. As shown in Figure 3.8B, labeled iDCs acquired a high amount of iron on average per cell. Charged poly-electrolyte particles were taken up to a very high extent, ranging from 45-80 pg/cell. Although in the case of OLS-MNP only 48 pg/cell of iron was acquired by cells, in summary all particles employed displayed good uptake characteristics in DCs.

3.2.2.3 Histological Staining of MNP-Labeled iDCs

To visualize intracellular localization and possible clustering of MNPs employed, histological iron staining of cytospins were performed. In this staining procedure, the synthetic compound Prussian blue is used to detect the presence of iron in biological specimens.

As shown in **Figure 3.9**, all iron residues originating from iron deposits within endosomal structures could be visualized. It is worth noting that all MNPs were localized confined to the cytoplasm. No staining patterns were observed within the nucleus or loosely attached to the outer membrane, providing initial evidence as to complete uptake processes. However, Chit-MNP displayed clustering of particles, as staining pattern obtained differ from ones seen with

other MNP formulations. Furthermore, the magnitude of iron staining pattern were decreased in the case of PEI-MNP compared to other particles tested.

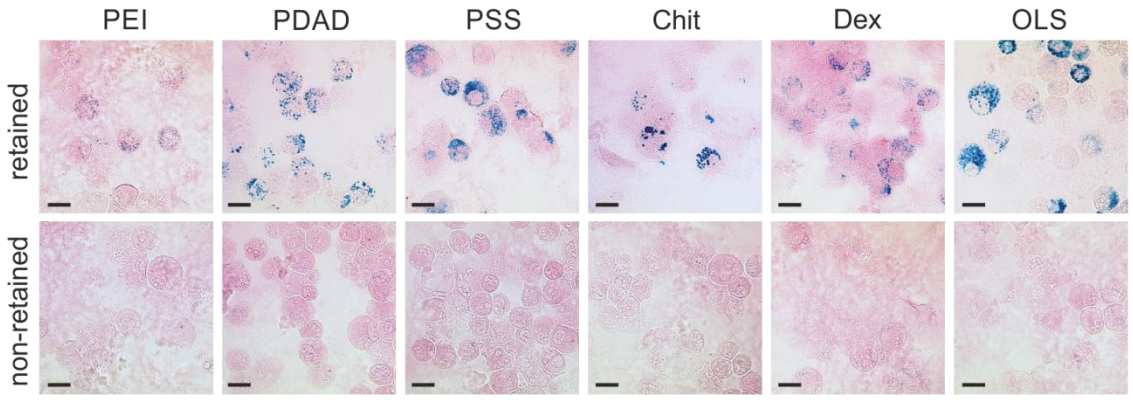

Figure 3.9 Histological stainings of cytospins after magnetic separation. Top row displays retained or MNP-labeled iDCs after magnetic separation, lower panels depict unlabeled counterparts. Blue areas correspond to localized iron deposition within cells due to Prussian blue staining. Membraneous structures counter-stained using Neutral Red (pink areas). Scale bars 15 µm.

Overall, particles were successfully imaged using Prussian blue histological staining of fixed cytospins. Areas of intense staining patterns appeared to be confined to the cytosol, most likely within endosomal vesicles.

3.2.2.4 Transmission Electron Microscopy (TEM) and Endosomal Packaging

To further substantiate findings related to intracellular fate and packaging properties of MNPs, transmission electron microscopy (TEM) analyses were performed. TEM provides information about the electron density of a given biological specimen that relies on the electron beam stopping power of imaged structures.

Figure 3.10A displays low-resolution pictures of inflammatory DCs labeled with respective particles. MNP depositions are marked with white arrows to improve visualization. As can be observed, clustering patterns varied with respect to the different surface chemistries of the nanoparticle at hand. Magnified images of specific endosomal structures containing iron oxide residues substantiate this observation even further.

As seen in Figure 3.10B, PEI, PSS, Dex and Chit-MNP tended to be packaged more loosely when compared to PDAD and OLS-MNP. To further investigate this finding, regions of interest (ROIs) marked in white were normalized against surrounding background and greyscale values were deduced. Figure 3.10C shows numerical evaluation of electron density as derived from greyscale values. Strikingly, PDAD and OLS-MNPs showed a significantly

higher electron density than other MNP formulations employed. As can be visually confirmed from Figure 3.10B, PEI-MNP, PSS-MNP, Chit-MNP, and Dex-MNP displayed lower normalized electron densities in numerical evaluation of greyscale values (Figure 3.10C).

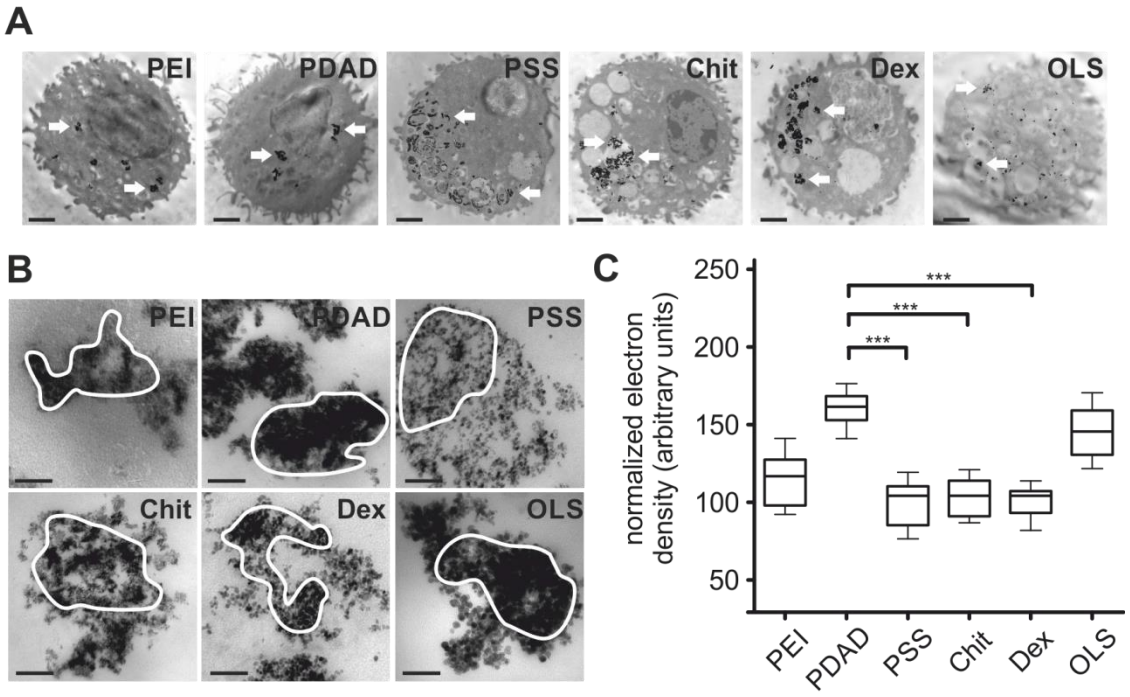

Figure 3.10 Transmission electron microscopy (TEM) studies of MNP-labeled inflammatory DCs. **A)** Endosomal structures containing clusters of MNPs as highlighted by white arrows. Scale bars 3 µm. **B)** Magnified images of individual endosomal compartments containing MNP clusters. White circles encompassing regions of interest (ROIs) used to evaluate electron stopping power from grey-scale values as illustrated in **C)**. Displayed are mean values (horizontal bars) ± min/max values (boxed). Whiskers depict SD from 30 independently evaluated ROIs. Scale bars 50 nm.

In summary, TEM measurements provided valuable information as to the intracellular localization and fate of engulfed particle formulations within iDCs. Furthermore, high-resolution images of specimen slices allowed the deduction of particle packaging properties and density on the basis of their electron attenuation.

3.2.2.5 Phenotypic Surface Marker Composition

DC subsets are known for their abundance of surface markers related to both innate and adaptive immunity[100]. These proteins indicate the real-time maturation status of individual cells and therefore allow a monitoring of potential changes after a given stimulus. To test whether or not MNPs induce immunological consequences within these cells, flow cytometric analyses were employed.

CD11c and MHC II both represent proteins expressed on the surface of professional antigen-presenting cells such as iDCs. Even though CD11c levels remain constant after terminal differentiation, MHC II levels are subject to change depending on the maturation state of the cell[203]. Upon activation via a foreign stimulus, elevated levels of MHC II are being recorded. In conjunction with CD80 and CD86, both members of the B7 co-stimulatory molecule family, conclusions on the activation state of iDCs can be drawn[204]. Whereas immune cells only express low levels of these two surface proteins critically involved in the functional stimulation of naïve T-lymphocytes in secondary lymphoid organs, activated APCs rapidly increase their abundance.

As shown in the top row of **Figure 3.11** (unlabeled control, black histogram), surface expression levels of MHC II, CD80 and CD86 proved to be fairly low in unstimulated iDCs. In contrast, these values were vastly up-regulated (red histogram) upon cellular activation using LPS.

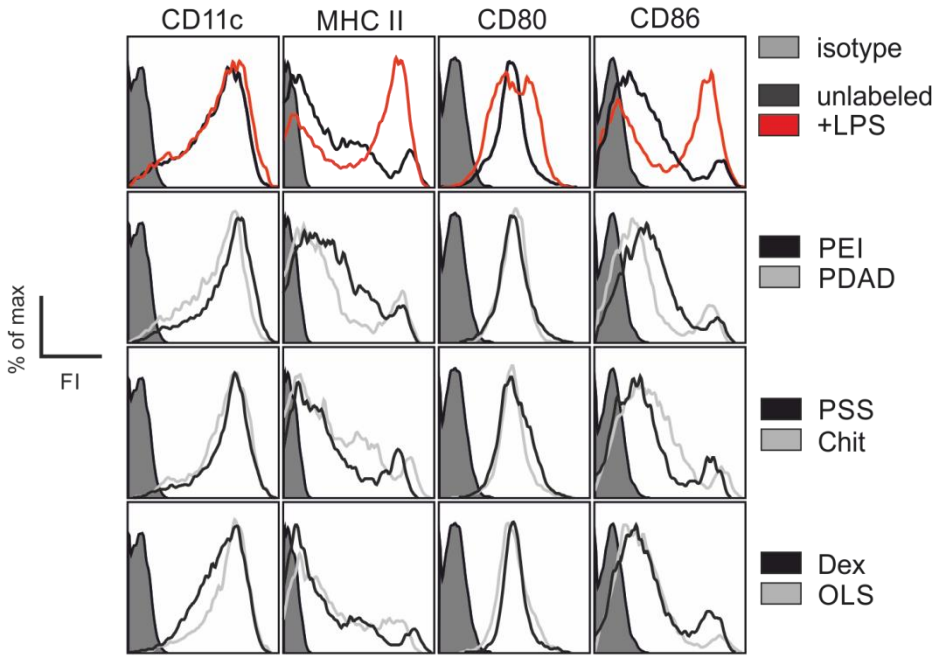

Figure 3.11 Phenotypical surface marker profiling of labeled GM-CSF derived iDCs. Quantitative abundance of CD11c, MHC II, CD80 and CD86 surface molecules and their potential up-regulation after MNP stimulation. LPS used as positive control (red histograms). Unstimulated control DCs depicted by black histograms in top row displaying cellular phenotype at the time of labeling. Cells were stimulated with LPS or respective MNP formulations for 24 h, magnetically separated and washed prior to experimental cytometry analyses. Depicted are fluorescence intensities (FI) of one representative experiment (n=3).

However, unlike LPS stimulation, none of the employed MNPs caused up-regulation of surface proteins relevant for activation and antigen presentation. Therefore, MNP formulations are biologically inert and do not trigger potential immunological consequences

within iDCs. Surface marker profiles remain subject to minor variations based on the *in vitro* culturing conditions. However, fluctuations remained within acceptable ranges.

Samples shown in Figure 3.11 were magnetically pre-selected, denoting that target cells did successfully acquire MNPs prior to cytometric analysis. On the other hand, unlabeled counterpart fractions did also not show up-regulation of MHC II, CD80 and CD86, however, they displayed a more mature phenotype (data not shown). This finding is in agreement with current knowledge on DC biology implying that only immature iDCs retain the capability of enhanced phagocytosis[205].

3.2.2.6 *In Vitro* Migration Assay

Cellular activation triggers DCs to up-regulate the expression of migration-dependent genes[204]. Using iDCs, an *in vitro* migration assay was employed to investigate the potential of MNP-stimulated DCs to acquire a migratory phenotype. After being activated through the uptake and processing of an external antigen, DCs migrate towards draining lymph nodes in order to present the acquired antigenic information to naïve T cells, and thus, initiate an appropriate adaptive immune response[104].

MyD88$^{-/-}$ knockout iDCs were included in the study to test whether MNPs possibly signal through TLR4 in a MyD88 adaptor protein dependent manner. As outlined in **Figure 3.12**, poly-electrolyte and OLS-MNPs did not show a significant up-regulation of their migratory behavior when compared to untreated controls. In addition, no significant difference between cell numbers of Wt and MyD88 knockout cells were observed, proving the lack of TLR involvement with respect to the nanoparticles tested.

However, LPS is known to signal exclusively through the TLR4 receptor, and therefore, MyD88$^{-/-}$ knockout iDCs served as control of cell functionality. As shown in Figure 3.12, numbers of migratory LPS-treated cells significantly dropped in case of cells devoid of the adaptor protein MyD88 relevant for TLR signaling and subsequent NFκB gene activation.

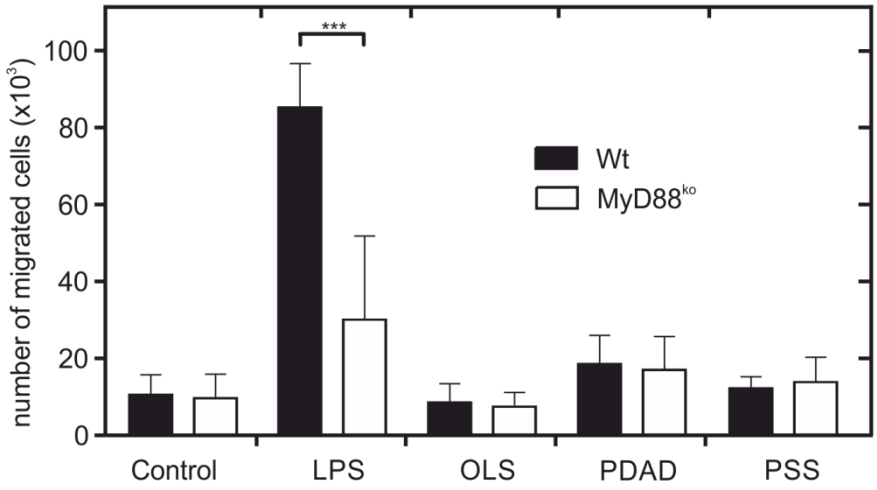

Figure 3.12 *In vitro* migration assay in the context of MyD88 adaptor protein knockout mice. Inflammatory DCs were labeled with MNPs and subsequently seeded into Transwell migration plates, allowing directional migration through a permeable membrane towards ELC chemo-attractant. Number of trans-migrated cells serve as an indication of fully activated DC phenotype. To investigate possible TLR receptor involvement, both Wt and MyD88^{ko} cells were employed. All values displayed in response to ELC chemokine gradient normalized against undirected migration of unstimulated iDCs in the absence of chemotactic signals. Results displayed are mean values ± SD (n=2).

3.2.2.7 *In Vitro* MRI Studies and Relaxivity

To further investigate MRI properties of MNP formulations employed in iDCs, MRI relaxometry studies were performed. Image contrast represents an important asset of MR imaging that enhances both imaging quality and differentiability[206]. In particular, contrast-to-noise ratio allows a quantifiable rating of contrast agent performance according to their capability to induce local field inhomogeneities.

As outlined in **Figure 3.13**, T2 map scans revealed good signal reduction patterns of MNPs. Figure 3.13A depicts pseudo-color images of labeled iDCs within *in vitro* phantom drillings. As outlined by the color legend, all particles except Chit-MNP and PSS-MNP showed low T2 relaxation times for all seeding densities examined. However, especially Chit-MNP and PSS-MNP proved to be inferior when compared to contrast agent characteristics of other employed poly-electrolyte and lipid-shell MNPs.

Figure 3.13B depicts the degree of linearity of R2 relaxation rates with regard to seeding density. Only Chit-MNP and PSS-MNP proved to be less efficient when compared to the remaining MNP formulations employed, resulting in a marked drop of R2 at lower seeding densities. Therefore, the linear relationship between R2 and seeding density was compromised below 10^3 cells seeded.

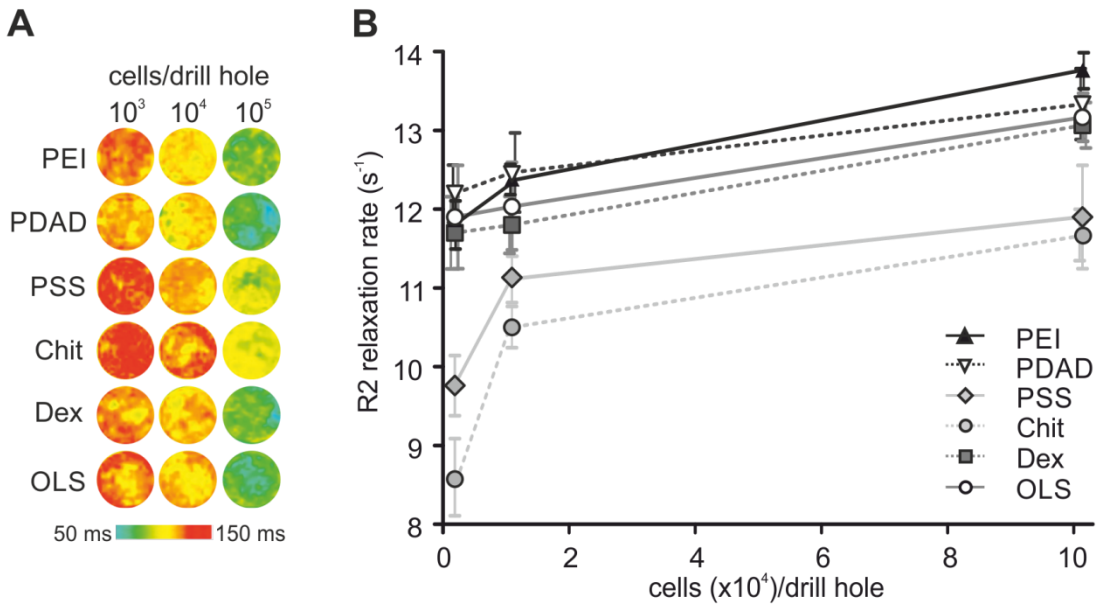

Figure 3.13 Relaxometry data of *in vitro* phantom studies. A) Pseudo-color depiction of software-calculated average relaxation times with regard to seeded density. Depicted color representation shows color coding corresponding to numerical values of relaxation times calculated using ImageJ. Prior to analysis, iDCs were immobilized into agarose and MR scans were performed under controlled experimental conditions. **B)** R2 relaxation rate as calculated from map scan raw data using Bruker ParaVision software. Depicted are mean values ± SD (n=3).

In summary, relaxivity data of all MNPs showed linear relationship between seeding density and resulting R2 relaxation rates within a wide range of seeding densities, providing good MR capabilities of employed MNPs within labeled iDCs.

3.2.2.8 *In vitro* MRI Detection Limits and CNR Values

To further investigate minimum and maximum possible detection limits within agarose phantoms, T2* image stacks were mounted. These values provide information about the contrast agent potential of employed MNPs even when imaging low numbers of target cells within a given area. Contrast to noise ratio is a measure to determine image quality of regions of interest (ROIs) in comparison to background "noise". A high CNR ratio translates into good visualization and differentiability of structures, and thus, denotes excellent MR contrast agent properties.

Figure 3.14A displays a cross-sectional view of an imaged agarose phantom and signal loss patterns observed to deduce minimum and maximum cut-off section numbers to be used in further analyses. OLS-MNP and PDAD-MNP displayed superior image contrast and cells could be successfully imaged down to a seeding density of only 10^2 cells (Figure 3.14B+C) with relatively high CNR remaining. On the other hand, Chit-MNP CNR ratios declined

rapidly, even falling below background levels in case of low numbers of embedded target cells. Using this particular MNP, it was only possible to successfully image 10^4 embedded cells.

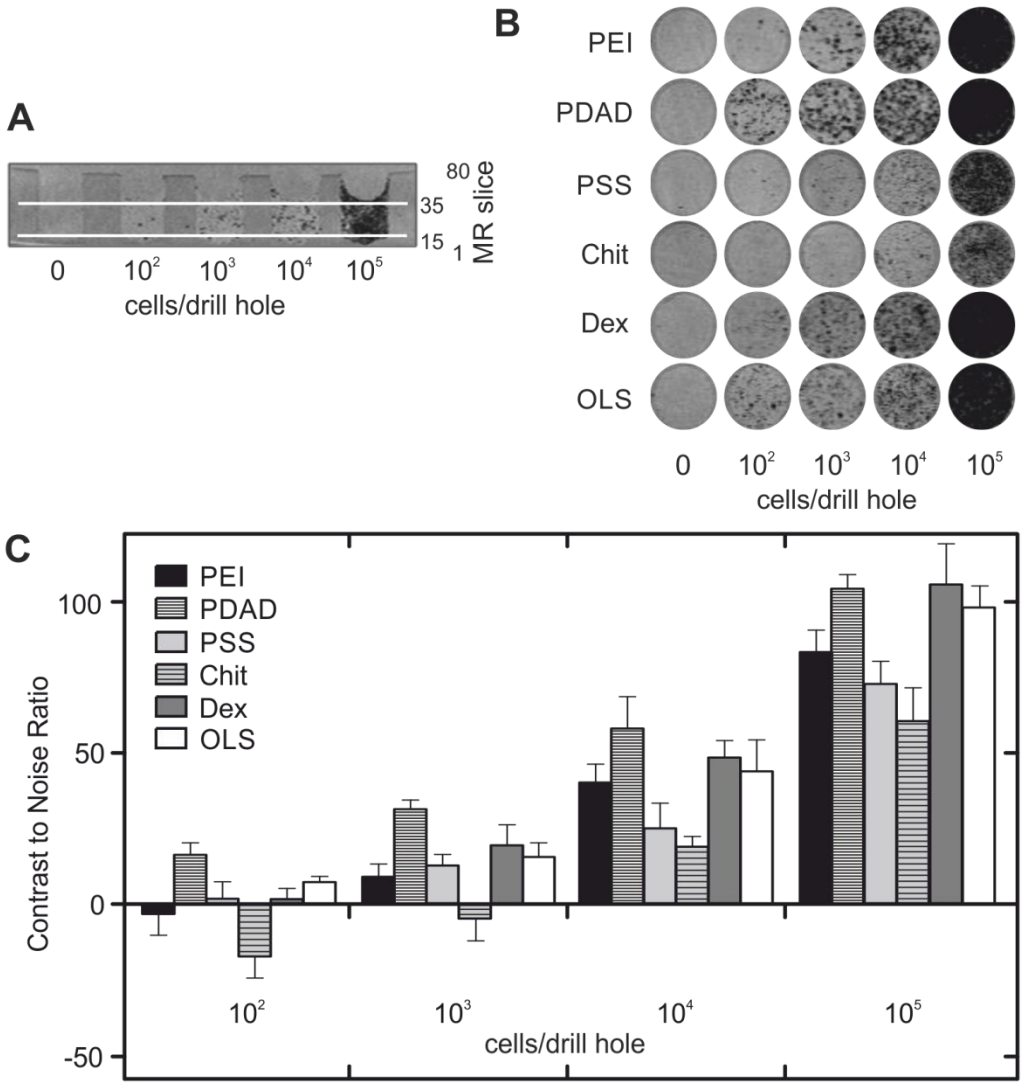

Figure 3.14 ***In vitro*** **MRI detection limits and SNR ratios. A)** Example of a cross-sectional view through an agarose phantom of OLS-MNP labeled iDCs. Numbers depicted correspond to MRI scan slices. Scan slices 15-35 were merged to yield images shown in B). **B)** Stacked 3D images of signal reduction due to the presence of contrast agent, providing minimum and maximum detection limit data. **C)** Numerical calculation of signal to noise ratios on the basis of grey-scales of mounted image stacks outlined in B). Shown are mean values ± SD of three independent experiments.

Contrast to noise ratio remained within good performance levels for all MNPs down to 10^3 embedded cells with Chit-MNP being the only exception.

In conclusion, all synthetic MNPs are suitable contrast agents to visualize iDCs, however, PDAD and OLS-MNP displayed superior imaging characteristics and proved to be most suited for imaging low numbers of iDCs within a given target volume.

3.2.3 MNP stimulated Flt3L-Generated DC Subsets

Flt3, a tyrosine kinase known to be crucially involved in lymphocyte development, stimulates differentiation towards the lymphoid lineage of blood cells, such as B-, T cells and DCs. This observation has led to the development of defined experimental procedures to differentiate bone marrow cells into various subsets of DCs.

In this study, Flt3 ligand (Flt3L) was used to induce differentiation of murine bone marrow progenitors to yield both conventional (cDCs) as well as plasmacytoid dendritic cells (pDCs). Both cell types have important functions in steady-state and inflammation, and therefore were used as targets for MNP stimulation.

3.2.3.1 MNP Stimulation of Flt3L Generated cDCs in the Context of Knockouts

Since Flt3L induces the differentiation into both cDCs and pDCs to roughly equal amounts, it is crucial to exclude unwanted cell populations to obtain adequate experimental results. As illustrated in **Figure 3.15**, cDCs express high levels of both CD11b and CD11c. Due to this

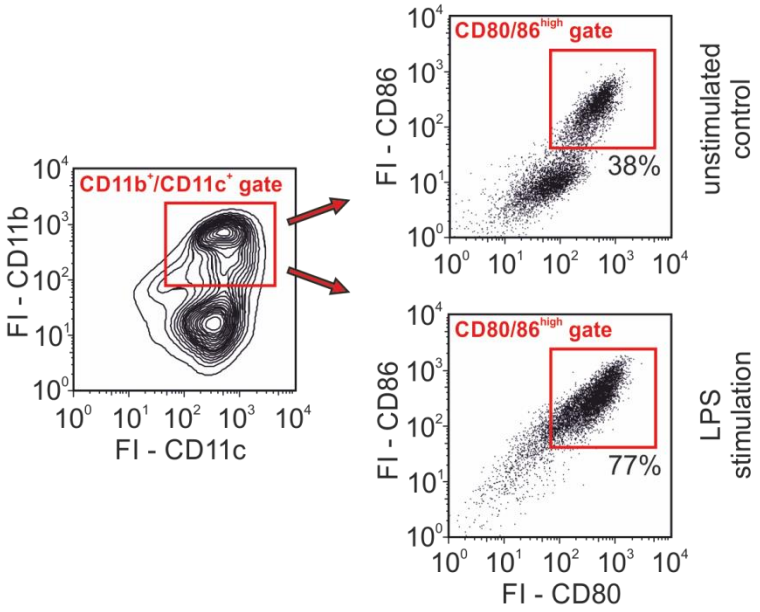

Figure 3.15 FACS gating strategy of Flt3L generated conventional DCs (cDCs). Target cell gating strategy of cDCs using $CD11b^+$ $CD11c^+$ populations for further surface marker evaluation (left image). Illustration of $CD80/86^{high}$ co-stimulatory molecule gating strategy and example evaluation of unstimulated and LPS-treated controls depicted in right column (red boxes). Percentages of cells within $CD80/86^{high}$ gate used for numerical evaluation.

myeloid commitment and apparent DC phenotype, a $CD11b^+CD11c^+$ double-positive gate was used to exclude pDCs from further experimental analyses. As outlined in Figure 3.15,

cDC gates were selected to further analyze surface expression levels of both CD80 and CD86 co-stimulatory molecules. The area of interest included cell fractions that were both $CD80^{high}$ as well as $CD86^{high}$. Approximately 38% of total gated cells were positive in case of unstimulated controls, whereas LPS stimulation significantly increased this fraction up to 77%.

To further investigate possible uptake and signaling mechanisms of Flt3-generated cDC populations, TLR4 and TLR9 knockout cells were employed. These toll-like receptors are critically involved in the recognition of foreign structures of both bacterial and viral origin, and lead to the induction of primary immune responses[92]. As previously discussed, MyD88 represents a signaling molecule downstream of the initial receptor-ligand recognition that is involved in translating the acquired surface information through signaling cascades of both receptors into nuclear expression of i.e. NFκB target genes[204]. The ASC protein is involved in the inflammasome pathway that recognizes both PAMPs and DAMPs through the cleavage of pro-caspase 1[207].

Figure 3.16 depicts the numerical evaluation of $CD80^{high}CD86^{high}$ gates as shown in Figure 3.15. As previously reported in similar experiments, poly-electrolyte MNPs did not trigger

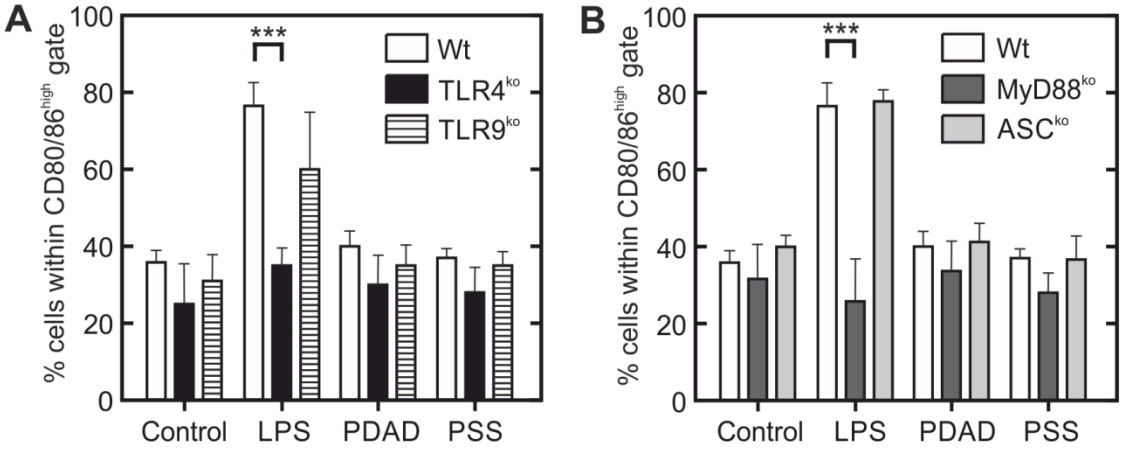

Figure 3.16 FACS profiling of Flt3L generated cDCs in the context of TLR receptor knockout mice. Displayed are surface marker levels of cDCs treated with poly-electrolyte MNPs for 24 h. Respective gating strategy shown in Figure 3.15. **A)** Percentage of cDC populations within $CD80/86^{high}$ gate of Wt, TLR4 and TLR9 receptor knockout cells. **B)** Displayed are populations within pre-defined gate in the context of adaptor protein knockout cells (MyD88 and ASC). Data shown are mean values from two different experiments ± SD.

significant up-regulation of assessed surface marker levels in Wt as well as $TLR4^{ko}$, $TLR9^{ko}$, $MyD88^{ko}$, and ASC^{ko} cells. Levels of surface expression are subject to small variations but remained within expected fluctuation levels. Cellular maturation due to LPS treatment resulted in the up-regulation of relevant surface levels as well as proving cellular integrity.

Due to the involved recognition and signaling dependencies of LPS, cellular responses of cDCs was compromised in TLR4^{ko} and MyD88^{ko}.

In summary, both positively charged PDAD-MNPs and particles possessing negative surface functionalization (PSS-MNP) did not alter levels of co-stimulatory molecules present on Flt3L generated cDC populations. Cytometry data suggests biological inertness of MNP formulations unlike stimulation using LPS that triggered a pronounced up-regulation of maturation dependent surface markers, and thus, led to the activation of cDCs.

3.2.3.2 MNP Stimulation of Flt3L Generated pDCs in the Context of Knockouts

In addition to generating cDCs, driving bone marrow derived progenitor cells into

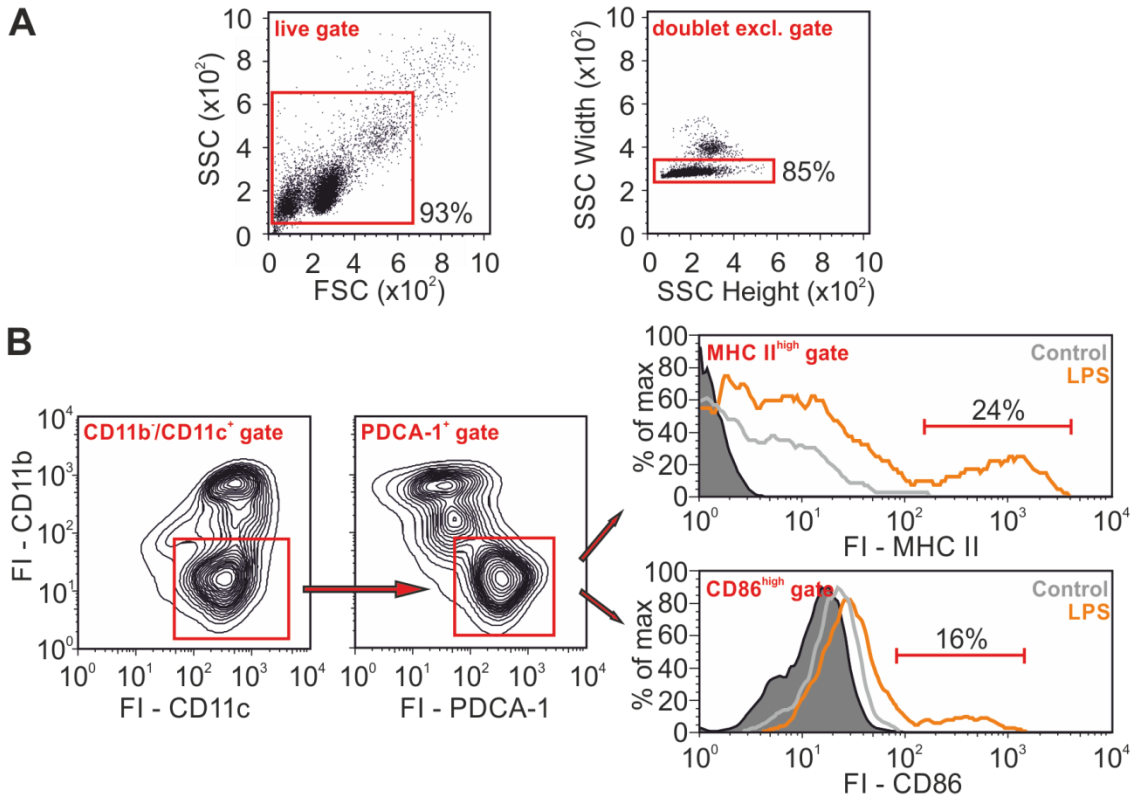

Figure 3.17 FACS gating strategy of Flt3L generated plasmacytoid DCs (pDCs). A) Experimental optimization procedure of differentiated hematopoietic cells to yield live cells, excluding debris, dead cells and doublet measuring errors. **B)** FACS gating strategy to differentiate between pDC and other cell populations in culture with the aid of pDC-specific surface marker gating. CD11b$^-$ CD11c$^+$ B220$^+$ PDCA-1$^+$ cell populations were used for further data evaluation. Right panel displays gating strategy of functionally important markers showing unstimulated (grey histogram) and LPS-treated (orange histogram) controls. Isotype staining controls depicted using tainted grey histograms. Numerical fractions are highlighted to exemplify data evaluation.

differentiation using Flt3L generates pDCs[161]. These cells induce vast amount of IFNs upon

cellular maturation and are critically involved in fighting viral infections, especially in a TLR9 dependent manner[208].

Figure 3.17 graphically illustrates the gating strategy of Flt3L generated pDCs. Cells were pre-selected for further experimental procedures including $CD11c^{+}CD11b^{-}PDCA\text{-}1^{+}B220^{+}$ fractions of total live cells as depicted in Figure 3.18. Levels of surface staining for MHC II and CD86 were evaluated and used for data acquisition and subsequent evaluation. Unstimulated control levels for both MHC II and CD86 gates were undetectable within selected gates. However, numerical values increased to 24% and 16% after cellular activation using LPS, respectively (Figure 3.17B, right column).

Numerical data of MHC II^{high} and $CD86^{high}$ gates are outlined in **Figure 3.18**. Even though pDCs did not yield surface marker abundance levels recorded for cDCs after LPS stimulation, a significant increase in surface marker levels was noted. Due to the fact that LPS is recognized by TLR4, surface marker expression dropped down significantly in case of TLR4 knockout cells.

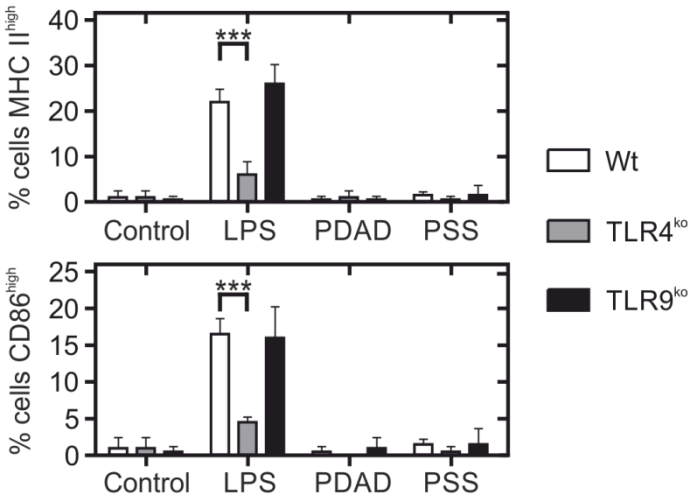

Figure 3.18 FACS profiling of Flt3L generated pDCs in the context of receptor knockout models. Stimulation of pDCs using poly-electrolyte MNPs and subsequent phenotypical analysis. Numerical evaluation of data as exemplified in Figure 3.17 for all MNPs employed in the context of TLR4 and TLR9 receptor knockout cells. Shown are mean values of cell populations within respective gates ± SD (n=2) for both $CD86^{high}$ and MHC II^{high} regions.

However, both PDAD- and PSS-MNPs did not alter surface expression levels of neither CD86 nor MHC II beyond the control baseline significantly. Furthermore, employed TLR4 and TLR9 knockout cells did not result in experimental differences regarding cytometric readouts, undermining the lack of PRR involvement in the recognition of poly-electrolyte MNPs employed in this study.

In summary, poly-electrolyte MNPs proved to be biologically inert and did not lead to an up-regulation of maturation-dependent surface proteins in pDCs.

3.2.3.3 ELISA Data of Bulk Supernatants after LbL-MNP Stimulation

Immune cells release pro-inflammatory cytokines into their immediate surroundings after cellular activation events through NFκB signaling and enhanced protein expression. The repertoire of cytokines ultimately released strictly depends upon the nature of the initial stimulus. To further investigate cytokine release of DCs into their surroundings, ELISA experiments were performed. Detection of pro-inflammatory cytokines was used to undermine data acquired during cytometric experiments as well as providing evidence as to the type of cellular activation.

Bulk cultures of Flt3L generated DCs were stimulated with poly-electrolyte MNPs for 24 h and supernatants were assessed as to their cytokine content. As depicted in **Figure 3.19**,

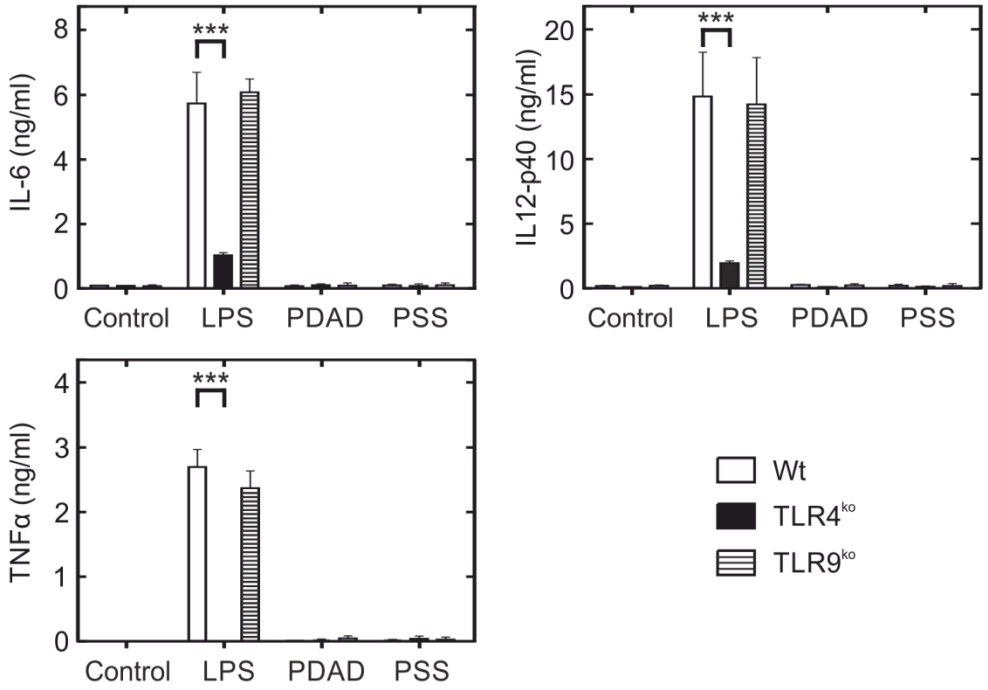

Figure 3.19 Cytokine secretion of poly-electrolyte MNP-stimulated bulk DCs generated using Flt3L. Cell culture supernatants of stimulated DCs used in ELISA assays in the context of TLR4 and TLR9 receptor knockout mice. Pro-inflammatory cytokines IL-6, IL12-p40, and TNFα analyzed to investigate activating potential of MNP formulations within target cell populations. Bars represent mean values of two independent experiments ± SD.

neither PDAD-MNP nor PSS-MNP led to a pronounced release of IL-6, IL-12p40, and TNFα pro-inflammatory cytokines beyond unstimulated control levels in Wt bulk DCs. No evidence as to PRR involvement was found due to the absence of released cytokines. However, LPS

stimulation resulted in a significant elevated sequestration of immune-stimulatory proteins into the supernatant in a TLR4-dependent manner.

On the other hand, none of the employed poly-electrolyte MNPs resulted in elevated levels of pro-inflammatory cytokines in the context of $TLR4^{ko}$ and $TLR9^{ko}$. Protein content did not exceed base-line levels recorded for untreated controls, and thus, further undermined the inertness of particle formulations employed.

3.2.4 Poly-Electrolyte MNP Stimulation of Macrophages

Macrophages are part of the RES system, and therefore, represent crucial entities in uptake and subsequent clearance of foreign matter, including synthetic MNPs[209]. Macrophages differentiate from monocytes that circulate the blood in steady state and extravasate upon terminal differentiation. In order for them to fulfill their role as scavengers in both steady-state and inflammation, they possess a vast amount of surface receptors and intracellular proteins such as TLRs[93].

In vitro, they can be differentiated from bone marrow precursors with the aid of M-CSF. This growth factor is critically involved in the proliferation and maintenance of bone marrow progenitor cells and monocytes, while additionally leading to the differentiation into macrophages and DCs[210]. Although macrophages can be obtained through the usage of other growth factors to some extent, M-CSF stimulation leads to a homogenous population of adherent precursors and macrophages, and thus, represents a suitable *in vitro* modeling system to study the cellular impact of MNP exposure.

3.2.4.1 M-CSF derived Macrophages: FACS Profiling and Gating Strategy

To ensure that cell populations of interest display phenotypic hallmark surface proteins of murine macrophages, flow cytometric analyses were performed prior to further experimental procedures. **Figure 3.20** outlines the gating strategy during cytometry measurements including live gating (Figure 3.20A) and $CD11c^{neg}CD11b^{pos}F4/80^{pos}$ pre-gating to yield viable macrophage populations (Figure 3.20B). Phenotypic status markers used include CD86 and Mac-3, both of which are known to be up-regulated upon cellular activation. In un-stimulated macrophages, expression of CD86 was absent and similar to control isotype staining (light

grey histogram, Figure 3.20B). On the other hand, Mac-3 was already expressed to some extent in un-stimulated immature macrophages on day seven of *in vitro* cultures. However, levels could be further increased following LPS stimulation as depicted in Figure 3.20.

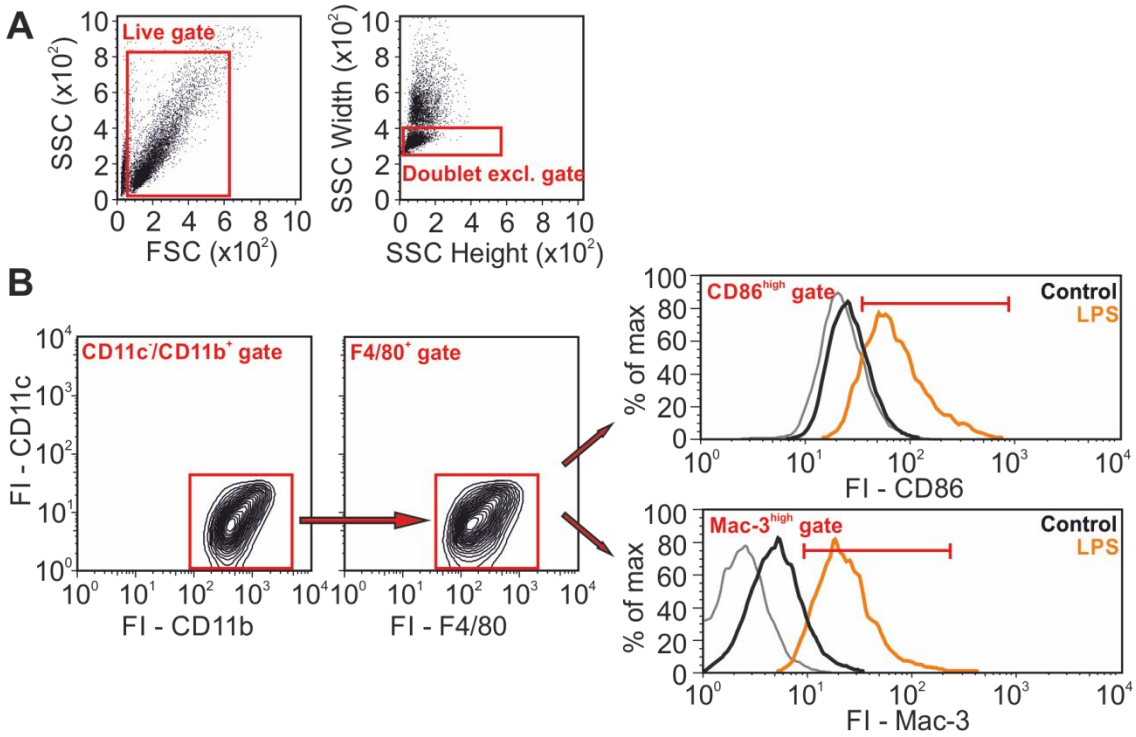

Figure 3.20 FACS gating strategy of M-CSF generated macrophages. A) Gating strategy of differentiated hematopoietic cells to yield live cells. **B)** Gating strategy to differentiate between macrophages and undesired cell populations in culture with the aid of macrophage-specific surface markers. Marker criteria included $CD11c^-$, $CD11b^+$, and $F4/80^+$ to exclude possible DC contamination in subsequent data interpretation. Right panel displays phenotypically important gates, namely $CD86^{high}$ and $Mac\text{-}3^{high}$ used for final data interpretation. Shown are histograms of isotype control stainings (light grey), unstimulated control (black), and LPS treated macrophages (orange) of one representative experiment.

3.2.4.2 Macrophages: Phenotype in the Context of TLR4 Knockouts

Cytometric surface profiling of CD86 and Mac-3 was performed after MNP stimulation of M-CSF generated murine macrophages in both the context of Wt and TLR4 knockout cells. **Figure 3.21** illustrates macrophage FACS profiles obtained after 24h of incubation with respective poly-electrolyte MNPs.

LPS yielded a significant up-regulation of both CD86 and Mac-3 surface proteins when compared to unstimulated control levels. However, elevated presence of the respective molecules dropped down significantly in case of TLR4 receptor knockout cells. PDAD- and PSS-MNPs did not result in an increase in surface expression of neither Mac-3 nor CD86, again substantiating the inertness of particle formulations.

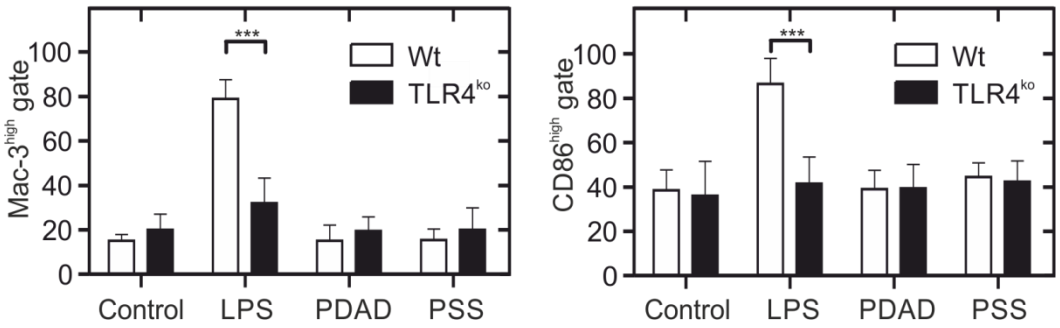

Figure 3.21 FACS profiling of macrophages stimulated with poly-electrolyte MNPs in the context of TLR4 receptor knockout cells. Numerical evaluation of data as outlined in Figure 3.20 for both PDAD-MNP and PSS-MNP in the context of TLR4 knockout cells. Shown are mean values of the percentage of cells within respective gates ± SD of three independent experiments.

3.2.4.3 ELISA Cytokine Secretion in the Context of TLR4 Knockouts

Macrophages are phagocytic cells of the innate immune system that sense potential harmful PAMPs and DAMPs within their immediate environment and react accordingly by recruiting additional immune cells through the release of pro-inflammatory cytokines[74]. Both TLR4 and the adaptor molecule ASC are critically involved in the recognition and subsequently resulting immunological consequences after PAMP and/or DAMP exposure, and thus, relevant knockout systems were included in these studies.

To test whether M-CSF generated murine macrophages sense poly-electrolyte MNP formulations as potentially harmful, ELISA measurements detecting released IL-6, IL-12p40, and TNFα in the context of TLR4 receptor knockout cells were performed.

As shown in **Figure 3.22**, all particle suspensions were tolerated by macrophages and did not induce significant release of tested cytokines. As expected, treatment of murine macrophages with LPS resulted in a significant decrease of secreted cytokine levels in TLR4 knockout cells. ASC^{ko}, however, displayed protein release similar to Wt macrophages.

In summary, synthetic poly-electrolyte nanoparticle formulations proved to be biologically inert within murine macrophages independent of their size and surface makeup.

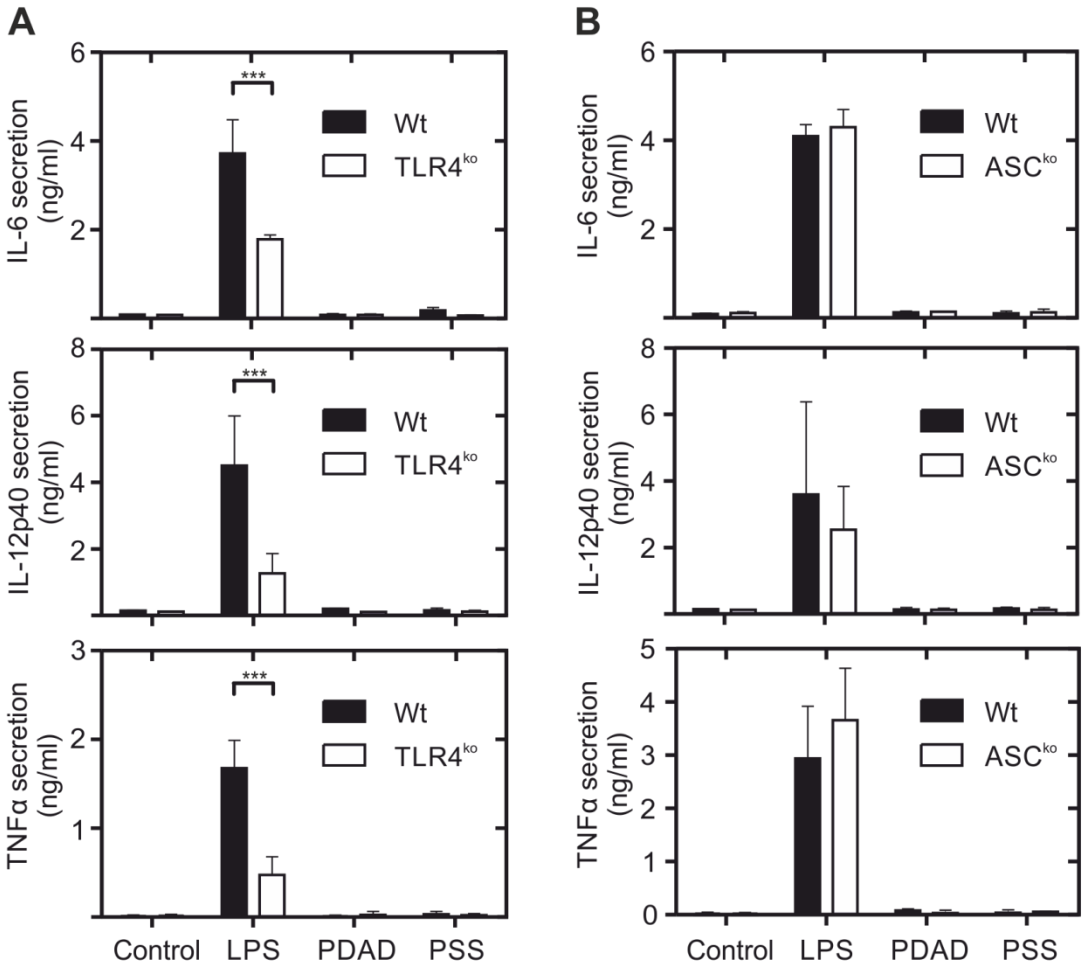

Figure 3.22 Cytokine secretion of poly-electrolyte MNP-pulsed macrophages in the context of knockout mice. A) Vertical panel displaying IL-6, IL-12p40, and TNFα cytokine secretion levels in both the presence and absence of the TLR4 receptor. **B)** Vertical panel showing cytokine secretion in both the presence and absence of the ASC adaptor protein. Cells were incubated for 24 h in the presence of the respective MNP and supernatants collected afterwards for further ELISA analyses. Boxes display mean values of two independent experiments ± SD.

3.2.5 Mixed Splenocyte Responses after Poly-Electrolyte MNP Stimulation

Secondary lymphoid organs such as lymph nodes are the primary site of adaptive immune responses[81]. Antigenic information acquired from peripheral tissues is brought into close proximity with both T- and B-lymphocytes that are capable of translating the peptide information presented to them through immigrating APCs. As a result, massive cell division and proliferation increases the potential number of clones being able to mount an immune reaction against a specific antigen[46,91]. In the case of T cells being activated through migratory or lymph node resident DCs, one of several effector phenotypes (Th1, Th2, Th17, Treg) is induced[78,211]. In the case of lymph-borne antigens such as MNPs, particles undergo immune surveillance in secondary draining lymph nodes, and thus, splenocyte cultures were employed to mimic *ex vivo* immunological detection of soluble antigens.

This process is highly dependent on the size and overall surface properties of administered iron oxide based contrast agents. In this case, lymph node resident immune cells are responsible for the identification, uptake and resulting lymphocyte priming[212].

3.2.5.1 T cell Proliferation Capacity after LbL-MNP Stimulation

Mixed splenocytes were harvested from explanted spleen and prepared to yield a homogenous cell population through mechanical disintegration as well as enzymatic action. MNP stimulation was carried out for a period of 72 h and cell numbers were assessed. These served as an indication of overall cell division events taking place as a result of MNP exposure accumulating throughout the incubation time.

As depicted in **Figure 3.23**, approximately $0.5x10^6$ cells remained after 72 h of incubation in case of unstimulated control samples. On the other hand, LPS stimulated controls resulted in a 3-fold increase of total splenocytes, whereas CpG treated populations did not alter cell numbers when compared to negative controls.

In summary, none of the poly-electrolyte MNPs tested proved to be able to induce cellular proliferation and division events under the experimental conditions. Total splenic cell populations after 72 h of incubation with PDAD- and PSS-MNP did not yield a significant increase in cell numbers when compared to unstimulated control samples.

To further substantiate findings obtained with whole spleen cultures, explanted single cell suspensions were labeled using CFSE dye. The succinimidyl-group of this stain covalently binds to intracellular proteins, and thus, is retained within target cells. Upon cellular division events, the total amount of the dye is passed on to equal amounts to both daughter cells, allowing a quantitative estimation of cellular activity. Using flow cytometry, the fluorescence signal of each cell can be obtained and compared separately. To ensure correct gating strategy, $CD45^+CD3^+$ double positive cells were pre-gated to exclude B cells and other spleen-derived cell populations (Figure 3.23A).

Figure 3.23C displays CFSE fluorescence intensities after 72 h of MNP exposure of both $CD4^+$ and $CD8^+$ T cell populations. Splenocytes were first explanted, mechanically and enzymatically resuspended, and subsequently labeled with CFSE.

Apart from LPS control stimulation, none of the poly-electrolyte MNPs employed was capable of inducing T cell proliferation within single cell suspensions of splenic explants. CFSE patterns showed a marked decrease of fluorescence in LPS treated total spleen populations when compared to the maximum signal of untreated splenocytes (FI~10^3), providing evidence as to cellular division events of pre-gated T cells.

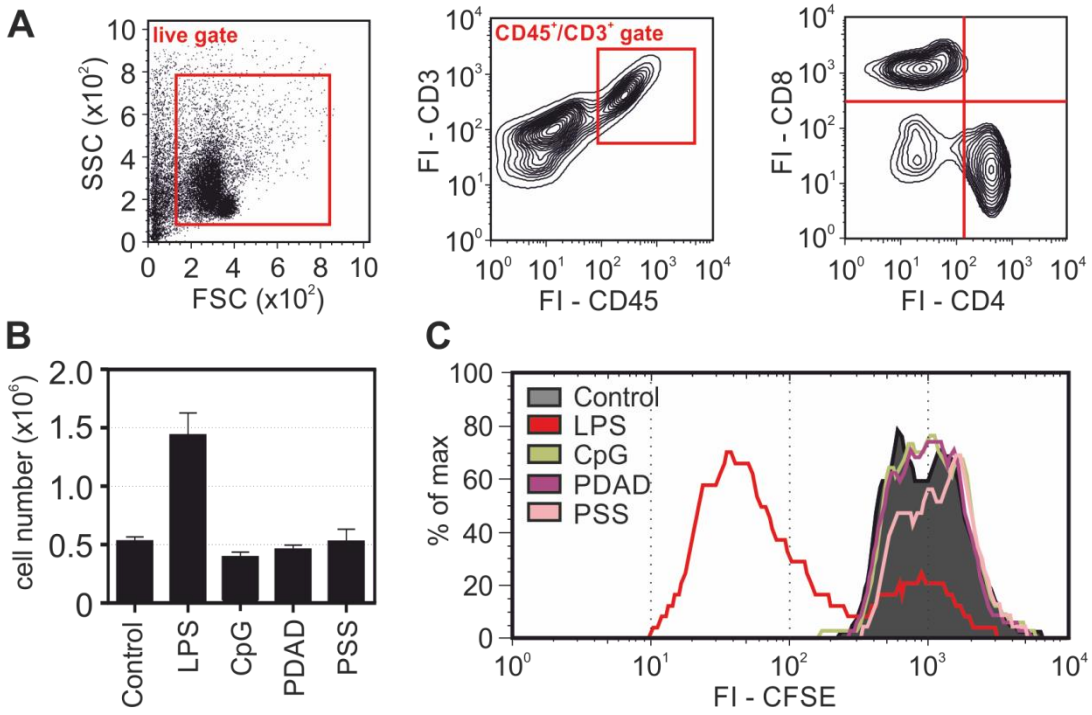

Figure 3.23 Mixed splenocyte reactions to evaluate T-cell proliferation capacity following poly-electrolyte MNP stimulation. A) Live gating of total splenocyte population after 72 h including $CD45^+CD3^+$ positive selection criteria for T-cell populations. Both $CD4^+$ and $CD8^+$ cells used in further evaluations. **B)** Total number of splenocytes remaining after 72 h of incubation given the respective stimulus. Shown are mean values ± SD of two independent experiments (n=2). **C)** Histograms of CFSE staining intensity as a function of T-cell proliferation measured using flow cytometry. Displayed is one representative experiment (n=2).

Overall, CFSE labeling of total splenocyte populations revealed that potentially lymph born synthetic MNPs would not alter cell numbers of total T cell populations. Therefore, both PDAD and PSS particle functionalization were regarded biologically inert.

3.3 Immunological Properties of Bacterial Magnetosomes

Biogenic magnetosomes represent bacterial organelles organized into membranous chains of iron oxide cores[213]. The linear structure serves as a compass, allowing certain bacterial strains to orientate themselves in geomagnetic fields, a process termed magnetotaxis[165]. Magnetosome crystals possess high chemical purity, narrow size ranges, and species-specific

crystal morphologies. Unlike synthetic MNPs, magnetosomes are composed of large single domain iron cores that reach diameters of up to 30-45 nm. Interestingly, iron oxide structures displaying these properties cannot be successfully synthesized using modern state of the art chemistry. This fact makes them particularly interesting for molecular imaging approaches as well as possibly introducing immunological consequences due to their bacterial origin.

3.3.1 Hematopoietic Progenitor Cells

3.3.1.1 Biocompatibility Studies of Bacterial Magnetosomes using HSCs

In order to investigate the potential of MSR-1 to induce adverse cytotoxic effects within HSCs, biocompatibility studies were performed. As illustrated in **Figure 3.24**, both concentration-dependent and long-term MNP exposure treatments were employed. Figure 3.24A depicts percent survival of MNP-exposed HSCs with increasing magnetosome

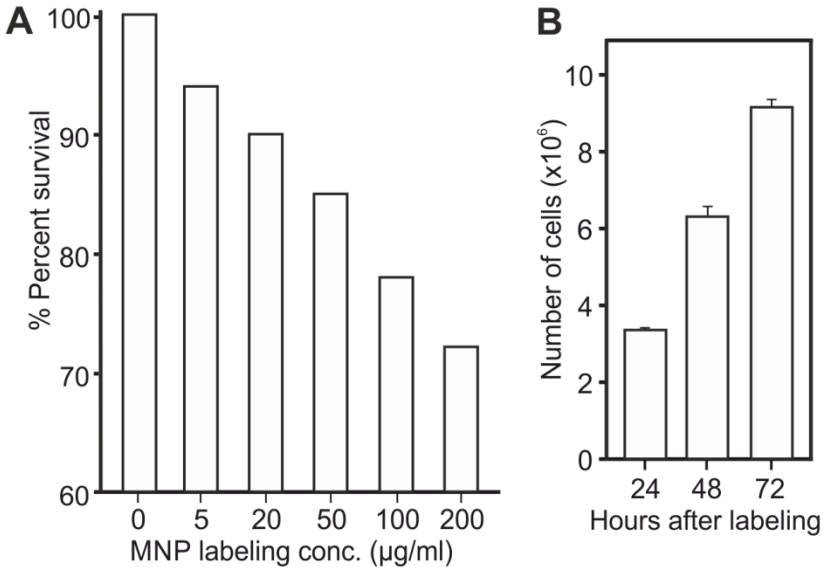

Figure 3.24 Biocompatibility studies of MSR-1 MNP using HSCs. A) Cytotoxic effects of increasing magnetosome labeling concentrations on proliferating HSCs. Iron oxide concentration ranged from 0-200 µg/ml. Displayed is one representative experiment (n=3). **B)** Long-term cytotoxic assessement of MSR-1 labeled HSCs for up to 72 h to address possible adverse effects on cell proliferation arising due to extended MNP exposure. Target cells were seeded at $2x10^6$ prior to MSR-1 labeling and left undisturbed for the remainder of the assay. Experimental data in A) used to optimize labeling concentration in further studies. Shown are mean values ± SD (n=3).

concentrations. Even though surviving cell numbers dropped when increasing MNP concentration up to 200 µg/ml, levels of remaining HSCs were comparable to other MNPs employed in similar studies (Figure 3.1A). As previously observed, a correlation between surviving HSCs and iron oxide labeling concentration showed a dose-dependent cytotoxic

effect of labeled HSCs. Furthermore, cellular amplification was not compromised after long-term incubation with MSR-1 for 72 h. As illustrated in Figure 3.24B, cell numbers remained within acceptable levels when compared to Figure 3.1B.

3.3.1.2 MSR-1 Uptake Studies employing HSCs

Uptake studies of bacterial MSR-1 into proliferating HSCs were employed using a labeling concentration of 10 µg/ml. As illustrated in **Figure 3.25**, approximately 25% of total HSCs successfully incorporated biogenic MNPs. When compared to other MNP formulations employed in similar studies (refer to Figure 3.2), labeling with MSR-1 resulted in a high percentage of total HSCs acquiring magnetic properties due to MNP uptake.

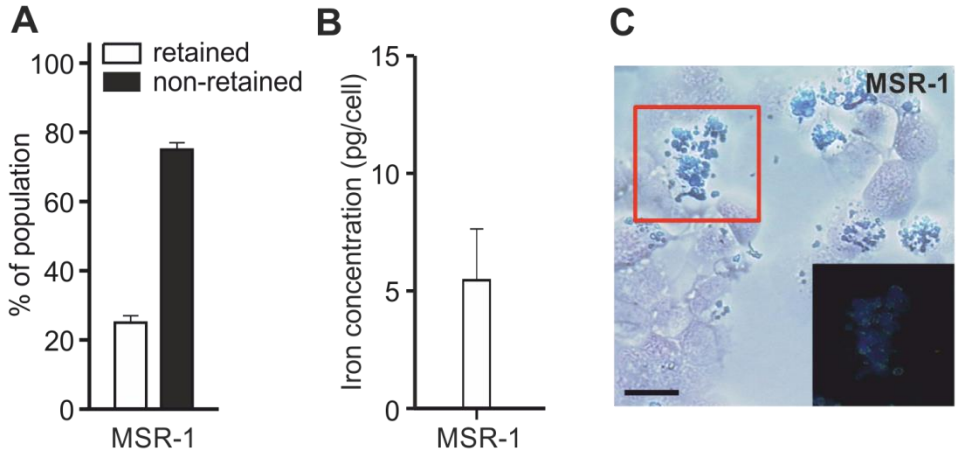

Figure 3.25 Quantitative and qualitative MNP uptake studies into HSCs. A) Magnetic separation techniques of HSC bulk cultures were employed to separate cell populations that acquired magnetic properties due to iron oxide incorporation from their unlabeled counterparts after 24 h of MSR-1 incubation. Both fractions of labeled and unlabeled cells yielded total cell counts and the percentage of retained and non-retained cells was calculated. **B)** Iron assay displaying average amount of molecular iron taken up by magnetically pre-selected MSR-1 labeled HSCs in pg/cell. Displayed are mean values ± SD (n=3) normalized against background iron levels present in unlabeled control samples. **C)** Prussian blue staining of fixed cytospins. Blue areas correspond to iron deposits. Counter staining of membranes employing Neutral Red. Boxed area shown in upper left corner are displayed using dark field microscopy (400x). Scale bar 20 µm.

However, intracellular iron concentrations of magnetically pre-selected HSCs remained low. On average, only 6 pg of iron per cell was measured. Apart from Chit-MNP previously discussed, MSR-1 resulted in the lowest intracellular iron concentration when compared to poly-electrolyte coated MNPs (Figure 3.2B).

Potential clustering effects of biogenic MNPs arising in aqueous solutions and intracellular localization were visualized employing Prussian blue stainings of fixed cytospins. As depicted

in Figure 3.25C, MSR-1 MNPs were successfully incorporated into HSCs. However, larger aggregates of particles appear to be adhering to the outer membrane of target cells.

In summary, bacterial magnetosomes were taken up by a large amount of cells, although not to a high degree when compared to other MNP formulations. Histological stainings confirmed intracellular localization of particle agglomerates.

3.3.1.3 Phenotypic Profiling of MSR-1 pulsed HSCs

In order to investigate surface marker make-up of magnetosome pulsed HSCs, flow cytometric analyses were performed. Cells were labeled for 24 h and magnetically separated prior to experimental procedures. As illustrated in **Figure 3.26**, no significant differences in surface marker profiles were detected when comparing MSR-1 labeled HSCs with untreated control samples. The adopted gating strategy employed to yield numerical evaluation of data is outlined in Figure 3.4A. In summary, exposure of HSCs with bacterial MNPs did not induce any phenotypic alterations of CD11b, CD11c, CD24 and Flt3 that would suggest the induction of differentiation or potential adverse effects arising as a consequence of bacterial MSR-1 exposure.

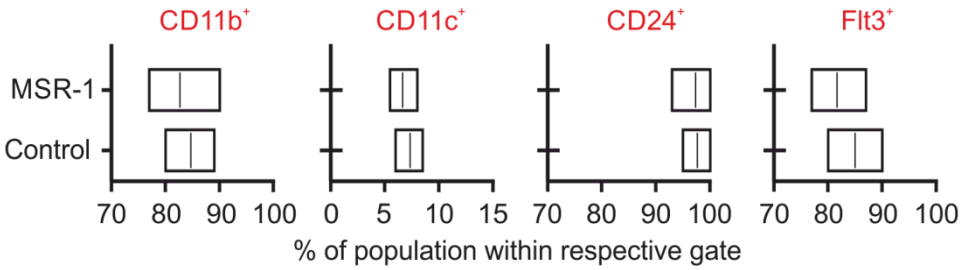

Figure 3.26 Phenotypical FACS analysis of MSR-1 pulsed HSCs. Depicted are numerical evaluations of surface stainings for CD11b, CD11c, CD24 and Flt3. Respective gating strategy outlined in Figure 3.4A. Depicted are mean values (vertical lines) ± min/max values (boxed) of three independent experiments.

3.3.1.4 Molecular Imaging Properties Employing MSR-1

In vitro phantom studies were employed to investigate MR imaging characteristics of bacterial magnetosomes. In brief, defined numbers of MSR-1 labeled HSCs were immobilized within agarose and subjected to MR imaging. As depicted in **Figure 3.27**, labeling of HSCs with bacterial MNPs resulted in a marked decrease of signal intensity when

compared to controls (Figure 3.27A + C). Bacterial magnetosomes could be imaged down to a minimum detection limit of 10^2 cells, rendering them particularly attractive for the imaging of low numbers of target HSCs. When compared to similar studies employing poly-electrolyte and lipid-shell MNPs, MSR-1 MNPs displayed remarkable MR characteristics given these experimental settings. Due to their low T2* relaxation time values (32 ms ± 8 ms), magnetosomes proved to be a valuable contrast agent for imaging of HSCs using MRI.

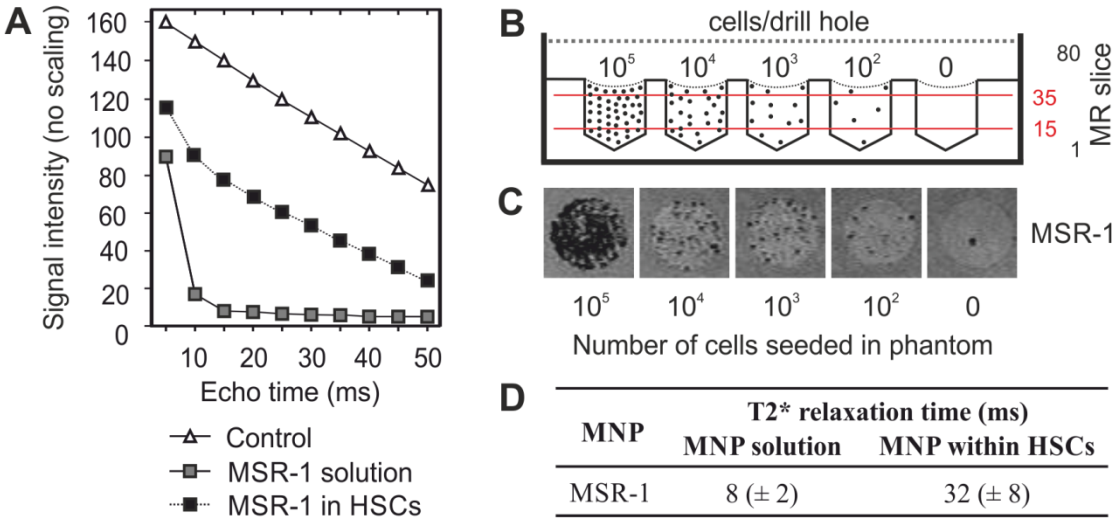

D

MNP	T2* relaxation time (ms)	
	MNP solution	MNP within HSCs
MSR-1	8 (± 2)	32 (± 8)

Figure 3.27 ***In vitro*** **MRI studies using MSR-1 labeled HSCs. A)** Numerical depiction of map scan data performed by consecutively increasing echo times (5 ms increments) and recording remaining signal intensities. Displayed are T2* relaxation kinetics of aqueous magnetosome solutions alone and after cellular uptake employing HSCs. MNP solutions equilibrated to final concentration of 10 µg/ml prior to seeding into phantoms. Initial labeling concentration of cells: 10 µg/ml. Shown are respective signal intensities of one representative experiment (n=3) at various echo times pre-defined during map scan protocol design. **B)** Cross-sectional schematic of agarose phantoms harboring MSR-1 labeled HSCs. Scan slices 15-35 (red horizontal lines depict cut-offs) used to mount 3D image stacks depicted in C). Inhomogenous volumes outside of cut-offs were not used in further data evaluation. **C)** T2*-weighted 3D MRI gradient echo scans to evaluate hypo-intense regions of signal-loss due to MSR-1 incorporation inside HSCs. Minimum and maximum detection limits were evaluated and corresponding phantom pictures with respective seeding density depicted. Displayed are resulting 3D image stacks of individual scan slices (15-35) merged using ImageJ software . **D)** Extracted numerical T2* values as fitted by software algorithm as a result of map scan protocols. Shown are aqueous MSR-1 suspensions alone (center column) and after magnetic separation of labeled HSCs (right column) by employing a T2* weighted MRI map scan. Values fitted and calculated using Bruker ParaVision software. Averaged numbers represent mean values of three independent experiments ± SD.

3.3.2 Inflammatory Dendritic Cells (iDCs)

3.3.2.1 Uptake Properties of Bacterial Magnetosomes into Inflammatory DCs

To investigate the uptake potential of MSR-1 MNPs into GM-CSF derived iDCs, cells were labeled for 24 h and magnetically separated as previously discussed. As outlined in **Figure 3.28**A, MSR-1 particles were taken up by iDCs to a high extent. Approximately 80% of immature cells successfully integrated bacterial MNPs. Due to their size and large magnetic

core structures, an iron amount of 50-65 pg/cell accumulated in positively selected iDCs (Figure 3.28B).

TEM images as shown in Figure 3.28C support these results. MSR-1 particles consist of large iron cores linked by structural proteins, leading to their chain-like appearance[213]. According to high magnification TEM images, magnetic cores possess a diameter of 30-45 nm, which is extremely large compared to synthetic core sizes of other MNPs employed (refer to Table

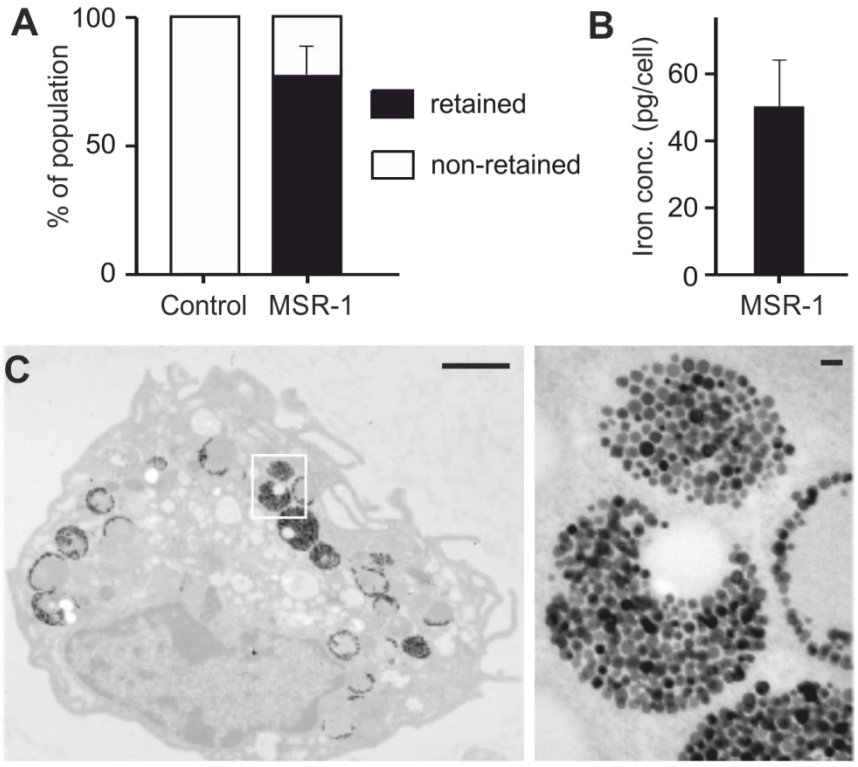

Figure 3.28 GM-CSF derived iDC uptake of bacterial MSR-1 magnetosomes. A) Displayed are magnetically retained cell fractions versus unlabeled non-retained counterparts ± SD (n=3). **B)** FerroZine assay determining average iron load per cell in pg of magnetically pre-selected labeled cell fractions. Depicted are mean values ± SD (n=3). **C)** TEM images of intracellular MSR-1 vesicles within tipDCs. Scale bars 2 µm (left image), and 100 nm (right image). Boxed area denotes area of magnification shown in right image.

3.2). TEM images revealed that cells indeed completely internalized magnetosomes into intracellular compartments. As shown in Figure 3.28C (left image), endosomal compartments harboring MSR-1 clusters are confined to the cytosol. No magnetosomes were detected within nuclear regions or adhered to the outer cell membrane. Dendrites extending from the cell membrane could be observed, pointing towards an activated phenotype of labeled cells.

In summary, bacterial magnetosomes were taken up to a high extent into iDCs. As visualized by TEM studies, organelles retained their chain-like structure inside endosomal compartments

after particle uptake. Furthermore, iDC membrane extrusions were clearly apparent, possibly providing evidence of an activated cellular phenotype.

3.3.2.2 Phenotypic iDC Cytometry Profiling of Bacterial Magnetosomes

Due to their bacterial origin and protein composure, bacterial magnetosomes were suspected to display an immunogenic nature when brought into proximity with *in vitro* generated phagocytic immune cells in previous experiments. Therefore, investigations as to the immunological impact of biogenic MNPs on immature iDCs using cytometry were conducted.

In order to address surface marker profiles of bacterial magnetosomes, flow cytometric analyses were performed. iDCs were labeled for 24 h, magnetically sorted and stained for lineage- and DC-specific markers.

Figure 3.29A+B display experimental settings used to analyze GM-CSF derived iDC populations. Live cell and doublet exclusion gating were selected prior to antibody gating

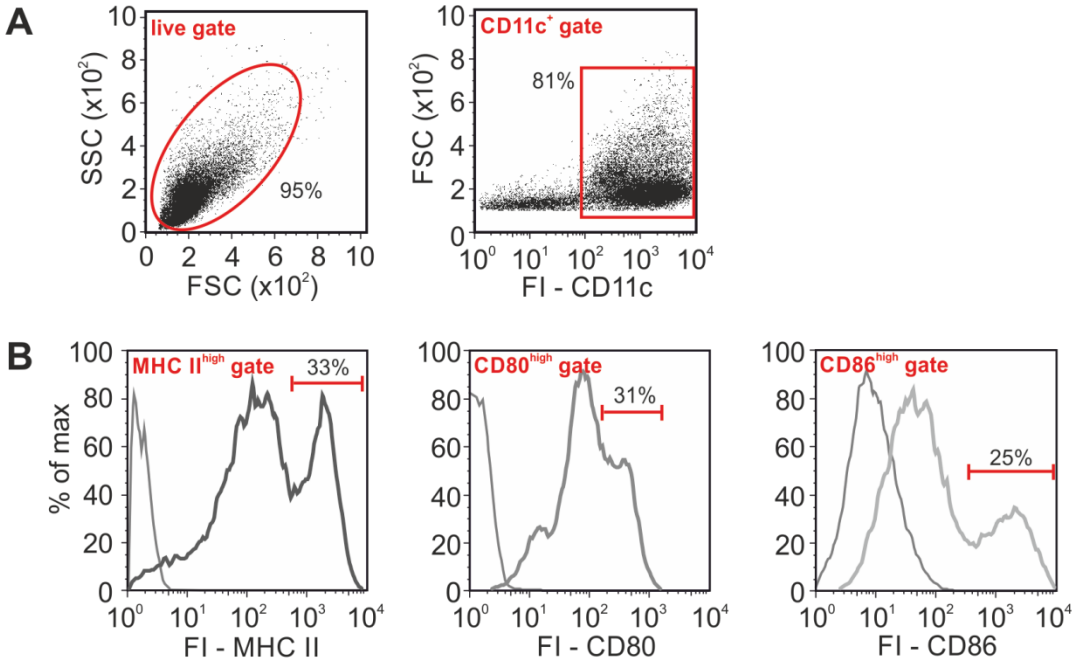

Figure 3.29 Phenotypic FACS gating strategy of GM-CSF derived inflammatory DC populations. **A)** Live gating on cell populations of interest further evaluated during final experimental acquisition of cell culture experiments including live and $CD11c^+$ gate. **B)** Pre-gated tipDC populations resulting from A) and gates of important surface markers of DC maturation states used for data compilation (red areas). Example of surface marker gating of unstimulated controls for $MHC\ II^{high}$, $CD80^{high}$ and $CD86^{high}$ as employed in further experimental procedures. Empty fair grey histograms depict isotype staining control samples.

strategies to exclude cell debris, dying cells or electronic measuring errors. Pre-gating on the

DC commitment marker $CD11c^{+}$ ensured that only inflammatory dendritic cells were analyzed in subsequent cytometry experiments, excluding $CD11c^{-}$ macrophage populations. As highlighted in Figure 3.29B, MHC II^{high}, $CD80^{high}$, and $CD86^{high}$ cell fractions were used to evaluate iDC maturation state of MSR-1 magnetosomes in further experiments.

Figure 3.30 depicts cytometry results acquired for MSR-1 particles after 24 h of labeling and subsequent magnetic separation. Gating strategy for GM-CSF derived iDCs followed procedures previously outlined in Figure 3.29A+B to exclude macrophage populations.

However, in contrast to previous experimental results gained through FACS employing inert synthetic MNPs, MSR-1 particles induced the up-regulation of co-stimulatory surface molecules CD80 and CD86. MHC II, CD80 and CD86 surface expression proved to be significantly increased after 24 h of incubation time when compared to control levels. LPS is

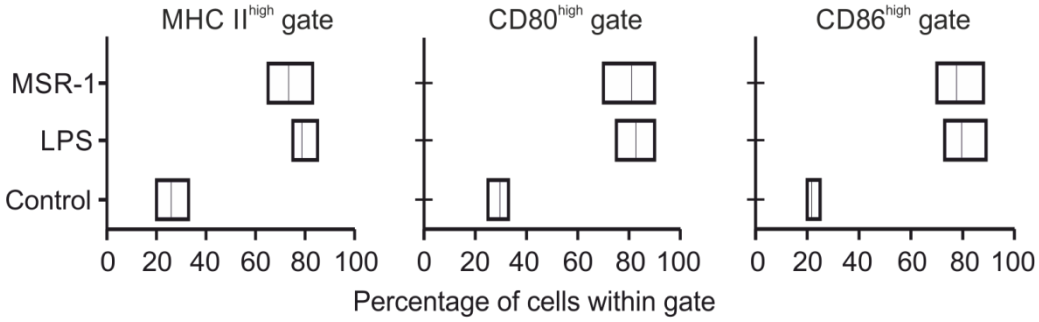

Figure 3.30 Phenotypic FACS profiling of GM-CSF derived iDC populations employing bacterial MSR-1 magnetosomes. Numerical evaluation of gates shown in Figure 3.29 after exposure of immature bulk tipDC culture to bacterial magnetosomes MSR-1. Untreated control stainings as well as positive LPS activation depict unchanged phenotype as well as cellular activation, respectively. Depicted are means (vertical lines within boxes) ± min/max values (boxes) of three independent experiments.

known to induce DC maturation and activation, and like MSR-1, approximately 80% of total iDC populations were found to be present within activated gates as outlined in Figure 3.29B.

3.3.2.3 *In Vitro* Migration Assay using iDCs and MSR-1 Stimulation

To further substantiate cytometric findings, *in vitro* migration assays in the context of $MyD88^{-/-}$ knockout cells were performed. As previously noted, MyD88 represents a cardinal adapter protein crucial for TLR signaling cascades involved in cellular activation[214]. Receptor-mediated signaling in turn leads to NFκB-dependent activation of genes driving immunological consequences. Due to the bacterial nature of magnetosome organelles, involvement of TLR4 was suspected.

As shown in **Figure 3.31**, treatment of immature iDCs with magnetosomes resulted in a robust increase in the number of cells migrating towards increasing chemokine concentration. Baseline migratory behavior of unstimulated controls was attributed to the developmental heterogeneity arising within the *in vitro* cell culturing system. However, numbers of migrated cells remained within tolerance levels when compared to stimulated migratory iDCs.

Treatment of cells with the positive control LPS resulted in comparable numbers of migratory iDCs when compared to MSR-1. Since LPS is known to signal via TLR4, it was not surprising that migratory behavior was significantly reduced in case of MyD88$^{-/-}$ knockout cells. As displayed in Figure 3.31, the same holds true for MSR-1 stimulated cell populations, although to a lesser extent than in MyD88$^{-/-}$ controls stimulated with LPS. In summary, MSR-1 stimulated iDC populations showed profound migratory capacity after 24 h of biogenic MNP exposure that was significantly reduced in the case of MyD88 deficient knockout cells.

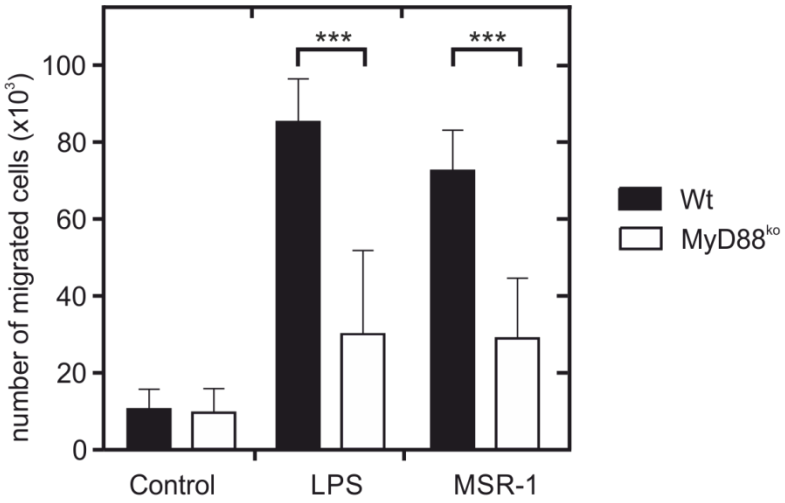

Figure 3.31 *In vitro* migration assay in the context of MyD88 adaptor protein knockout mice. GM-CSF derived iDCs were labeled with bacterial MSR-1 MNPs for 24 h, magnetically separated and subsequently seeded into Transwell migration plates allowing directional migration through a membrane towards ELC chemo-attractant. Number of trans-migrated cells served as an indication of fully activated DC phenotype. All values displayed in response to ELC chemokine gradient normalized against undirected migration of unstimulated iDCs in the absence of chemotactic signals. Shown are mean values of two independent experiments ± SD.

3.3.3 MSR-1 stimulated Flt3L-Generated DC Subsets

3.3.3.1 FACS Profiling of MSR-1 Pulsed cDC Populations

Figure 3.32 depicts numerical evaluation of $CD80^{high}CD86^{high}$ gates resulting as a consequence of the gating strategy employed in Figure 3.15. As previously reported employing GM-CSF derived iDCs, bacterial magnetosomes triggered significant up-regulation of assessed surface marker levels in Wt Flt3L derived cDC populations. As shown in Figure 3.32A, PRR knockout models ($TLR4^{ko}$, $TLR9^{ko}$) as well as downstream adaptor molecule knockouts ($MyD88^{ko}$, ASC^{ko}) were employed to illustrate potential recognition mechanisms and resulting signaling dependencies. Cellular maturation due to LPS treatment

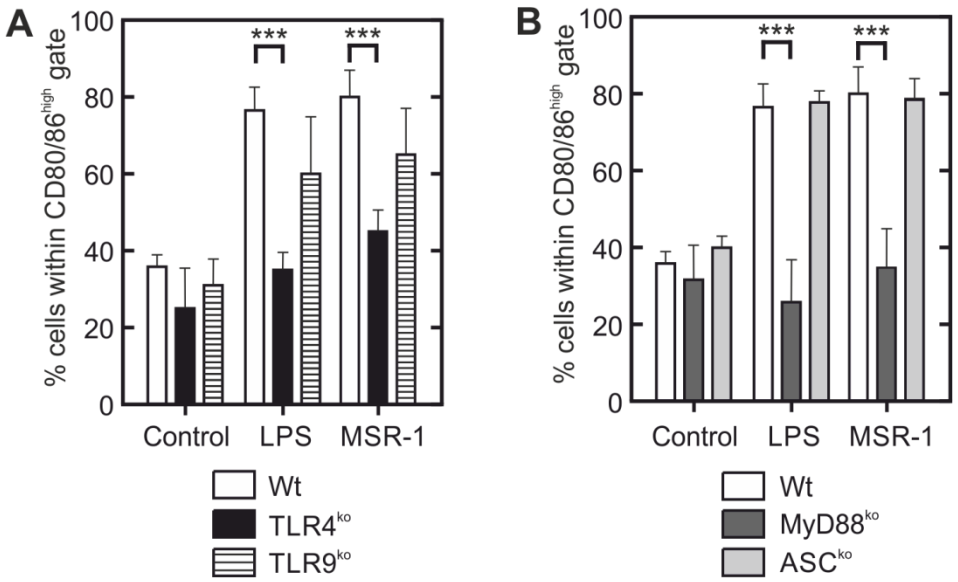

Figure 3.32 FACS profiling of Flt3L generated cDCs in the context of TLR receptor and adaptor knockout mice. A) Respective populations within $CD80/86^{high}$ gate of Wt, TLR4 and TLR9 receptor knockout cells. **B)** Percentages of populations within pre-defined gates in the context of adaptor protein knockout cells (MyD88 and ASC). Data shown are mean values of two independent experiments ± SD.

resulted in the up-regulation of both CD80 and CD86 surface levels. Markedly, MSR-1 stimulated Flt3L generated cDCs resulted in comparable surface molecule densities. Similar to LPS treatment, MSR-1 dependent up-regulation and activation of cells appeared to be TLR4 dependent. In the absence of functional TLR4, elevation of both CD80 and CD86 was significantly diminished. Due to the fact that TLR4 signals through MyD88, surface protein levels were also reduced in case of MyD88 knockout cells. TLR9 and ASC deficiency resulted in surface molecule levels similar to Wt conditions, illustrating the lack of involvement of these proteins in surface marker expression using MSR-1 magnetosomes.

In summary, MSR-1 treated cDC populations resulted in a robust increase of maturation dependent surface markers in cytometric measurements. A significant reduction of both TLR4 and MyD88 deficient percentages was measured within respective gates of Flt3L derived cDCs.

3.3.3.2 FACS Profiling of MSR-1 Pulsed pDC Populations

Numerical data of MHC II^{high} and $CD86^{high}$ gates are outlined in Figure 3.17. Even though pDCs did not yield activation levels of previously discussed cDCs after LPS stimulation, a significant increase in surface marker levels was noted. This increase in surface protein levels

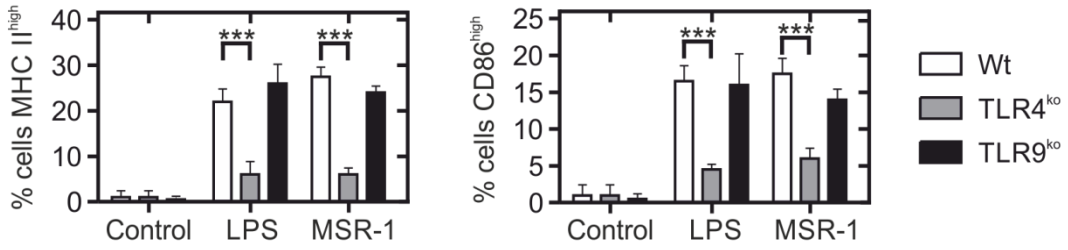

Figure 3.33 FACS profiling of Flt3L generated pDCs in the context of receptor knockout models. Numerical evaluation of example data shown in Figure 3.17 for biogenic MSR-1 MNPs in the context of TLR4 and TLR9 receptor knockout cells. Shown are mean values of the percentage of cells within respective gates ± SD of two independent experiments for both $CD86^{high}$ and MHC II^{high} regions.

was also observed in pDC populations after MSR-1 stimulation (**Figure 3.33**). Values dropped down significantly in case of TLR4 knockout cells. LPS as well as MSR-1 stimulation using TLR9 knockout cells resulted in a pronounced cellular activation comparable to Wt activation. This is in marked difference to unstimulated control pDCs that showed base-line presence of respective surface markers.

In summary, both Wt and TLR9 knockout pDC were activated after magnetosome exposure. This activation was significantly reduced in case of TLR4 knockout cells similar to LPS control levels, pointing toward a signaling involvement of this respective pattern recognition receptor.

3.3.3.3 Cytokine Release of Bulk Flt3L derived DC after Magnetosome Exposure

The secretion of pro-inflammatory cytokines after cellular activation is an important feature of DCs resulting in the recruitment of additional cellular mediators driving the immune

response. To investigate the potential of bacterial MSR-1 magnetosomes to induce IL-6, IL-12p40, and TNFα, supernatants of bulk DCs were collected after MNP exposure and ELISA measurements performed.

As illustrated in **Figure 3.34**, labeling of bulk Flt3L generated cell cultures led to a pronounced secretion of pro-inflammatory cytokines in both WT and TLR9 knockout cells. Levels of LPS treated cells and bacterial magnetosomes resulted in comparable amounts of sequestered protein levels. However, secretion of cytokines was abolished in case of TLR4 knockouts in both LPS and MSR-1 treated cells. Interestingly, sequestration of IL-12p40 was not altered when compared to Wt and TLR9 knockout cells.

In summary, treatment of cDC and pDC bulk cultures led to a significant release of pro-inflammatory cytokines after 24 h of incubation, undermining cytometric results previously discussed.

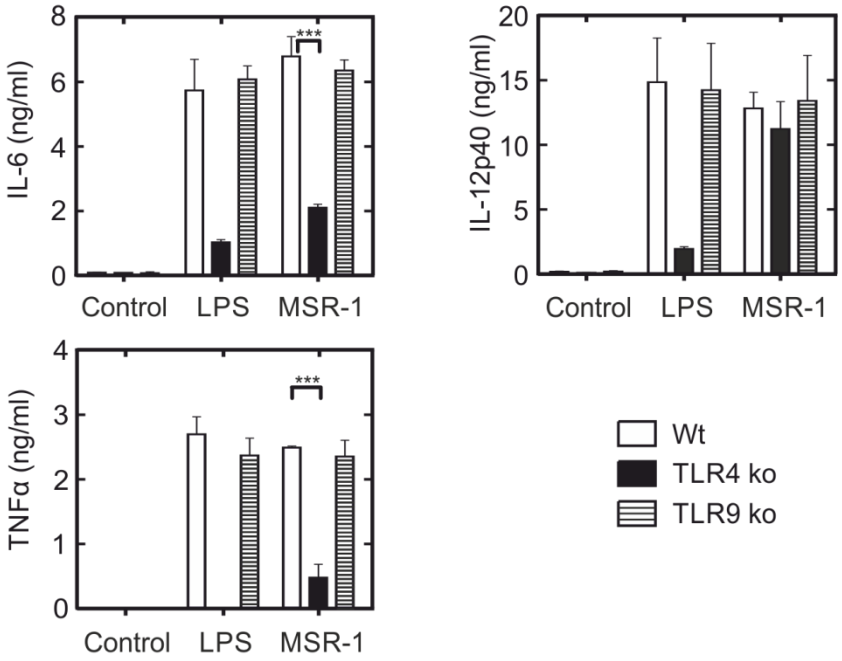

Figure 3.34 Cytokine secretion of MSR-1 stimulated bulk DCs. Cell culture supernatants of Flt3L generated DCs used in ELISA assays in the context of TLR4 and TLR9 receptor knockout mice after stimulation with bacterial magnetosomes. Bars represent mean values of two independent experiments ± SD.

3.3.4 Bacterial Magnetosomes in the Context of MSR-1

3.3.4.1 Phenotypic Analysis Employing Cytometry

Next, the impact of bacterial magnetosomes on M-CSF derived macrophage populations was investigated. In normal physiological conditions, macrophages represent the first line of defense against invading pathogens and exogenously introduced MNPs. As shown in **Figure 3.35**, cytometric data suggest cellular activation of MSR-1 pulsed macrophages due to the significant elevated levels of both CD86 and Mac-3. Gating strategy employed to yield macrophage populations is illustrated in Figure 3.20. Briefly, $CD11b^{+}CD11c^{-}$ gates were employed to exclude DCs arising throughout *in vitro* culturing. Surface expression of the macrophage marker F4/80 was employed to yield viable macrophages for subsequent data analyses.

Mac-3 is already expressed to some extent in immature macrophage populations, however, elevated levels were recorded in both LPS and MSR-1 treated cells. Concomitantly, CD86 is further up-regulated after cellular activation in Wt cells. As shown in Figure 3.35, surface

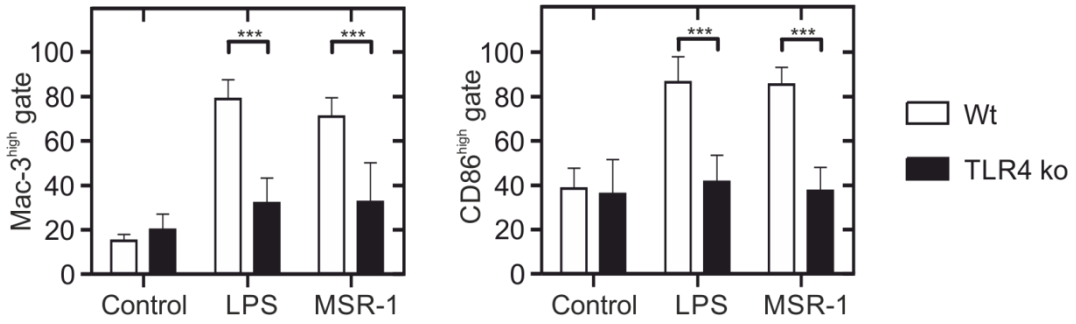

Figure 3.35 FACS profiling of macrophages in the context of TLR4 receptor knockout cells. Numerical evaluation of example data shown in Figure 3.20 for bacterial magnetosomes MSR-1 employed in the context of TLR4 knockout cells. Shown are mean values of the percentage of cells within respective gates ± SD of three independent experiments.

marker levels of TLR4 knockout macrophages are significantly reduced and display values similar to negative controls in both LPS and MSR-1 treated cells.

3.3.4.2 Macrophage ELISA Data

Macrophages are phagocytic cells of the innate immune system that sense potential harmful PAMPs and DAMPs within their immediate environment and react accordingly by recruiting other immune cells through the release of pro-inflammatory cytokines[44].

To test whether M-CSF generated murine macrophages sense MNP formulations as potentially harmful, we performed ELISA measurements detecting released IL-6, IL-12p40, and TNFα in the context of TLR4 receptor knockout cells.

As shown in **Figure 3.36**, biogenic MSR-1 led to a pronounced sequestration of IL-6, IL-12p40, and TNFα in case of Wt macrophages. However, when employing TLR4 knockout cells, protein levels in supernatants were dramatically reduced, even though they remained elevated when compared to baseline levels in untreated controls. These experimental results are in agreement with data previously obtained, pointing at a high cellular activation potential of bacterial magnetosomes in a TLR4 dependent manner.

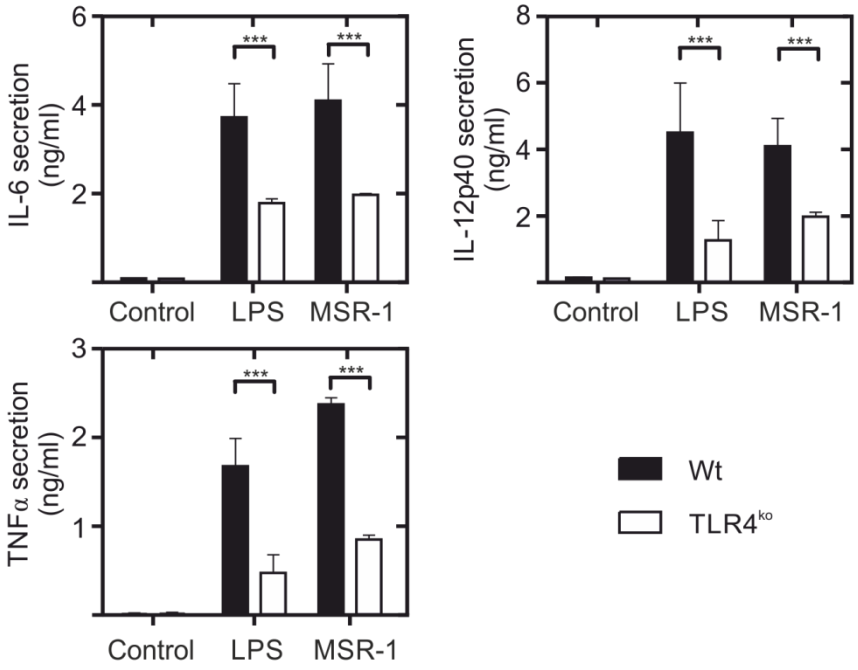

Figure 3.36 Cytokine secretion of MNP-pulsed macrophages in the context of receptor knockout mice. IL-6, IL-12p40, TNFα cytokine secretion levels in both the presence and absence of TLR4 receptors. Cells were incubated for 24 h in the presence of bacterial MSR-1 and supernatants collected afterwards for further ELISA analyses. Boxes display mean values of two independent experiments ± SD.

3.3.5 Mixed Splenocytes in the Context of MSR-1

Mixed splenocytes were harvested from explanted spleen and prepared to yield a homogenous cell population through mechanical disintegration as well as enzymatic action. MNP stimulation was carried out for a period of 72 h and cell numbers were assessed. These served as an indication of overall cell division events taking place as a result of MSR-1 exposure accumulating throughout the incubation time.

As depicted in **Figure 3.37**, approximately 0.5x10^6 cells remained after 72 h of incubation in case of unstimulated control samples. On the other hand, LPS stimulated controls resulted in a 3-fold increase of total splenocytes, whereas CpG treated populations did not alter cell numbers when compared to negative controls.

MSR-1 proved to be able to induce cellular proliferation and division events under the experimental conditions. Total splenic cell populations after 72 h of incubation increased to approximately 1.5x10^6 cells when compared to only 0.5x10^6 in untreated control samples.

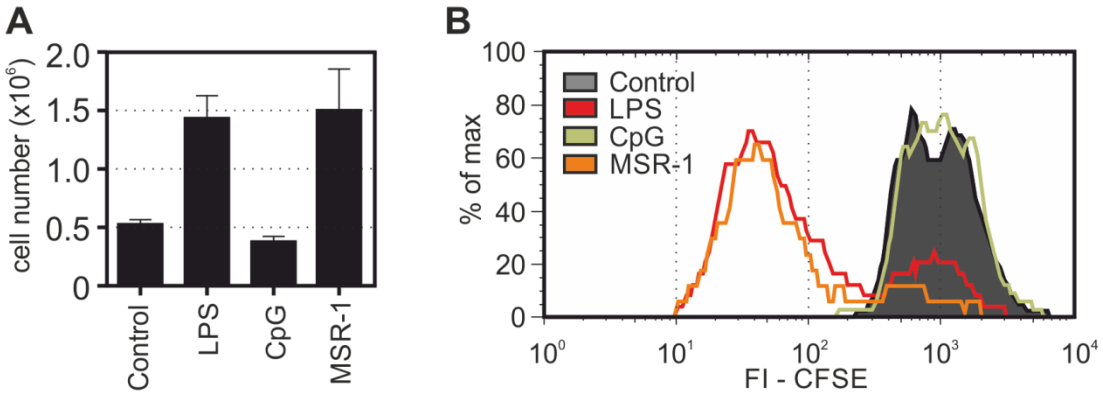

Figure 3.37 Mixed splenocyte reactions to evaluate T-cell proliferation capacity of bacterial MSR-1 MNPs. A) Total number of cells after 72 h of incubation resulting from potential T-cell proliferation events. Shown are mean values ± SD of two independent experiments (n=2). **B)** Histograms of CFSE intensity as a function of T-cell proliferation using magnetosomes. Shown is one representative experiment (n=2).

3.3.6 Macrophages in the Context of Innate Immunity

3.3.6.1 Magnetosomes and the Inflammasome Pathway

The inflammasome is governed by a series of intracellular proteins and receptors responsible for the cleavage of caspase-1 that ultimately leads to the sequestration of functional IL-1ß. A series of proteins including the NOD-like and RLH receptors and NALP proteins are responsible for both (i) the recognition of antigens as well as (ii) mounting subsequent immunological consequences[148].

IL-1ß is a crucial inflammatory cytokine that that been shown to be particularly important in mounting an appropriate immune response against intracellular bacterial infections, especially in the context of endogenous danger signals[148,215]. In order for IL-1ß to be exported from the cytoplasm, two independent but synergistic steps are involved. First of all, the pro-enzyme caspase-1 has to be cleaved through the action of the ASC protein complex. This complex becomes activated by cytoplasmic nucleic acid sensors after severe tissue damage in the

context of invading pathogens[216]. Active caspase-1 is rendered to cleave intracellular pro-IL-1ß that in turn gets released from the cell as a functional cytokine. Expression of pro-IL-1ß is interconnected with NFκB signaling that in turn leads to the sequestration of pro-inflammatory cytokines itself.

Adaptor proteins such as ASC are important in a hosts alertness and danger sensing capacities in the context of tissue damage and resulting pathogen invasion. Wounding is not only accompanied by tissue damage, but also serves as a primary entry point of exogenous pathogens such as bacteria and viruses. The immune system has evolved to cope with this particular situation by employing a series of intracellular proteins and receptors[43].

3.3.6.2 IL-1ß Sequestration and ASC Adaptor Protein Dependency

As shown in **Figure 3.38**, induction and cleavage to form functional IL-1ß was observed for

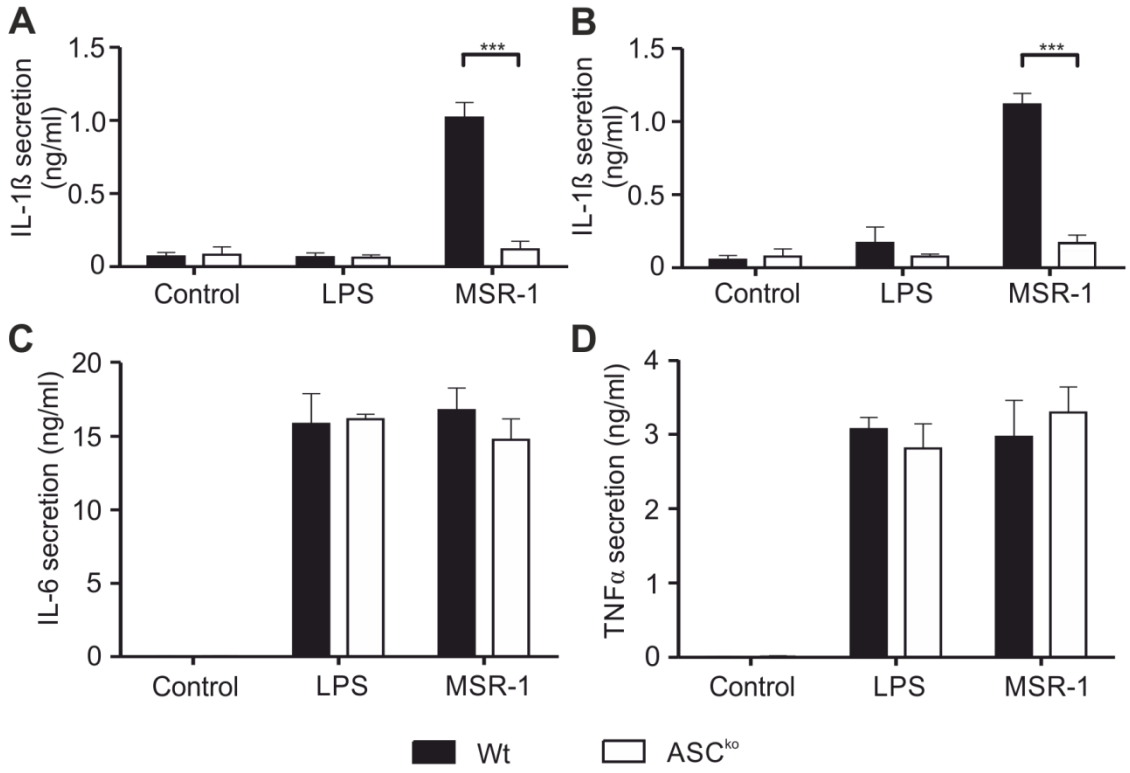

Figure 3.38 Secreted IL-1ß and corresponding IL-6 and TNFα inflammatory cytokine levels of macrophages stimulated with bacterial magnetosome MSR-1 as an indication of the inflammasome pathway. A) IL-1ß sequestration without prior LPS stimulation of cells incubated with MNPs. **B)** IL-1ß secretion after cell-priming with a low dose of LPS prior to MNP labeling procedures. Wt and ASC adapter protein knockout cells were used to demonstrate inflammasome activation dependency. **C)** IL-6 sequestration of cells depicted in A). **D)** TNFα release levels of macrophages treated with bacterial magnetosomes as depicted in A). Boxes display mean values of two independent experiments ± SD.

bacterial magnetosomes MSR-1 after MNP stimulation. Other particles tested did not result in any up-regulation or induction of functional pro-inflammatory cytokines, and thus, are not likely to trigger the induction of the inflammasome pathway. For this reason, detection of released IL-1ß as a direct consequence of the activated inflammasome pathway was only investigated for bacterial magnetosomes.

In order to stimulate TLR signaling and subsequent activation of cytokine release, LPS pre-stimulation using a low-dose for 4 h was employed. However, neither LPS treatment alone nor LPS stimulation with a priming dose of LPS resulted in the release of functional IL-1ß.

On the other hand, MSR-1 MNPs caused a significant amount of active IL-1ß to be sequestered into the culture medium even without priming macrophages with a low dose of LPS prior to particle stimulation overnight (Figure 3.38A+B). Furthermore, MSR-1 displayed induction of the inflammasome in an ASC dependent manner. ASC deficient cells were not able to recruit functional IL-1ß proteins, although levels of pro-inflammatory cytokines remained significantly elevated (Figure 3.38C+D).

3.4 Concept of "Stealth" Particles and their Properties

Usually DCs are well capable of ingesting virtually any foreign compound during their immature phenotypic state[73]. However, in modern medical applications such as diagnostic imaging of vasculature, this effect is undesirable because it reduces systemic half-life of MNP formulations and enhances clearance through the RES system. As a consequence, imaging vectors might not be able to reach and accumulate at the respective imaging target location or remain in circulation for the required imaging time frame.

Therefore, Nitro-DOPA particles functionalized with PEG and biotin were employed that potentially evade uptake mechanisms to prolong their half-life in biological fluids. Particles that fulfill these criteria are often termed "stealth" particles and are being used for both imaging as well as drug delivery systems.

3.4.1 Inflammatory Dendritic Cells (iDCs) in the Context of "Stealth" MNPs

3.4.1.1 Iron Oxide Uptake Properties and Quantification

In order to test how coating materials affect residual uptake of "stealth" particles, two sets of surface coatings for each MNP formulation were employed. Both PEG and biotin are known for their biocompatibility as well as their potential to evade cellular uptake mechanisms.

As displayed in **Figure 3.39**A, the percentage of total cells that successfully integrated MNPs was substantially reduced when compared to MNP formulations previously discussed. Strikingly, a correlation between the percentage of biotinylation as well as a relation to PEG molecular weight was observed. A higher degree of surface biotinylation on MNPs seemed to affect uptake rate in a negative manner. Similarly, a longer chain length of PEG resulted in a lower percentage of cellular uptake. Nitro-DOPA, representing the initial non-functionalized MNP formulation, was taken up the least. Only 8% of the total iDC population yielded successful MNP incorporation.

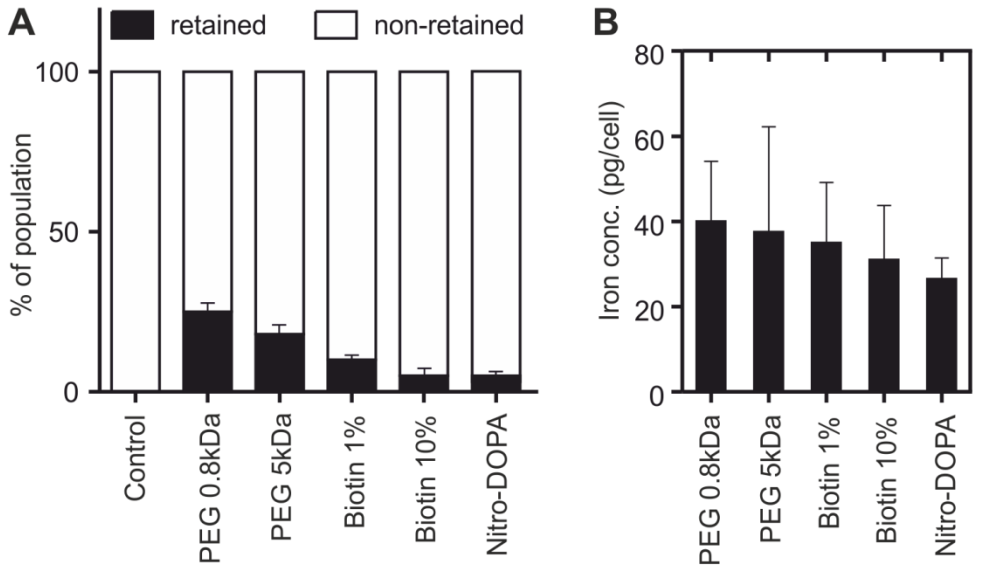

Figure 3.39 Uptake properties of covalently linked „stealth" MNPs into GM-CSF derived iDCs. PEG as well as biotin were functionalized onto Nitro-DOPA base MNP formulations. **A)** Displayed are magnetically retained cell fractions versus unlabeled non-retained ± SD (n=2) after 24 h of incubation. **B)** FerroZine assay determining average iron load per cell in pg. Only positively selected cell fractions depicted in B) normalized against unlabeled counterparts. Depicted are mean values ± SD (n=2).

Intracellular iron levels, however, proved to be within levels already shown for other MNP formulations. On average, 30-60 pg Fe/cell was taken up by immature iDCs (Figure 3.39B). The same trend of magnitude was observed in magnetic separation assays discussed in Figure 3.42A.

Taken together, particles employed indeed provided "stealth" characteristics. Since immature iDC populations represent one of the most phagocytically active cell type, average quantity of uptake proved to be significantly decreased when compared to other MNP formulations employed in this study. Especially Biotin-MNPs conjugated with 10% surface structures evaded cellular uptake mechanisms, with less than 8% of cells being able to incorporate respective MNPs.

3.4.1.2 Phenotypic Cytometry Analysis using iDCs

In order to address surface marker profiles of synthesized "stealth" particles, flow cytometric analyses were performed. iDCs were labeled for 24 h, magnetically sorted and stained for lineage- and DC-specific markers.

Figure 3.29 displays experimental settings used to analyze GM-CSF derived iDC populations. Live cell and doublet exclusion gating were selected prior to antibody gating strategies to exclude cell debris, dying cells or electronic measuring errors. Pre-gating on the DC commitment marker $CD11c^{+}$ ensured that only conventional dendritic cells were analyzed in subsequent cytometric experiments, excluding $CD11c^{-}$ macrophage populations. As exemplified in Figure 3.29B, MHC II^{high}, $CD80^{high}$ and $CD86^{high}$ cell fractions were used to evaluate iDC maturation potential of "stealth" MNPs.

Both PEGylated and biotinylated "stealth" particles proved to be biologically inert and displayed surface marker expression similar to those of untreated controls (**Figure 3.40**). Neither CD80/CD86 nor MHC II surface expression levels appeared to be elevated when compared to LPS positive controls. 24 h of labeling using LPS was employed to provide surface expression profiling of activated iDCs, as outlined in Figure 3.40.

In summary, modification of non-functionalized Nitro-DOPA MNPs using PEG and Biotin moieties did not influence particle immunogenicity. All formulations employed proved to be biologically inert independent of their level of modification and surface decoration characteristics.

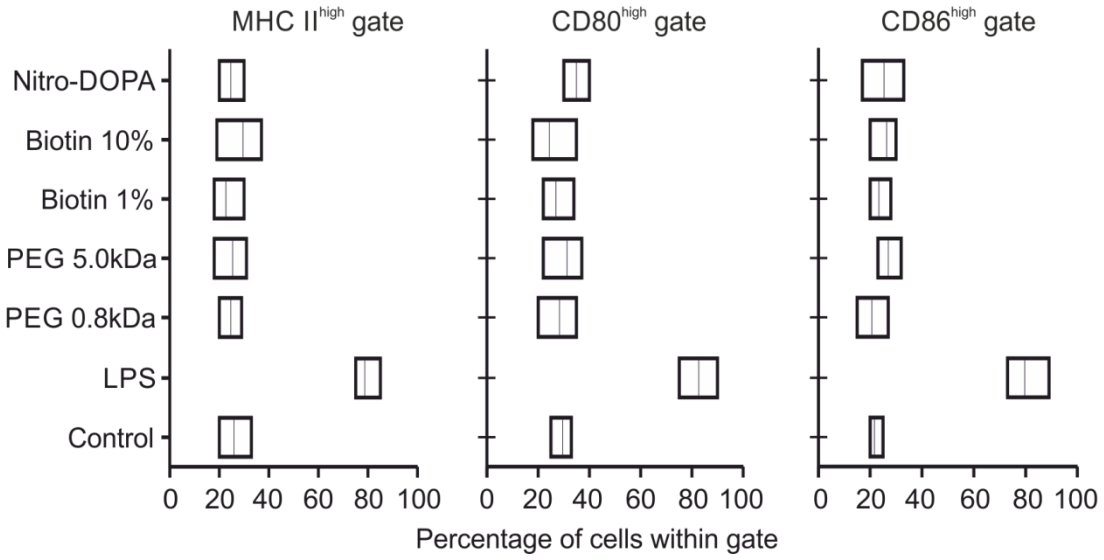

Figure 3.40 Phenotypic FACS profiling of GM-CSF derived iDC populations of covalently linked „stealth" MNPs. Numerical evaluation of gates previously described in Fig. 3.29. Untreated control depicted in lowest column followed by LPS-treated positive control resembling cellular activation. Vertical bars represent mean values ± min/max (boxes) from three independent experiments.

3.4.2 "Stealth" MNP in the Context of Flt3L-Generated DCs

3.4.2.1 Phenotypic Surface Marker Analysis of Flt3L-Generated cDCs

Figure 3.41 depicts numerical evaluation of $CD80^{high}CD86^{high}$ gates as shown in Figure 3.15. As previously seen in similar experiments, "stealth" particles did not trigger an immune response in Wt as well as $TLR4^{ko}$, $TLR9^{ko}$, $MyD88^{ko}$, and ASC^{ko} cells. Levels of surface expression are subject to small variations but remained within normal fluctuation levels.

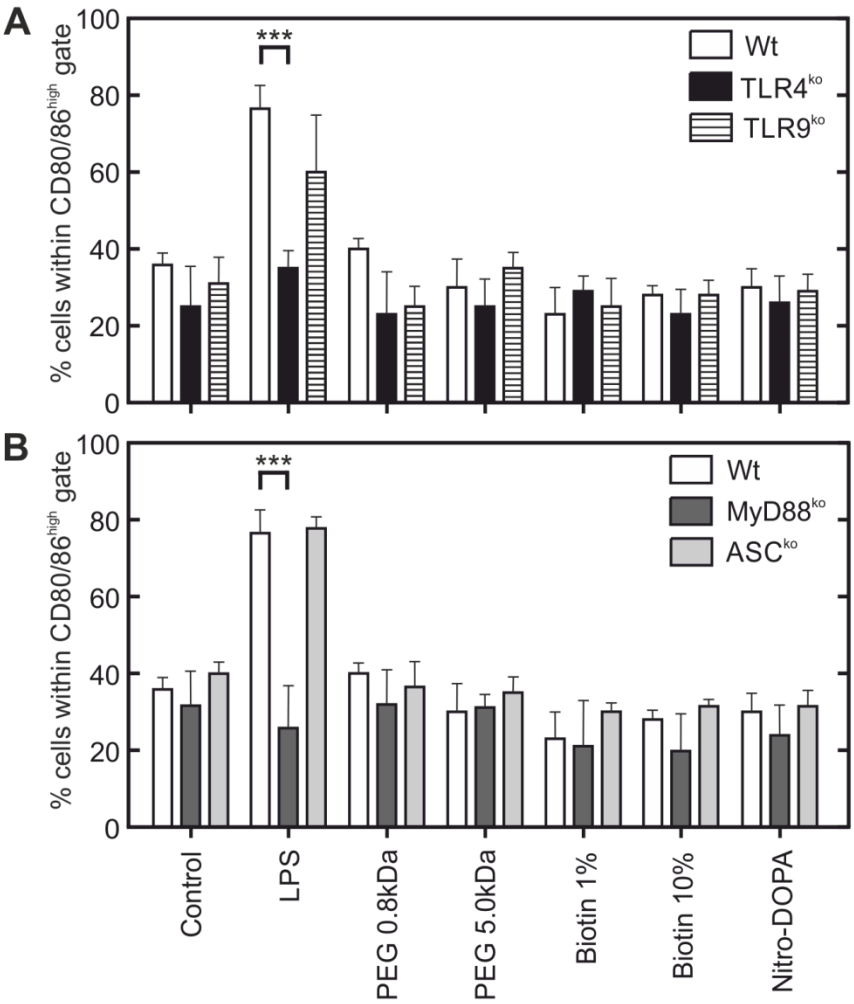

Figure 3.41 FACS profiling of Flt3L generated cDCs in the context of TLR receptor knockout mice. A) Respective populations within CD80/86^{high} gate of Wt, TLR4 and TLR9 receptor knockout cells. **B)** Percentages of populations within pre-defined gates in the context of adaptor protein knockout cells (MyD88 and ASC). Data shown are mean values from two different experiments ± SD.

3.4.2.2 "Stealth" Particles in the Context of Flt3L Derived pDCs

In addition to generating cDCs, driving bone marrow derived progenitor cells into differentiation using Flt3L generates pDCs. These cells induce vast amount of IFNs upon cellular maturation and are critically involved in fighting viral infections, especially in a TLR9 dependent manner.

Figure 3.17 depicts the gating strategy of Flt3L generated pDCs. Cells were selected for further experimental procedures including CD11c^{+}CD11b^{-}PDCA-1^{+}B220^{+} fractions of total live cells as depicted in Figure 3.17B. Levels of surface staining for MHC II and CD86 were evaluated and used for data acquisition and subsequent evaluation. Unstimulated control levels for both MHC II and CD86 gates were undetectable within selected gates. However,

numerical values within selected gates increased to 24% and 16% after cellular activation using LPS, respectively (Figure 3.26B).

Numerical data of MHC II^{high} and CD86^{high} gates are outlined in **Figure 3.42**. Even though pDCs did not yield activation levels of cDCs after LPS stimulation, a significant increase in

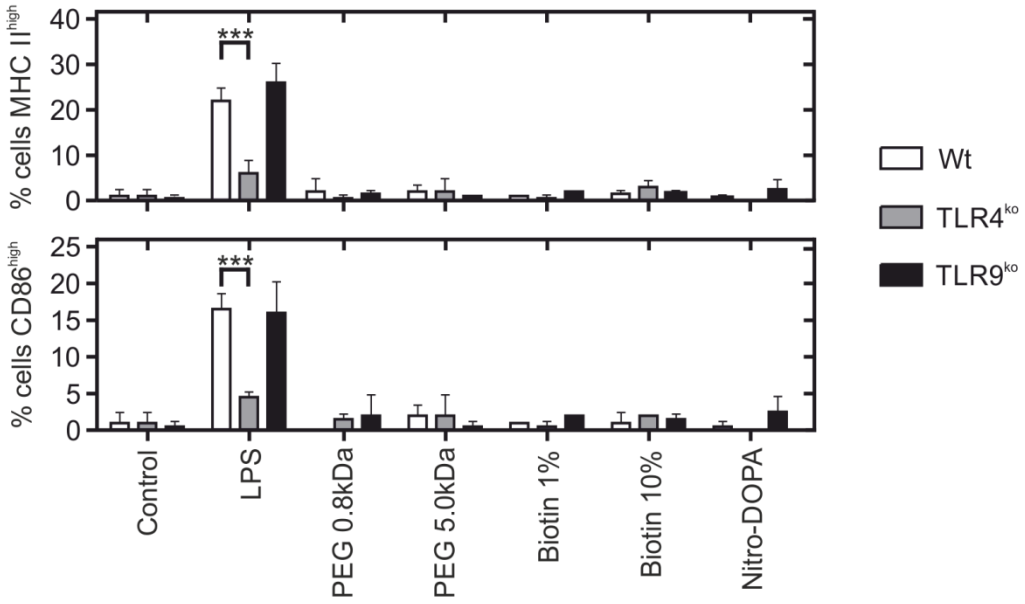

Figure 3.42 FACS profiling of Flt3L generated pDCs in the context of receptor knockout models. Numerical evaluation of data employing gating strategy shown in Figure 3.17 for all „stealth" MNPs employed in the context of TLR4 and TLR9 receptor knockout cells. Shown are mean values of the percentage of cells within respective gates ± SD of two independent experiments for both CD86^{high} and MHC II^{high} regions.

surface marker levels was noted. Values dropped down significantly in case of TLR4 knockout cells. LPS stimulation using TLR9 knockout cells resulted in a pronounced cellular activation comparable to Wt activation. All "stealth" MNP formulations employed, however, did not alter surface expression levels of neither CD86 nor MHC II beyond the control baseline.

3.4.2.3 Cytokine Release of Bulk DCs in the Context of "Stealth" Particles

To further investigate cytokine release of DCs into their surroundings, ELISA experiments were performed. Detection of pro-inflammatory cytokines IL-6, IL-12p40, and TNFα were used to undermine data gathered during cytometric experiments as well as providing evidence as to the type of cellular activation.

In addition to displaying an activated phenotype in FACS scans, DCs highly sequestrated all examined cytokines into their immediate environment upon stimulation with LPS in a TLR4

dependent manner (**Figure 3.43**). However, all "stealth" MNP formulations employed did not result in an increased release of pro-inflammatory cytokines. Protein content did not exceed base-line levels recorded for untreated controls, and thus, further undermined the inertness of particle formulations employed.

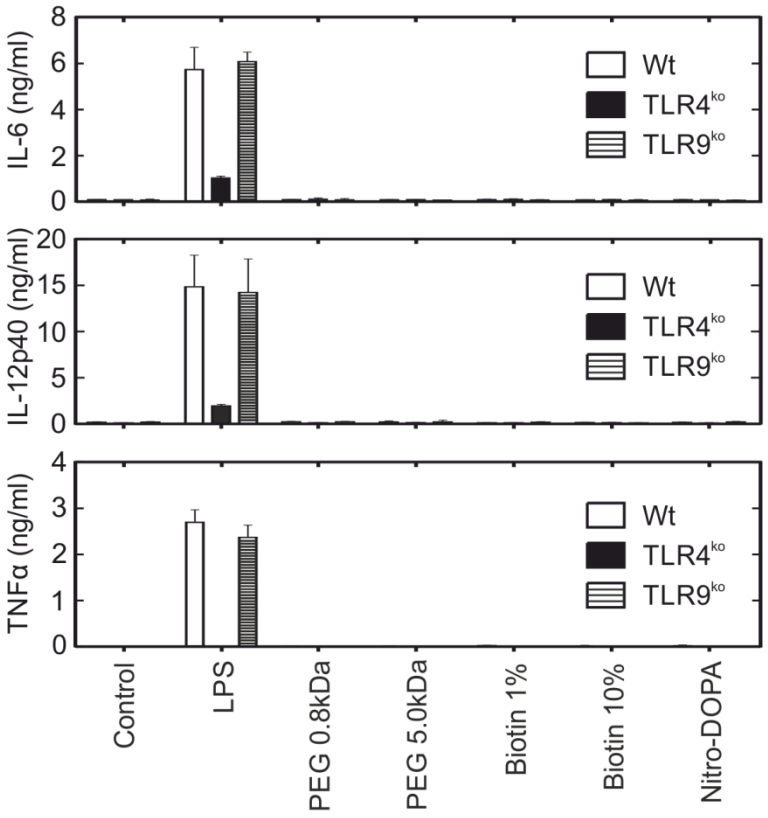

Figure 3.43 Cytokine secretion of „stealth" MNP-stimulated bulk DCs. Cell culture supernatants of stimulated Flt3L generated DCs used in ELISA assays in the context of TLR4 and TLR9 receptor knockout mice. Bars represent mean values of two independent experiments ± SD.

3.4.3 "Stealth" MNP Pulsed Macrophages

3.4.3.1 FACS Profiling of "Stealth" MNP Pulsed Macrophages

Cytometric surface profiling of CD86 and Mac-3 was performed after MNP stimulation of M-CSF generated murine macrophages in both the context of Wt and TLR4 knockout cells. **Figure 3.44** illustrates macrophage FACS profiles obtained after 24 h of incubation with respective "stealth" MNPs. The gating strategy employed is illustrated in Figure 3.20.

LPS yielded a significant up-regulation of both CD86 and Mac-3 surface proteins when compared to control levels. However, elevated presence of the respective molecules dropped down significantly in case of TLR4 receptor knockout cells. Neither Mac-3 nor CD86 levels

appeared to be elevated after exposure of macrophages to PEG and biotin MNP formulations, again substantiating the inertness of particles in the context of murine macrophages.

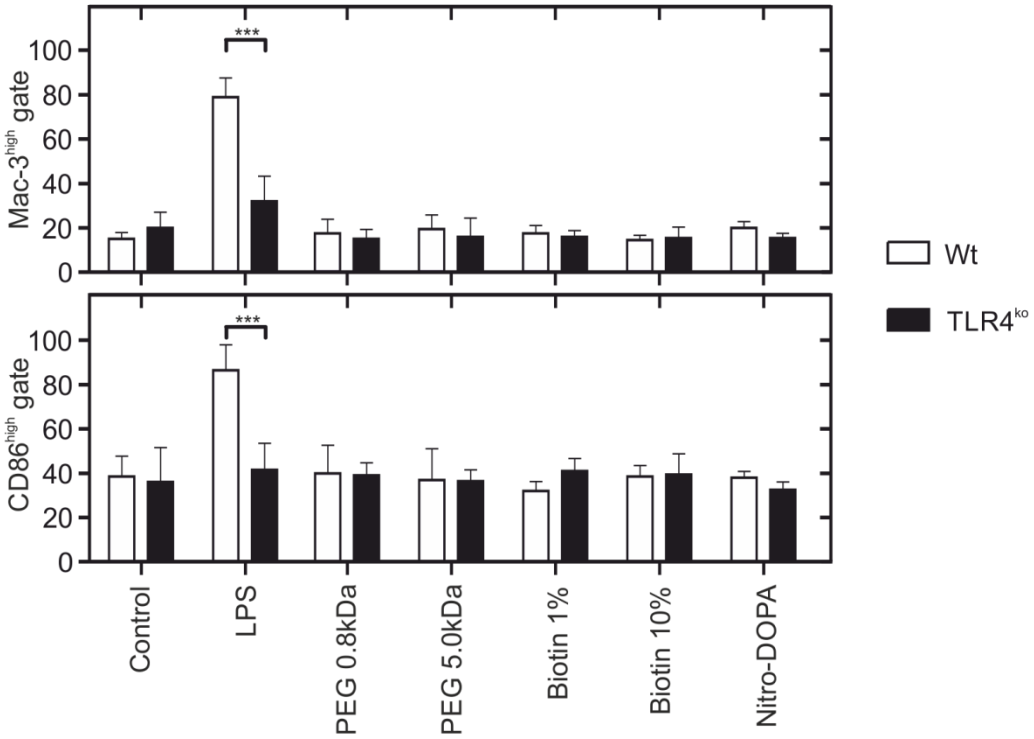

Figure 3.44 FACS profiling of „stealth" MNP-pulsed macrophages in the context of TLR4 receptor knockout cells. Numerical evaluation of example data shown in Figure 3.20 for all MNPs employed in the context of TLR4 knockout cells. Shown are mean values of the percentage of cells within respective gates ± SD of three independent experiments.

3.4.3.2 ELISA Cytokine Secretion of M-CSF Generated Murine Macrophages

In order to test the biological response of differentiated macrophages to "stealth" particle exposure, cytokine measurements were performed. Levels of IL-6, IL-12p40 and TNFα sequestration were investigated after 24 h of MNP exposure to adherently growing immature cells.

As illustrated in **Figure 3.45**, "stealth" MNPs display neglectable levels of protein release as do untreated control macrophages. LPS resulted in the release of all three tested cytokines in a TLR4 dependent manner.

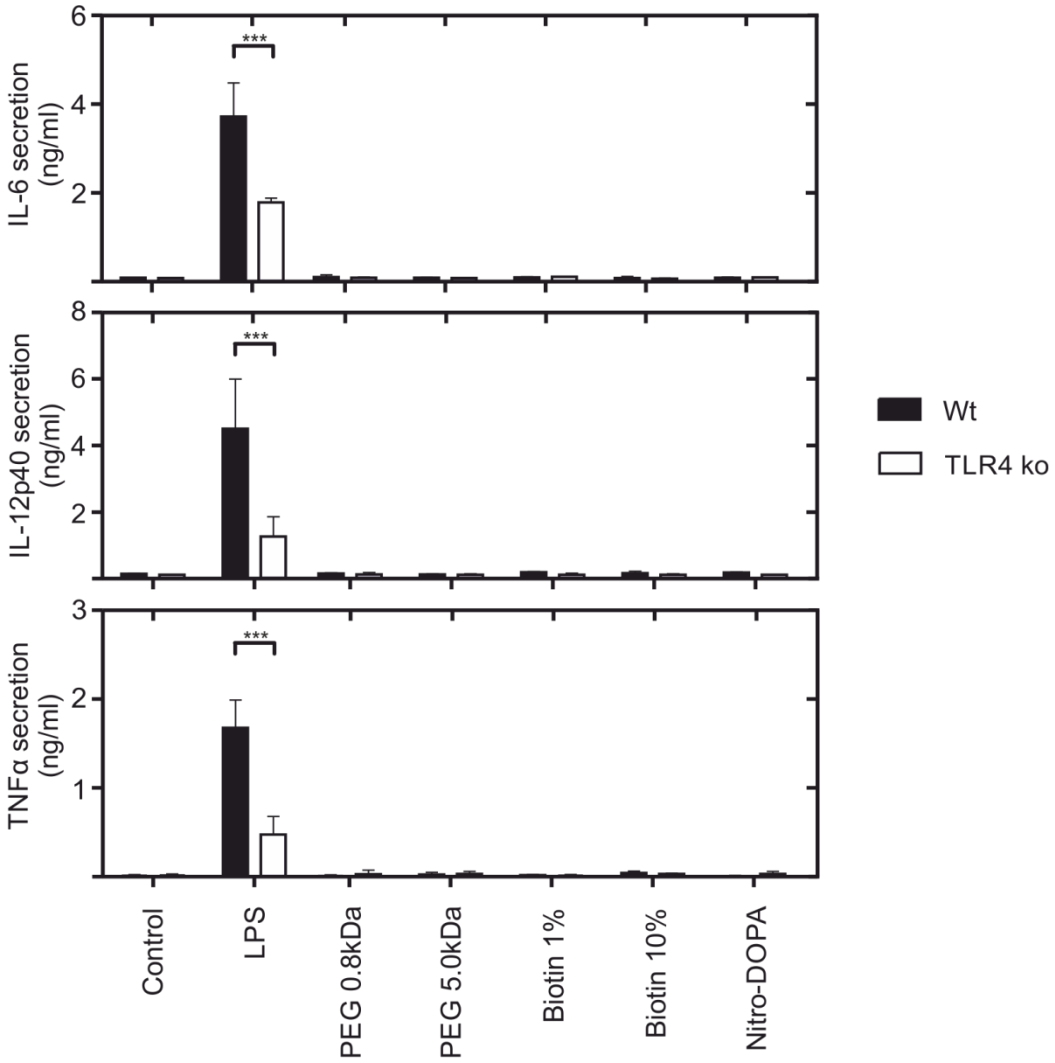

Figure 3.45 Cytokine secretion of MNP-pulsed macrophages in the context of receptor knockout mice. IL-6, IL-12p40, TNFα cytokine secretion levels in both the presence and absence of TLR4 receptors. Cells were incubated for 24 h in the presence of the respective MNP and supernatants collected afterwards for further ELISA analyses. Boxes display mean values of two independent experiments ± SD.

3.4.4 Splenocyte Responses to "Stealth" MNPs

In order to test the immunological impact on bulk splenocyte cultures, explanted organs were dissociated and single cell suspensions labeled with respective "stealth" MNPs for 72 h under the influence of CFSE dye. This allows a fluorescent tracking of successive cellular division events that provides information about the potential of MNPs to induce T cell proliferation within the explanted splenocyte population.

As illustrated in **Figure 3.46**, only LPS treatment resulted in the decrease of CFSE signal. "Stealth" MNPs did not induce cell proliferation of explanted bulk splenocyte populations

(Figure 3.46B) and total cell numbers remained within untreated control levels (Figure 3.46A).

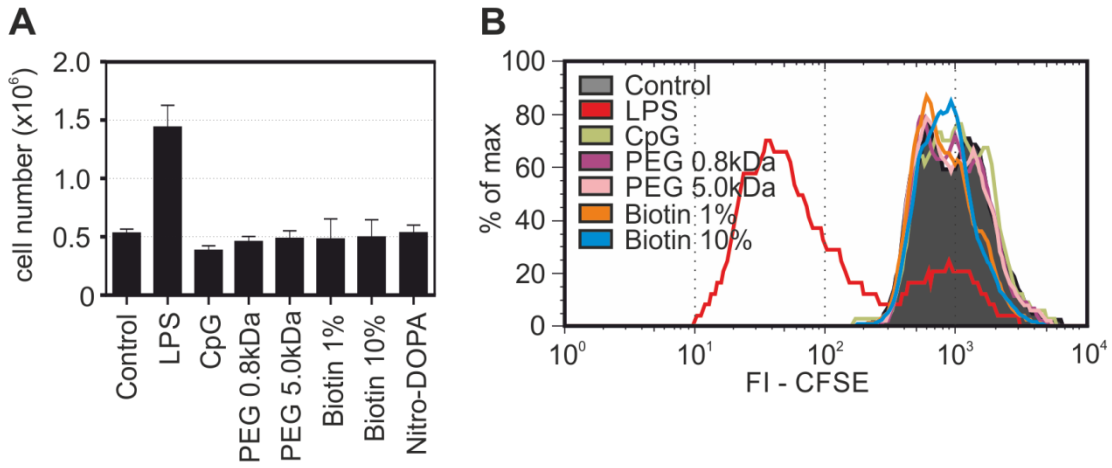

Figure 3.46 Mixed splenocyte reactions to evaluate T-cell proliferation capacity of „stealth" MNPs employed. A) Total number of cells after 72 h of incubation resulting from potential T-cell proliferation events. Shown are mean values ± SD of two independent experiments (n=2). **B)** Histograms of CFSE intensity as a function of T-cell proliferation after 72 h of incubation with both MNPs and the dye. Shown is one representative experiment (n=2).

3.5 Influence of Serum Components on MNP-iDC Interactions

Recently, it has been demonstrated that proteins present in biological fluids such as i.e. blood serum or cell culture additives impact on MNP properties[155]. Especially charged MNPs adhere to opposingly charged proteins and are immediately covered by a film of biomolecules that alter their designed chemical MNP properties. This additional adherent soft protein shell ultimately changes particle-cell interactions such as recognition, mechanisms of endocytosis and clearance that strongly depend upon the nature of this protein "soft-shell" formed in aqueous solutions.

Therefore, investigations regarding uptake and resulting imaging properties of MNPs in either the presence or absence of serum proteins were performed.

3.5.1 Serum-Dependent Uptake Kinetics of MNPs

Time course experiments were carried out to investigate uptake kinetics of MNPs. Since the apparent differences in uptake seemed to be present shortly after MNP exposure to protein content, time intervals were chosen between 1 min and 6 h. After that time period, levels of

uptake appeared to normalize when comparing serum-free and serum-containing MNP-labeling environments (data not shown).

As illustrated in **Figure 3.47**, positively charged particles such as PEI-MNP were taken up to a significantly higher degree in the absence of serum proteins. Almost 80% of PEI-MNP particles were taken up into the cells within the first few minutes of exposure, after which the amount taken up only increased marginally (20%). In serum-containing culture conditions, however, only 50% of PEI-MNP was taken up into cells after 1 min.

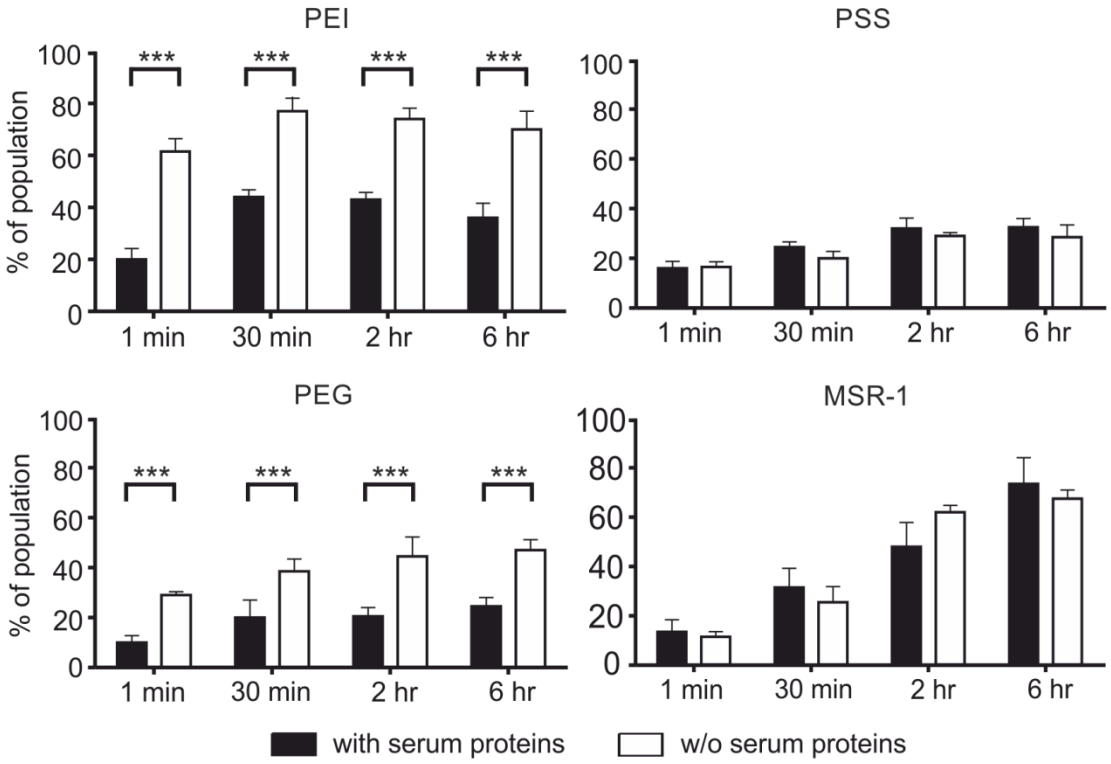

Figure 3.47 Influence of serum protein content on uptake properties of various MNPs into iDCs. Magnetic separation data of various MNP formulations in both the presence and absence of serum proteins. Charged poly-electrolyte MNPs, PEGylated „stealth" particles and bacterial MSR-1 magnetosomes were employed to assess the influence on soluble molecules on MNP-cell interactions. Time course experiments show MNP uptake after 1 min or up to 60 min of incubation time. Bars display mean values of three independent experiments ± SD. *** $R < 0.001$.

The impact seemed to be abolished when dealing with negatively charged particles such as PSS-MNP, which was gradually taken up by iDCs. No difference was observed when comparing serum-free with serum-containing culture conditions. Surprisingly, PEG-coated MNPs also displayed both time- and serum-dependent differences in uptake properties. On the other hand, bacterial MSR-1 MNP did not show a significant difference when altering soluble protein concentration in culture medium. However, bacterial MSR-1 MNP was gradually taken up, with the maximum amount reached after 6 h. No further uptake was recorded beyond this time.

3.5.2 Serum-Dependency of Intracellular Iron Concentration

It has been known for a long time that exogenous pathogens or compounds are being opsonized through various mechanisms such as antibody or complement binding to facilitate uptake into cells[23]. However, charged surfaces interact with ions and proteins in solution that loosely bind to particles through adhesive forces[217]. This could potentially implicate a masking of cellular target structures on MNPs, or, facilitate initial binding to structures of the plasma membrane that enhance subsequent uptake.

To investigate these parameters, analyses to test whether the presence of serum constituents has an influence on MNP uptake quantity, namely intracellular iron content within labeled cells, were performed. As depicted in **Figure 3.48**, almost all MNPs tested were taken up to a higher degree without serum proteins present. However, PSS-MNP, a negatively charged particle, was taken up to the same degree in both experimental conditions. On the other hand, nearly twice the amount of iron was incorporated in the case of the bacterial magnetosome MSR-1.

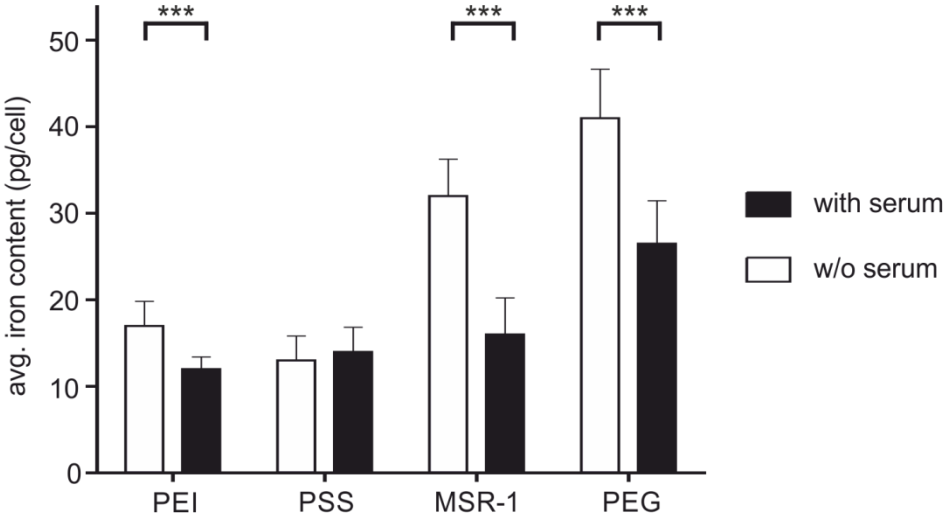

Figure 3.48 Influence of serum proteins on intracellular iron concentration of various MNPs in iDCs. FerroZine assay displaying the average amount of iron taken up per cell in magnetically separated cell fractions. Bars display mean values of three independent experiments with error bars ± SD. *** $R < 0.001$.

3.5.3 Impact of Protein "Corona" on MR Imaging Properties

It can be envisioned that particle opsonization or adhesive protein layers shielding reactive surface moieties of MNP shell structures ultimately change packaging properties inside target

cells. In turn, altered intracellular particle density or agglomeration patterns could potentially change molecular imaging characteristics of contrast agents being employed.

To investigate the impact of serum components on MNP imaging properties using MRI, *in vitro* phantom experiments were performed on successfully labeled iDCs. As shown in **Figure 3.49**, no significant differences were observed in signal reduction patterns when comparing target cell populations labeled under either serum-free or serum-containing conditions. All particles displayed the same magnitude of relaxation rate and detection limits under the two given experimental labeling conditions.

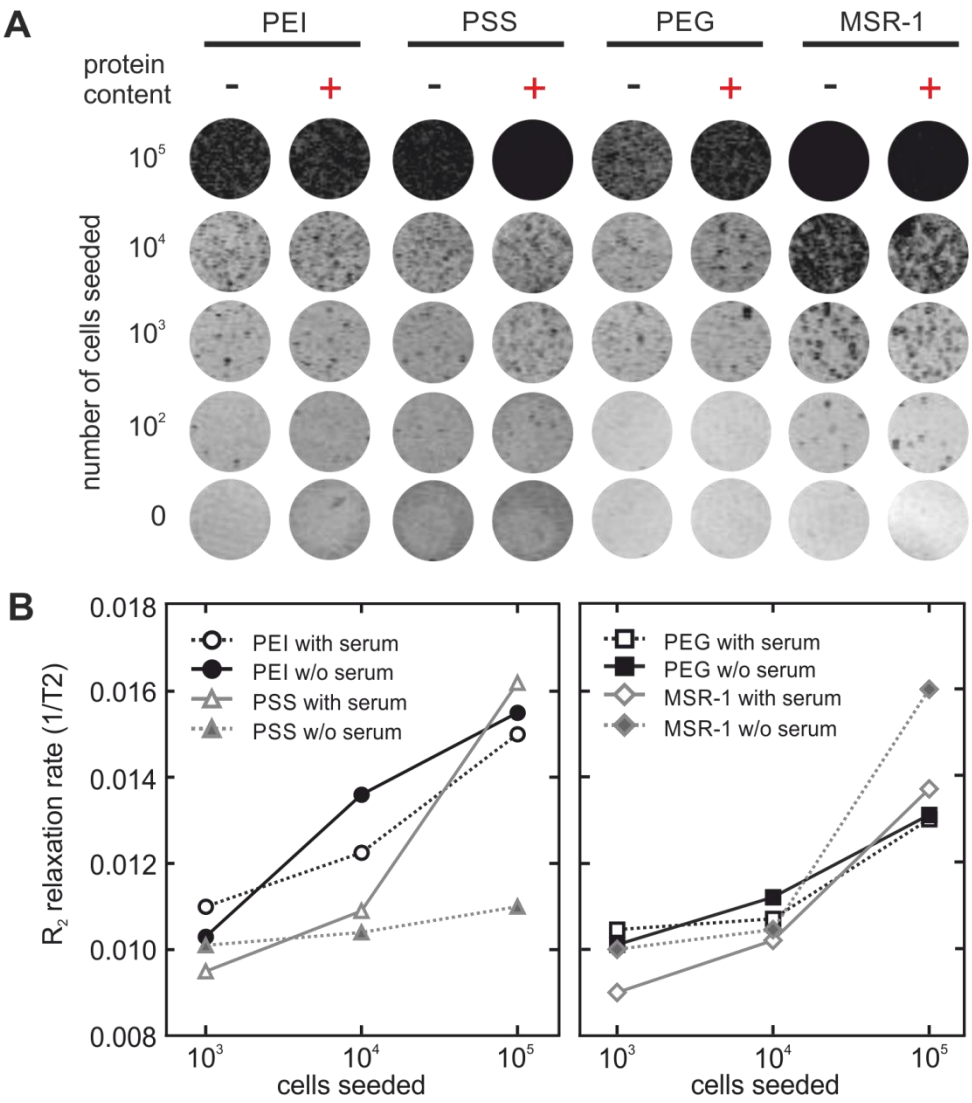

Figure 3.49 Influence of serum proteins on MRI properties of various MNP formulations within inflammatory iDCs. A) 3D image stacks of regions of interest (ROIs) including DCs labeled with MNPs that have been cultured under serum-containing and serum-free conditions. **B)** Numerical evaluation of MRI phantom data from one representative experiments (n=2) depicted in A).

However, the linear relationship between relaxation rate R2 and cell seeding density appeared to be improved when imaging cells labeled under serum-free conditions. In particular, MSR-1 R2 data showed substantial loss of linearity under protein-rich environments, whereas linearity was retained in the absence of serum components.

3.6 Concept of Functionalized Acryl-MNPs

Functionalization of particle surface structures represents a valuable research tool to enhance or guide performance and induction potential of MNPs regarding a defined target cell population[177]. Molecular moieties such as CpG motifs can be implemented on particle surfaces to drive immune cells towards a specific immunological phenotype that could potentially enhance (i) a desired treatment outcome and (ii) MR imaging properties.

Nitro-DOPA MNPs coupled to acrylated functional groups were investigated as to their potential to covalently bind functional groups to their outermost anchor moieties. In this study, the possibility to enhance immunological capacity of MNP formulations by chemically ligating CpG motifs to their terminal structures to stimulate immature DCs, in particular pDCs, was investigated. Especially pDCs are known for their potential to become activated and release vast amount of type 1 interferons upon viral encounters, and thus, enhancement of cellular activation while lowering amounts of CpG needed was investigated.

3.6.1 FACS Data of pDCs and Bulk Supernatant ELISA

To validate successful MNP coupling strategies for CpG motifs onto target acrylated MNPs, a series of experimental measures were conducted. CpGs represent DNA analogues of viral origin and are recognized via endosomal TLR9 molecules within DCs. TLR9 is known to signal exclusively through the adaptor protein MyD88, and thus, cells deficient of this protein were included as controls in these experiments.

In order to provide evidence as to coupling efficiency, magnetic purification steps were performed to exclude unbound CpGs within coupled MNP solutions that potentially trigger DC maturation without being coupled to designated target structures. As outlined in **Figure 3.50**A+B, target CpGs alone, acrylated control MNPs without CpG ligation (acMNP),

purified CpG-coupled MNPs (after 1st, 2nd purification), and resulting acrylated CpG-MNPs (after 3rd purification) were employed.

Bulk Flt3L generated DCs were subjected to particle formulations acquired during CpG coupling steps and tested for their potential to induce cellular maturation events leading to the up-regulation of surface co-stimulatory molecules, namely CD80 and CD86 (outlined in Figure 3.50A).

As shown in Figure 3.50B, positive controls using LPS showed significant up-regulation of both surface markers in Wt and TLR9$^{-/-}$ cells. Stimulation with CpG motifs alone resulted in a pronounced increase in the abundance of CD80/86 surface proteins; however, this effect was

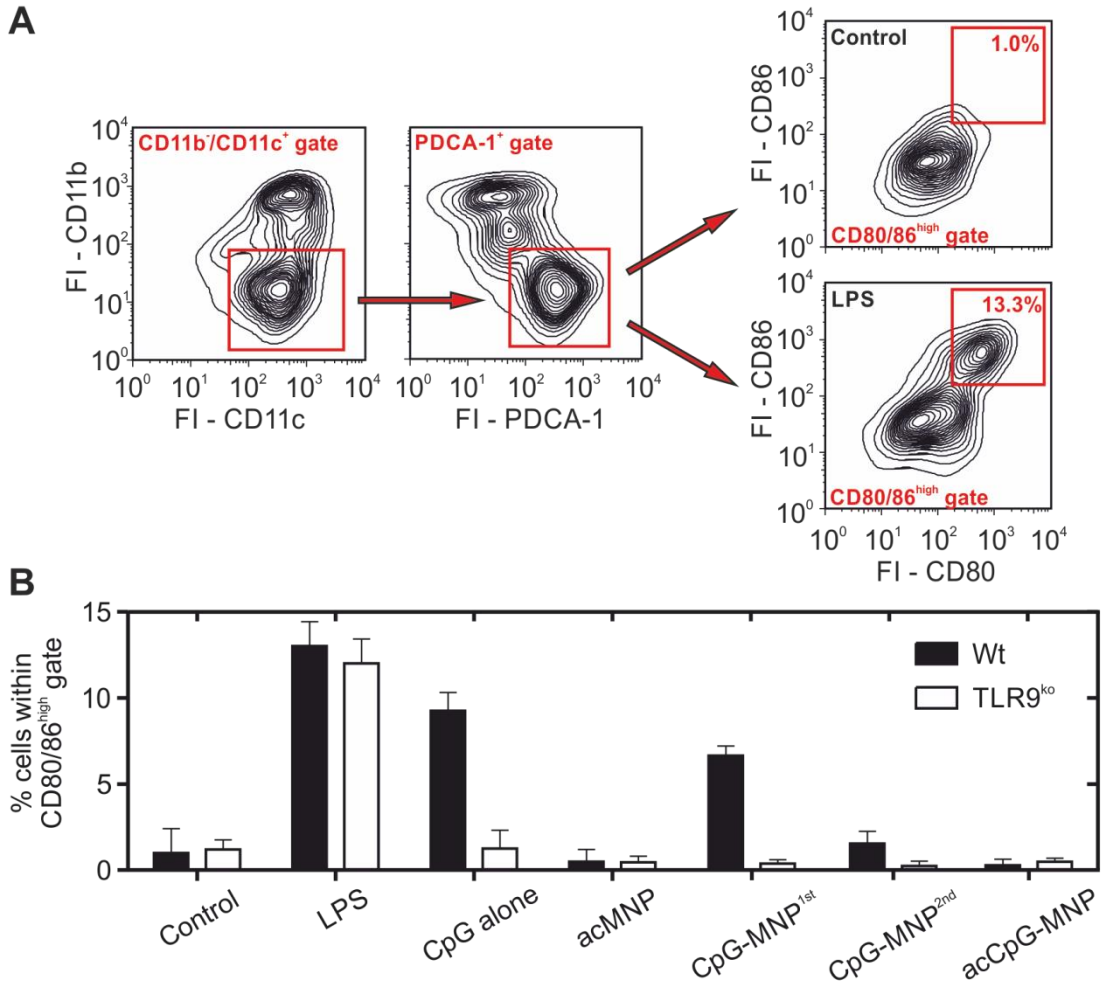

Figure 3.50 Concept of functionalized acrylated MNPs (acMNP) using CpG motifs linked to MNP surface moieties. A) FACS gating strategy of Flt3L generated pDCs. **B)** Acquired data displaying pDC activation potential of CpG functionalized MNPs and their wash fraction in the context of Wt and TLR9 knockout cells. CpG moieties were linked to acrylated MNP formulations and magnetically separated to withdraw unbound molecules. Corresponding wash fractions represent unbound, MNP-free supernatant. Displayed are mean values of two independent experiments ± SD.

abolished in knockout cells. Acrylated MNP alone without coupling of target moieties did not

result in surface marker up-regulation beyond untreated control levels, providing evidence as to the inertness of the base particle formulation.

Purified CpG-coupled MNPs (after 1st, 2nd purification) displayed activation of pDC Wt populations to some extent; however, the effect seemed to be diminishing with increasing numbers of purification steps. Unfortunately, the resulting acrylated CpG-MNPs (after 3rd purification) lost all capacity to induce cellular maturation of bulk DC cultures, in particular pDC populations.

3.6.2 ELISA Cytokine Secretion of Flt3L-Generated Bulk DCs

In order to validate findings acquired with cytometry, supernatants of CpG-coupled MNPs were collected and subjected to ELISA. As outlined in **Figure 3.51**, pro-inflammatory cytokine levels of IL-6, IL-12p40, and TNFα of Wt cells were measured.

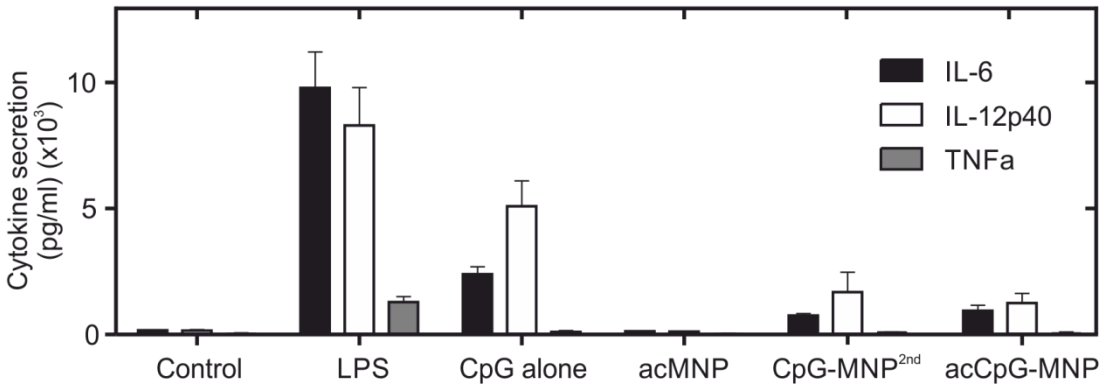

Figure 3.51 Cytokine secretion of functionalized acMNPs using CpG motifs linked to MNP surface moieties. ELISA data of Flt3L generated bulk DC cultures. Pro-inflammatory cytokines IL-6, IL-12p40, and TNFα were measured after 24 h of treatment. Displayed are mean values of two independent experiments ± SD.

LPS controls induced a dramatic increase of sequestered pro-inflammatory cytokines compared to untreated control baseline levels. Stimulation with CpG motifs alone induced the release of IL-12p40 and to some extent IL-6, whereas no TNFα was detected. Protein levels within supernatants collected of non-ligated acrylated particles (acMNP) displayed no elevation of released cytokines and levels were identical to untreated control samples.

However, purified CpG-MNPs (after 2nd purification and final acCpG-MNP) showed elevated levels of both IL-6 and IL-12p40, although only to a minor extent when compared to positive controls such as LPS and CpG motifs.

In summary, both cytometric and ELISA measurements revealed that non-ligated acrylated particles (acMNP) possess no immunogenicity. However, after the ligation of CpG motifs to the outermost layers of the particle shell through covalent binding strategies, no significant TLR9 dependent maturation of DCs remained after particle purification measures.

4 Discussion

In the present study, an investigation of different MNP formulations was performed to assess the interaction and uptake phenomena that ultimately shape molecular imaging characteristics. It has been well established that exogenous particles are internalized by cell types of different origins and developmental stages after systemic and *ex vivo* MNP application[174,218,219,220]. In combination with their inherent biocompatibility and chemical stability, this finding has been the basis for employing iron-oxide based MNPs in molecular imaging and drug delivery regimes using MRI[23,29,221]. However, systematic studies addressing surface decoration and subsequent cellular consequences are still lacking and underlying mechanisms are poorly understood. Shaping particle surface moieties to confer a specific immunological and imaging goal remains to be a research area of great interest for future diagnostic and therapeutic applications[222,223].

For this reason, an experimental platform was generated in this study that allowed the investigation of interaction, uptake and resulting imaging characteristics involving synthetically engineered and biogenic nanoparticles in the context of cellular targets. It can be envisioned that functionalized surface moieties of MNPs impact on initial particle recognition, thus dictating routes of endocytosis and thereby influencing subsequent intracellular processing. Furthermore, these parameters ultimately shape resulting MRI properties. To achieve this functionalization, a wide range of surface moieties on MNPs were generated.

LbL technology provides the means to actively shape particle attributes such as charge, overall size, and shell chemistry by employing charged poly-electrolytes as coating substrates[162,224,225,226].Using this versatile technological platform, particle properties can be engineered depending upon the experimental goal. Furthermore, LbL provides a means to engraft biologically active macromolecules into MNP shells for further functionalization[227,228,229]. Poly-electrolyte coating of MNPs can be conceived to endow particle surfaces with desired properties resulting in (i) enhanced or even targeted uptake into cells, thereby augmenting MRI performance and (ii) providing additional functionalities such as immune-regulatory activities[230].

PEG and biotin are particularly suitable contrast agents for MRI due to their inherent property of evading systemic clearance, and thus, prolong circulation times[167,231]. To test how coating density affects cellular interactions, MNPs functionalized with PEG and biotin moieties

provided additional MNP platforms to further investigate the impact on biological target populations. For this purpose, a novel Nitro-DOPA anchoring group was employed to covalently attach surface moieties onto existing molecular MNP structures[169]. In addition, an attempt was pursued to further functionalize covalently modified acrylated MNPs with immunologically competent CpG antigenic structures that are known to confer TLR9 dependent immunological consequences, especially in pDCs.

Bacterial magnetosomes represent a class of biogenic nanoparticles that open the perspective to further amplify functionalization strategies through employing genetic engineering. Using this tactic, Scheffel et al. were recently able to fuse eGFP to the *mamJ* gene product of *M. gryphiswaldense*, thereby creating bimodal magnetosome imaging probes[232].

4.1 Chemical Stability and Biocompatibility of MNP Formulations

Design criteria of MNPs employed in biomedical applications include both the acquisition of particle (i) stability as well as (ii) biocompatibility. Particle stability is conferred by layer(s) of substrates around the magnetic core of iron oxide particles[233]. Surface moieties usually grant particle monodispersity through charged molecules that drive MNP repulsion, thus leading to a homogenous distribution within solvents that inhibit undesirable agglomeration effects[234]. Furthermore, complete shielding of iron core structures conveys particle stability. It has been shown that incomplete coating strategies lead to premature particle degradation and severely decreased half-lives. Naked core particles tend to be highly chemically active and are prone to oxidation, leading to loss of magnetic properties and dispersibility[235].

Therefore, particles synthesized for the purpose of this study were analyzed using Zeta Sizing and Dynamic Light Scattering (DLS) technologies. As has been shown in several independent studies, these two techniques are successfully employed to verify particle properties such as overall hydrodynamic size and surface potential (Table 3.2)[188,189]. All MNPs tested resulted in a narrow size range and surface charge potential proving their stability and monodispersity. The only exception was Chit and Dex-MNP, whose parameters could not be determined successfully. This finding can be attributed to incomplete surface functionalization during synthesis procedures, thereby compromising particle stability and integrity. Due to the fact that multiple species ranging in size and surface potential were recorded, particle agglomeration most likely occurred in aqueous solution. However, due to the approved biocompatibility of both dextran and chitosan poly-saccharides, particles were included in this

study. Skebo et al. have shown that indeed incomplete surface modification leads to compromised integrity of MNP formulations[236]. On the other hand, however, all other poly-electrolyte, lipid-shell and covalently functionalized MNPs employed herein proved to be chemically stable by presenting discrete sizes and surface potentials.

However, even though biocompatibility of nano-scaled objects has been a focus of extensive research recently[218,237], there is a need to constantly monitor and ensure the lack of potentially arising adverse effects on exposed biological systems, particularly in medical imaging regimes. Especially biomaterials used in medical implants and the growing number of nano-scaled particles employed in both medicine and industry pose a potential threat to biological systems[154].

In general, cellular cytotoxicity of MNPs in both experimental and clinical environments can be separated into two broad categories: Uptake-independent and uptake-dependent mechanisms. According to Soehnen et al., uptake-independent cytotoxic effects are exerted whenever large quantities of nanoparticle solutions are present without any cellular uptake mechanisms being involved[196]. Particle degradation products, excessive amount of MNPs within the cell's immediate environment, and nutrient displacement potentially lead to adverse cellular viability effects[238]. Uptake-dependent cytotoxic effects on the other hand can be linked directly to MNP formulations being taken up by target cells. They arise as a consequence of reactive oxygen species (ROS) formation, the destruction of cellular compartments by chemical or mechanical forces, as well as ultimately leading to the induction of apoptosis[154,239].

In order to test these parameters on target cells, biocompatibility screenings were performed including both colorimetric MTT-based experimental procedures as well as 7-AAD fluorimetric cytometry approaches. While MTT results provided information about the resulting adverse effects on bulk populations including both uptake-dependent and uptake-independent effects, 7-AAD data only considered successfully labeled target cells after magnetic separation procedures. However, with all cell types investigated, no significant adverse effects on cell populations were observed even when increasing iron oxide labeling concentrations by a factor of 20. It is worthwhile noting that both Chit and Dex-MNP resulted in elevated rates of cell death in HSCs when compared to terminally differentiated DCs (Figures 3.1+3.7). This finding can most likely be attributed to the endocytic capabilities of DCs being present as an integral biological asset of professional antigen scavenging cells[116]. On the other hand, HSC and their immediate downstream progenitors are not exposed to

exogenous antigens within their primary localization, and therefore, do not require endocytic properties. They are confined and shielded within their biological "niche", whereas DCs reside in environments potentially encountering danger signals. As previously discussed, however, cytotoxicity observed with the cells types employed and particle formulations used is in agreement with previous studies employing similar MNPs and cell types. Under comparable experimental conditions, Soenen et al. have shown that iron oxide MNPs are usually well tolerated by progenitor cells up to a concentration of several mg/ml of iron content[240]. Terminally differentiated cells such as DCs and macrophages are capable of tolerating an even higher amount of iron oxide based nanoparticles.

4.2 Uptake Properties and Intracellular Iron Deposition

Uptake properties of MNPs into a given target cell population not only provide information about the efficiency of designed particle surface moieties, but in addition insights into molecular imaging characteristics[241]. Labeled cells are endowed with magnetic properties allowing a separation of fractions according to their MNP engulfment status. This separation technique was employed to allow both a quantitative as well as a qualitative assessment of the efficiency of MNPs taken up by target immune cells of various developmental and lineage origins.

In this study, undifferentiated HSCs labeled with magnetic nanoparticles did not show a prominent uptake that can be attributed to their developmental stage and biological function. Previous studies using stem and progenitor cells showed similar results regarding labeling efficiencies employing iron oxide based nanoparticles[33,242]. Interestingly, we herein report an elevated uptake (2-fold) of bacterial magnetosomes into $Flt3^+$ hematopoietic stem cells when compared to synthetic LbL poly-electrolyte and lipid-shell MNPs. This observation can be linked to the expression repertoire of PAMP recognition receptors on these stem cells and their immediate progenitors allowing them to respond to potential environmental threats[243].

However, due to the need for HSC labeling options in cell-based biomedical applications, especially charged poly-electrolyte MNPs such as PDAD-MNP and PEI-MNP proved to be taken up by a fairly large amount of target cells (Figure 3.2A). As shown by Weissleder et al. and others, this is due to the positively charged surface properties of these two contrast agents that allows electrostatic adherence to the negatively charged membrane structures of cells, and thus, facilitates endocytic uptake[244,245]. In contrast to professional phagocytes, intracellular

amount of iron oxide MNPs remained low but in agreement with labeling studies performed using different progenitor cell types (Figure 3.2B)[202].

Due to their biological function as professional phagocytic cells, immature DCs are capable of ingesting large amounts of MNPs. Charged poly-electrolytes and lipid-shell MNPs were taken up by the majority of cells, with more than 70% of exposed target populations being labeled after 24 h (Figure 3.8A). Again, electrostatic attractive and repulsive forces lead to the formation of so-called "protein corona" effects, opsonizing particle surface moieties and increasing subsequent MNP uptake[155,159].

Successful labeling of target cell populations such as i.e. DCs with contrast agents prior to implantation provides a means to non-invasively monitor cell fate using MRI. Therefore, efficient uptake of contrast agents by DCs allows detection of cell deposition and migration as previously reported by us and other groups[171,246,247,248].

Protein adsorbance and opsonization effects represent another area of intense research. In medical applications, chemical changes in the nature of a particular contrast agent or drug delivery system pose a great threat to the functionality of the delivered probe[155]. Therefore, scientists are eager to optimize coating strategies to minimize opsonization effects potentially resulting in enhanced clearance mechanisms through the immune and RES system as well as increasing therapeutic potential and overall stability of MNP formulations employed[249].

Covalently linked "stealth" particles employed in this study displayed significantly reduced uptake properties when compared to poly-electrolyte and lipid-shell MNPs (Figure 3.39). PEG and Biotin are well known to exert these characteristics and therefore represent suitable coating materials for certain biomedical imaging applications that convey increased circulation half-life[249,250]. Particle formulations coated with PEG and biotin were not taken up by cells to a high degree. Interestingly, cellular uptake was further diminished when increasing amount of MNP surface functionalization as shown employing covalently-linked biotinylated and PEGylated MNPs. Endowing particle formulations with similar "stealth" effects represents an area of intense research to further optimize imaging potential of nanoscaled vectors[251].

Especially charged particle surfaces are prone to be electrostatically covered by opposingly charged proteins leading to the formation of a secondary soft shell of various molecules in solution[159,252]. Ultimately, MNP interaction processes and subsequent uptake mechanisms are subject to change depending on the nature and magnitude of this particle sheathing.

As shown in this study, in particular positively charged MNP uptake characteristics are changed in that regard. During time-course experiments, PEI-MNP displayed significant alteration of uptake depending on the presence or absence of serum proteins. Maximum cellular uptake was reached after very short incubation times (below 30 min), after which no further increase was detected (Figure 3.47). However, even though uptake was dramatically increased when stimulating target cells with MNP in the absence of serum proteins, overall uptake kinetics remained unaltered for both experimental conditions. This finding provides evidence that particle uptake is enhanced due to charge-dependent adhesive forces exerted by the positively charged outer-most MNP layers. In several independent studies, it was shown that reactive serum components such as albumin and immunoglobulins have a high binding affinity to exogenously introduced matter such as MNPs[159,253]. Keeping these experimental outcomes in mind, it can be envisioned that opsonizing effects occurring in biological fluids change distinct parameters vital for successful imaging or even drug delivery systems. Cho et al. argue that these changes in chemical behavior of medical probes being administered to patients for the course of imaging or treatment could potentially alter the course of the desired MNP behavior[254]. However, no significant differences in MRI properties were noted when comparing protein-rich labeling environments with protein-low cell culturing conditions in this study (Figure 3.49).

Furthermore, the bacterial magnetosome MSR-1 was taken up to a fairly high extent by iDCs. On average, 75% of cells incorporated bacterial MNPs resulting in the highest uptake of particles in these studies (Figure 3.28). This finding can be attributed to the immunogenicity of magnetosomes, resulting in phagocytic burst and enhanced uptake into target DCs in the course of cellular activation. The immature “surveillance” phenotype of DCs confers enhanced endocytic activity to provide maximum antigen monitoring capabilities of peripheral DCs. In the event of foreign antigen encounter, endocytosis is temporarily enhanced to increase antigenic load within endosomal structures[255]. This finding has been attributed to DCs and explains the drastic increase in labeling efficiency when compared to undifferentiated HSCs. As assessed through iron assays after magnetic separation, intracellular iron content was drastically increased in iDCs when compared to labeled HSCs (Figure 3.8B). DCs represent professional APCs biologically designed to take up vast amounts of extracellular materials, and thus resulted in high uptake quantities of MNP formulations.

Histological stainings provided information about the localization of iron oxide residues within labeled cells. Prussian blue staining patterns were localized intracellularly in numerous vesicles confined to the cytosol. MNPs were not found at the cell surface or within the nucleus. These results were consistent throughout all cell types examined and all MNP formulations employed, suggesting a global endocytic uptake mechanism. This finding is in agreement with previous studies proving shuttling of MNPs to early and late endosomes for subsequent degradation and processing[256].

Furthermore, investigations of iDCs using TEM displayed a strong correlation between MNP surface decoration and electron stopping power that has been reported in previous studies by Schwarz et al.[175]. It can be envisioned that adhesive or repulsive forces are responsible for individual particle agglomeration effects that shape intracellular trafficking and endosomal compartmentalization. It also has been known that endosomal compartments are low in pH, possibly contributing to exocytosis, MNP destabilization and clustering effects after uptake[257].

4.3 MRI Contrast Agent Potential

Recently, MRI has advanced to an indispensable imaging modality due to its capacity to yield excellent high-resolution images of target tissues within a detailed anatomical context. In particular, *in vitro* labeling of target cells with nano-scaled contrast agents prior to implantation provides a powerful tool for tracking and monitoring cellular migration using MRI[258,259]. The potential of iron oxide based MNP formulations to serve as T2 and T2* shortening contrast agent to be used in clinical diagnosis and/or drug delivery systems have to be evaluated in order to establish a correlation between surface MNP decoration, target cell type to be labeled, and MR imaging properties[18,23,174]. Therefore, an evaluation of the molecular imaging properties was performed by employing high-resolution T2 and T2* 3D echo scans as well as map scans. The range of detection limits provided insights into minimal MNP-labeled cell numbers still being able to generate a local field inhomogeneity that can be visualized as signal reduction pattern with significant contrast. Iron oxide based particles influence MRI contrast due to changes in the local magnetic field homogeneity (T2* relaxation time) that depends on the magnetic moment and/or the size of the single particle. Larger particles, as shown from studies using micron-sized iron oxide particles, yield larger magnetic susceptibility that results in higher R2 and R2* relaxation rates[33,260].

All iron oxide based particles employed in this study provided good imaging characteristics, however, intracellular shuttling parameters of individual MNPs resulted in changes with regard to MRI potential. As shown in several independent studies, T2 and T2* contrast of paramagnetic contrast agents is a result of MNP accumulation that results in a proton environment change of surrounding hydrogen protons present in water molecules[261,262]. The accumulation density, overall quantity of cellular MNP uptake, and intracellular packaging therefore lead to the formation of altered, yet MNP-specific imaging characteristics. In this study, it was demonstrated that PDAD-MNP is particularly suitable to trace labeled target cells populations down to a minimum seeding density of 10^2 cells/drillhole (Figures 3.13+3.14). This observation is in marked contrast to Chit-MNP, which could only be visualized down to a DC concentration of 10^4 cells. We attribute this finding to the intracellular fate of engulfed particle formulations.

Using TEM studies, we showed that different MNP formulations resulted in variable intracellular agglomeration effects within endosomal vesicles after successful uptake into iDCs (Figure 3.10). This observation was further supported by quantifying electron densities of MNP clusters within sub-cellular compartments in high-resolution TEM images. PDAD-MNP provided highest electron stopping power as inferred from deduced numerical greyscale values. Interestingly, this in turn translated into favorable imaging characteristics as previously described by Schwarz et al.[175].

Generally speaking, an increase in molecular imaging properties can be achieved through increasing labeling concentrations, and thus, intracellular iron load. However, elevated intracellular iron oxide accumulation potentially leads to adverse cellular effects as previously discussed. In a given clinical setting, viability and functionality of employed cellular vectors remains crucial for diagnostic and therapeutic imaging outcome. Optimizing contrast agent performance with regard to sensitivity and specificity therefore allows targeted molecular imaging without compromising biocompatibility.

4.4 Immunological Consequences after Contrast Agent Exposure

Magnetic nanoparticles coated with polymeric structures have been known to be biologically inert, however, recent studies also provide data pointing towards an immunogenic potential of MNPs[223,263]. In medical diagnostics, these biological alterations are undesirable i.e. in the case of systemic administration of contrast agents prior to MRI scans. Furthermore, systemic

administration of contrast agents cannot result in systemic immune reactions that could potentially be fatal for the patient being imaged. On the other hand, there is a growing number of medical research aiming at exploiting immunological consequences of targeted MNP delivery systems as part of therapeutic treatment regimes[13,14,264]. Since immune cells sense foreign exogenous matter prior to other tissues, it is feasible to target them as vectors to convey a desired immunological endpoint that is favorable for such medical applications[172,265].

In order to test the involvement of both adaptor proteins and TLR receptors on signaling after MNP exposure, MyD88, TLR4 and TLR9 knockout cells were employed. It has been previously shown that TLRs and their downstream effector and adaptor molecules are crucial in initiating appropriate molecular countermeasures responsible for engaging exogenous threats such as bacteria and viruses[92,93]. Extracellular matter and particles that are taken up by phagocytosis mediated by pattern recognition receptors lead to a prominent up-regulation of cytokine and chemokine related genes involved in further immune-modulatory actions[44,81].

Therefore, MNP formulations employed herein were tested for their potential to alter phenotypic surface marker composition of hematopoietic cell types as an indication of potential immunogenicity. In case of undifferentiated progenitor cells, none of the employed MNP formulations caused a change in surface marker make-up including lineage markers (Figure 3.4), verifying that synthetic contrast agents employed in this study do not induce altered or even adverse phenotypic effects, and biological consequences to HSC remain minimal in a wide range of experimental conditions. This finding can be attributed to the low amount to particles being taken up by target cells and the given experimental conditions. However, due to the growing interest in medical treatment and reconstitution therapies involving multipotent stem cells in combination with molecular imaging techniques, possible adverse effects on target populations need to be evaluated.

In case of the different DC subsets being employed in this study, no up-regulation of co-stimulatory molecules that would confer immunological activity nor increased MHC II levels were detected in case of lipid-shell, polymer-based, and covalently functionalized MNPs. Therefore, MNP formulations can be expected to be biologically inert. These data are in agreement with studies addressing similar questions[175]. To further support this notion, secreted levels of pro-inflammatory cytokines were determined. In agreement with previously acquired cytometric data, no elevated release of IL-6, IL12p40, and TNFα was recorded for

all synthetic MNPs, providing additional evidence as to the inertness of particle formulations. However, Dementо et al. showed that synthetic polymer MNPs do indeed have the potential to activate immune cells[266].

Biogenic MNPs derived from bacteria, on the other hand, displayed a strong potential to induce the up-regulation of differentiated cell types tested such as various DC subsets and macrophages. Even though magnetosomes employed are purified bacterial organelles, structural proteins linking single domain iron oxide cores could be the reason for MNP-dependent up-regulation of co-stimulatory molecules CD80 and CD86 as well as MHC II. Significantly elevated levels of pro-inflammatory cytokines and cell proliferation events employing explanted cultures of splenocytes proved that biogenic magnetosomes indeed lead to an up-regulation of immune functions within these target cells. To address the involvement of PRRs and subsequent downstream NFκB signaling, knockout experiments employing TLR4, TLR9, and downstream adaptor protein MyD88 deficient cells were performed.

In the context of these studies, bacterial magnetosomes displayed pronounced cellular activation potential in a TLR4 dependent manner. Both the absence of TLR4 and its downstream signaling molecule MyD88 resulted in the abrogation of immunological responses seen in Wt cells, providing evidence as to their dependency. Poly-electrolyte, lipid-shell, and covalently functionalized “stealth” MNPs, however, did not show a significant response within target immune cells. As previously discussed in similar studies, this is most likely due to generalized endocytic uptake mechanisms[125,126]. In marked contrast, MSR-1 MNPs were most likely taken up through receptor-mediated endocytosis, leading to maturation effects as shown in this study.

In order to examine a possible involvement of the inflammasome in the presence of MNP formulations, M-CSF generated macrophages were pre-stimulated with a low priming dose of the TLR4 antagonist LPS. Several studies have shown the involvement of the inflammasome pathway in combination with administered contrast agents, which is desirable in the case of i.e. vaccine therapies. Particles being used serve as adjuvants in addition to providing molecular imaging characteristics. However, only the bacterial magnetosome MSR-1 resulted in pronounced IL-1ß release. Both LPS pre-stimulated as well as stimulation of macrophages with MSR-1 alone lead to an ASC-dependent cleavage of pro-IL-1ß and subsequent detection in supernatants (Figure 3.31). No other tested MNP formulation resulted in a marked initiation of the inflammasome pathway (data not shown). It was shown in this study that MSR-1 involves TLR signaling, namely TLR4. In the absence of this PRR receptor in knockout

models, the cellular response is significantly diminished similar to LPS controls (Figures 3.35+3.36).

Furthermore, functionalizing acrylated MNPs with CpG motifs did not lead to the desirable TLR9 dependent immunological responses in pDCs (Figure 3.50). Even though CpG coupling motifs alone resulted in a pronounced up-regulation of both CD80 and CD86, residual cellular activation remaining after several MNP purifications ceased to control baseline levels. This served as an indication of uncompleted ligand coupling given the experimental settings.

4.5 Concluding Remarks

Taken together, this study provides insights into uptake and intracellular packaging properties in the context of different iron oxide based nanoparticles involving murine immune cells. The LbL technology proved to be highly valuable in shaping MNP surface characteristics that conferred enhanced cellular uptake and MR imaging properties, in particular the positively charged poly-electrolytes PDAD and PEI. In addition, oleate-stabilized lipid-shell MNPs provided a solid platform combining both good cellular uptake characteristics and MR imaging properties. Herein, we provide evidence that endocytic compartmentalization after successful uptake of MNP formulations markedly shapes resulting MR imaging properties.

Therefore, our data suggest a critical involvement of MNP surface structures with regard to (i) cellular uptake and (ii) intracellular fate of administered contrast agents. Furthermore, these criteria impact on resulting imaging properties employing MRI as shown in this work. Inherent clustering properties of MNP formulations dependent on both (i) the particle chemistry and (ii) biological interactions can be expected to shape imaging as well as cellular/immunological results. Through shaping immunological consequences, as was observed in case of MSR-1, a specific induction of cellular phenotypes can be achieved. This includes both innate immunological countermeasures including i.e. the inflammasome and T cell mediated adaptive immune consequences. As intended, synthetic MNPs employed herein proved to be biologically inert in all experimental settings. In combination with their MRI potential, especially positively charged LbL poly-electrolyte MNPs represent a promising labeling vector for hematopoietic cells of various developmental stages.

However, these data point towards the numerous variables that have to be accounted for when designing molecular probes for a specific imaging goal. Biological processes, particularly

during *in vivo* cell tracking or treatment monitoring, fundamentally shape or even alter the designed chemical properties of imaging agents dramatically. Surpassing current MNP limitations during the development of the next generation of MR contrast agents will be the focus of coming interdisciplinary research efforts.

5 References

1. Tarik F. Massoud and Sanjiv S. Gambhir. Molecular imaging in living subjects: seeing fundamental biological processes in a new light. Genes & Development 17, 545-580 (2003).
2. Ralph Weissleder. Imaging in the era of molecular oncology. Nature 452, 580-589 (2008).
3. Simon M. Amatamey, Michael Honer, and Pius A. Schubiger. Molecular Imaging with PET. Chem Rev 1501-1516 (2008).
4. Markus Rudin and Ralph Weissleder. Molecular Imaging in Drug Discovery and Development. Nature 123-131 (2003).
5. Juergen K. Willmann, Nicholas van Bruggen, Ludger M. Dinkelborg, and Sanjiv S. Gambhir. Molecular imaging in drug development. Nature Rev Drug Discov 7, 591-607 (2008).
6. Enzo Terreno, Daniela D. Castelli, Alessandra Viale, and Silvio Aime. Challenges for Molecular Magnetic Resonance Imaging. Chem Rev 110, 3019-3042 (2010).
7. Jeff W.M. Bulte and Dara L. Kraitchman. Iron oxide MR contrast agents for molecular and cellular imaging. NMR in Biomedicine 17, 484-499 (2004).
8. Ralph Weissleder and Umar Mahmood. Molecular Imaging. Radiology 219, 316-333 (2001).
9. Ben N.G. Giepmans, Stephen R. Adams, Mark H. Ellisman, and Roger Y. Tsien. The Fluorescent Toolbox for Assessing Protein Location and Function. Science 312, 217-224 (2006).
10. Daniel L.J. Thorek, Antony K. Chen, Julie Czupryna, and Andrew Tsourkas. Superparamagnetic Iron Oxide Nanoparticle Probes for Molecular Imaging. Annals of Biomedical Engineering 34, 23-38 (2006).
11. Lisa Brannon-Peppas and James O. Blanchette. Nanoparticle and targeted systems for cancer therapy. Advanced Drug Delivery Reviews 56, 1649-1659 (2004).
12. Stephane Mornet, Sebastien Vasseur, Fabien Grasset, and Etienne Duguet. Magnetic nanoparticle design for medical diagnosis and therapy. J Mater Chem 14, 2161-2175 (2004).
13. Carl G. Figdor, Jolanda M. de Vries, Joost Lesterhuis, and Cornelis J.M. Melief. Dendritic cell immunotherapy: mapping the way. Nature 10, 475-480 (2004).
14. Jolanda M. de Vries et al.. Magnetic resonance tracking of dendritic cells in melanoma patients for monitoring of cellular therapy. Nature 23, 1407-1413 (2005).
15. Jeff W.M. Bulte et al.. Magnetodendrimers allow endosomal magnetic labeling and in vivo tracking of stem cells. Nature Biotech 19, 1141-1147 (2001).
16. Mathias Hoehn et al.. Monitoring of implanted stem cell migration in vivo: A highly resolved in vivo magnetic resonance imaging investigation of experimental stroke in rat. PNAS 99, 16267-16272 (2002).

17. Jeff W.M. Bulte. Hot spot MRI emerges from the background. Nature 23, 945-946 (2005).

18. Uwe Himmelreich and Mathias Hoehn. Stem cell labeling for magnetic resonance imaging. Minim Invasive Ther Allied Technol 17, 132-142 (2008).

19. F. Bloch. Nuclear induction. Physical Review 70, 460-474 (1946).

20. Tobias Schaeffter and Hannes Dahnke. Magnetic Resonance Imaging and Spectroscopy. Handbook Exp Pharmacology 185, 75-90 (2008).

21. Denis Le Bihan. Looking into the functional architecture of the brain. Nature Rev Neurosci 4, 469-480 (2003).

22. C.T. Moonen, P.C. van Zijl, J.A. Frank, D. Le Bihan, and E.D. Becker. Functional magnetic resonance imaging in medicine and physiology. Science 250, 53-61 (1990).

23. Conroy Sun, Jerry S.H. Lee, and Miqin Zhang. Magnetic nanoparticles in MR imaging and drug delivery. Advanced Drug Delivery Reviews 60, 1252-1265 (2008).

24. Stasia A. Anderson et al.. Noninvasive MR imaging of magnetically labeled stem cells to directly identify neovasculature in a glioma model. Blood 105, 420-425 (2005).

25. Mark E. Davis, Zhuo Chen, and Dong M. Shin. Nanoparticle therapeutics: an emerging treatment modality for cancer. Nature Reviews Drug Discovery 7, 771-782 (2008).

26. Peter Caravan. Strategies for increasing the sensitivity of gadolinium based MRI contrast agents. Chem Soc Rev 35, 512-523 (2006).

27. Gustav J. Strijkers, Willem J.M. Mulder, Geralda A.F. van Tilborg, and Klaas Nicolay. MRI Contrast Agents: Current Status and Future Perspectives. Anti Cancer Agents in Med Chem 7, 291-305 (2007).

28. Anne M. Morawski et al.. Targeted Nanoparticles for Quantitative Imaging of SParse Molecular Epitopes with MRI. Magn Reson Med 51, 480-486 (2004).

29. Matthew D. Budde and Joseph A. Frank. Magnetic Tagging of Therapeutic Cells for MRI. J Nucl Med 50, 171-174 (2009).

30. Robert S. Negrin et al.. Transplantation of Highly Purified CD34+Thy-1+ Hematopoietic Stem Cells in Patients with Metastatic Breast Cancer. Biol Blood Marrow Transpl 6, 262-271 (2000).

31. Julie M. Vose et al.. Transplantation of HIghly Purified CD34+THy-1+ Hematopoietic Stem Cells in Patients With Recurrent Indolent Non-Hodgkin's Lymphoma. Soc Blood Marrow Transpl 7, 680-687 (2001).

32. Ali S. Arbab et al.. Intracytoplasmic tagging of cells with ferumoxides and transfection agent for cellular magnetic resonance imaging after cell transplantation: methods and techniques. Transplantation 76, 1123-1130 (2003).

33. Kathleen A. Hinds et al.. Highly efficient endosomal labeling of progenitor and stem cells with large magnetic particles allows magentic rsonance imaging of single cells. Blood 102, 867-872 (2003).

34. Gosse J. Adema, Jolanda M. de Vries, Cornelis J.A. Punt, and Carl G. Figdor. Migration of dendritic cell based cancer vaccines: in vivo veritas? Curr Opin Immunol 17, 170-174 (2005).

35. Irving L. Weissman. Stem Cells: Units of Development, Units of Regeneration, and Units of Evolution. Cell 100, 157-168 (2012).

36. Gerald J. Spangrude, Shelly Heimfeld, and Irving L. Weissman. Purification and Characterization of Mouse Hematopoietic Stem Cells. Science 241, 58-62 (1988).

37. J. Zhang et al.. Identification of the hematopoietic stem cell niche and control of the niche size. Nature 425, 836-841 (2003).

38. Judith A. Shizuru, Robert S. Negrin, and Irving L. Weissman. Hematopoietic Stem and Progenitor Cells: Clinical and Preclinical Regeneration of the Hematolymphoid System. Annu Rev Med 56, 509-538 (2005).

39. Stuart H. Orkin. Diversification of haematopoietic stem cells to specific lineages. Nature Reviews Genetics 1, 57-64 (2000).

40. Stuart H. Orkin and Leonard I. Zon. Hematopoiesis: An Evolving Paradigm for Stem Cell Biology. Cell 132, 631-644 (2008).

41. Frederic Geissmann, Markus G. Manz, Steffen Jung, Michael H. Sieweke, Miriam Merad, and Klaus Ley. Development of Monocytes, Macrophages, and Dendritic Cells. Science 327, 656-661 (2010).

42. Eric Vivier and Bernard Malissen. Innate and adaptive immunity: specificities and signaling hierarchies revisited. Nature Immunol 6, 17-21 (2005).

43. Ruslan Medzhitov. Recognition of microorganisms and activation of the immune response. Nature 449, 819-826 (2007).

44. Glenn Dranoff. Cytokines in cancer pathogenesis and cancer therapy. Nature Rev Cancer 4, 11-22 (2004).

45. Ruslan Medzhitov and Charles A. Janeway. Innate immunity: impact on the adaptive immune response. Curr Opin Immunol 9, 4-9 (2002).

46. Ruslan Medzhitov and Charles A. Janeway. Innate Immunity: The Virtues of a Nonclonal System of Recognition. Cell 91, 295-298 (1997).

47. Kasper Hoebe, Edith Janssen, and Bruce Beutler. The interface between innate and adaptive immunity. Nature Immunol 5, 971-974 (2004).

48. Charles A. Janeway and Ruslan Medzhitov. Innate Immune Recognition. Annu Rev Immunol 20, 197-216 (2002).

49. Zeev Pancer and Max D. Cooper. The evolution of adaptive immunity. Annu Rev Immunol 24, 497-518 (2006).

50. Daniel Ricklin, George Hajishengallis, Kun Yang, and John D. Lambris. Complement: a key system for immune surveillance and homeostasis. Nature Immunol 11, 785-797 (2010).

51. Peter F. Zipfel. Complement and immune defense: From innate immunity to human disease. Immunol Letters 126, 1-7 (2009).

52. Peter M. Henson and David A. Hume. Apoptotic cell removal in development and tissue homeostasis. Trends Immunol 27, 244-250 (2006).

53. Alan Aderem and Richard J. Ulevitch. Toll-like receptors in the induction of the innate immune response. Nature 406, 782-787 (2000).

54. Estee M. Toeroek, Fiona J. Cooke, and Ed Moran. Innate defense mechanisms. Oxford Handbook Inf Disease and Microbiol (2010).

55. David A. Hume et al.. The mononuclear phagocyte system revisited. J Leukocyte Biol 72, 621-627 (2002).

56. Andrew S. Cowburn, Alison M. Condliffe, Neda Farahi, Charlotte Summers, and Edwin R. Chilvers. Advances in Neutrophil Biology: Clinical Implications. Chest 134, 606-612 (2008).

57. Oliver Soehnlein et al.. Neutrophil secretion products pave the way for inflammatory monocytes. Blood 112, 1461-1471 (2008).

58. T.G. Gabig and B.M. Babior. The Killing of Pathogens by Phagocytes. Annu Rev Med 32, 313-326 (1981).

59. Stefan H.E. Kaufmann. Cell-mediated immunity: Dealing a direct blow to pathogens. Curr Biol 9, 97-99 (1999).

60. Christine A. Biron and Laurent Brossay. NK cells and NKT cells in innate defense against viral infections. Curr Opin Immunol 13, 458-464 (2001).

61. Klas Kaerre. NK Cells, MHC Class I Molecules and the Missing Self. Scand J Immunol 55, 221-228 (2002).

62. Bali Pulendran and Santa J. Ono. A shot in the arm of mast cells. Nature Med 14, 536-541 (2008).

63. Siamon Gordon and Philip R. Taylor. Monocyte and macrophage heterogeneity. Nature Rev Immunol 5, 953-964 (2005).

64. Koichi Akashi, David Traver, Toshihiro Miyamoto, and Irving L. Weissman. A clonogenic common myeloid progenitor that gives rise to all myeloid lineages. Nature 404, 193-197 (2000).

65. Ralph van Furth and Zanvil A. Cohn. The origin and kinetics of mononuclear phagocytes. J Exp Med 415-435 (1968).

66. Subhra K. Biswas and Alberto Mantovani. Macrophage plasticity and interaction with lymphocyte subsets: cancer as a paradigm. Nature Immunol 11, 889-896 (2010).

67. David M.Mosser and Justin P.Edwards. Exploring the full spectrum of macrophage activation. Nature 8, 958-969 (2008).

68. Alberto Mantovani, Antonio Sica, and Massimo Locati. Macrophage Polarization Comes of Age. Immunity 23, 344-346 (2005).

69. Charles D. Mills, Kristi Kincaid, Jennifer M. Alt, Michelle J. Heilman, and Annette M. Hills. M-1/M-2 Macrophages and the Th1/Th2 Paradigm. J Immunol 164, 6166-6173 (2000).

70. Bin-Zhi Qian and Jeffrey W. Pollard. Macrophage Diversity Enhances Tumor Progression and Metastasis. Cell 141, 39-51 (2010).

71. Siamon Gordon. Alternative Activation of Macrophages. Nature Rev Immunol 3, 23-35 (2003).

72. Ralph M. Steinman and Jacques Banchereau. Taking dendritic cells into medicine. Nature 449, 419-426 (2007).

73. Christopher C. Norbury. Drinking a lot is good for dendritic cells. Immunology 117, 443-451 (2006).

74. Patrick Blanco, Karolina A. Palucka, Virginia Pascual, and Jacques Banchereau. Dendritic cells and cytokines in human inflammatory and autoimmune diseases. Cytokines, Dendritic Cells and Immunological Rejection 19, 41-52 (2008).

75. D.G. Schatz, M.A. Oettinger, and M.S. Schlissel. V(D)J Recombination: Molecular Biology and Regulation. Annu Rev Immunol 10, 359-383 (1992).

76. Tomohiro Kurosaki. B-lymphocyte biology. Immunol Rev 237, 5-9 (2010).

77. Tim R. Mosmann and Subash Sad. The expanding universe of T-cell subsets: Th1, Th2 and more. Immunology Today 17, 138-146 (1996).

78. Casey T. Weaver, Laurie E. Harrington, Paul R. Mangan, Maya Gavrieli, and Kenneth M. Murphy. Th17: An Effector CD4 T Cell Lineage with Regulatory T Cell Ties. Immunity 24, 677-688 (2006).

79. Daniel L. Mueller. Mechanisms maintaining peripheral tolerance. Nature Immunol 11, 21-27 (2010).

80. Kristin A. Hogquist, Troy A. Baldwin, and Stephen C. Jameson. Central tolerance: learning self-control in the thymus. Nature Rev Immunol 5, 772-782 (2005).

81. Jason G. Cyster. Chemokines and Cell Migration in Secondary Lymphoid Organs. Science 286, 2098-2102 (1999).

82. Michael Reth and J. Wienands. Initiation and Processing of Signals from the B Cell Antigen Receptor. Annu Rev Immunol 15, 453-479 (1997).

83. Thomas A. Ferguson, Jayoung Choi, and Douglas R. Green. Armed response: how dying cells influence T-cell functions. Immunol Rev 241, 77-88 (2011).

84. Mark A. Wallet, Pradip Sen, and Roland Tisch. Immunoregulation of Dendritic Cells. Clin Med & Res 3, 166-175 (2005).

85. Elodie Segura and Jose A. Villadangos. Antigen presentation by dendritic cells in vivo. Curr Opin Immunol 21, 105-110 (2009).

86. Stuart G. Tangye and David M. Tarlinton. Memory B cells: Effectors of long-lived immune responses. Eur J Immunol 39, 2065-2075 (2009).

87. Manfred B. Lutz and Gerold Schuler. Immature, semi-mature and fully mature dendritic cells: which signals induce tolerance or immunity? Trends Immunol 23, 445-449 (2002).

88. Martin Zenke and Thomas Hieronymus. Towards an understanding of the transcription factor network of dendritic cell development. Trends Immunol 27, 140-145 (2006).

89. Jacques Banchereau et al.. Immunobiology of Dendritic Cells. Annu Rev Immunol 18, 767-811 (2000).

90. Teunis B.H. Geijtenbeek and Sonja I. Gringhuis. Signalling through C-type lectin receptors: shaping immune responses. Nature Rev Immunol 9, 465-479 (2009).

91. Jacques Banchereau and Ralph M. Steinman. Dendritic cells and the control of immunity. Nature 392, 245-252 (1998).

92. Shizuo Akira, Satoshi Uematsu, and Osamu Takeuchi. Pathogen Recognition and Innate Immunity. Cell 124, 783-801 (2006).

93. Taro Kawai and Shizuo Akira. The role of pattern-recognition receptors in innate immunity: update on Toll-like receptors. Nature Immunol 11, 373-384 (2010).

94. J.A. Villadangos and H.L. Ploegh. Proteolysis in MHC class II antigen presentation: who's in charge? Immunity 12, 233-239 (2000).

95. Ted H. Hansen and Marlene Bouvier. MHC class I antigen presentation: learning from viral evasion strategies. Nature Rev Immunol 9, 503-513 (2009).

96. Pierre Guermonprez, Jenny Valladeau, Laurence Zitvogel, Clotilde Thery, and Sebastian Amigorena. Antigen presentation and T-cell stimulation by dendritic cells. Annu Rev Immunol 20, 621-667 (2002).

97. Kang Liu et al.. Immune Tolerance After Delivery of Dying Cells to Dendritic Cells In Situ. J Exp Med 196, 1091-1097 (2002).

98. Manfred B. Lutz and Christian Kurts. Induction of peripheral CD4+ T-cell tolerance and CD8+ T-cell cross-tolerance by dendritic cells. Europ J Immunol 39, 2325-2330 (2009).

99. Miriam Merad and Markus G. Manz. Dendritic cell homeostasis. Blood 113, 3418-3427 (2009).

100. Yong-Jun Liu. Dendritic Cell Subsets and Lineages, and Their Functions in Innate and Adaptive Immunity. Cell 106, 259-262 (2001).

101. Thomas Hieronymus et al.. Progressive and Controlled Development of Mouse Dendritic Cells from Flt3+CD11b+ Progenitors In Vitro. J Immunol 174, 2552-2562 (2005).

102. Angela D'Amico and Li Wu. The Early Progenitors of Mouse Dendritic Cells and Plasmacytoid Predendritic Cells Are within the Bone Marrow Hematopoietic Precursors Expressing Flt3. J Exp Med 198, 293-303 (2003).

103. Ken Shortman and Shalin H. Naik. Steady-state and inflammatory dendritic-cell development. Nature Rev Immunol 7, 19-30 (2007).

104. Alfonso Martin-Fontecha et al.. Regulation of Dendritic Cell Migration to the Draining Lymph Node: Impact on T Lymphocyte Traffic and Priming. J Exp Med 198, 615-621 (2003).

105. Claudia Jakubzick et al.. Lymph-migrating, tissue-derived dendritic cells are minor constituents within steady-state lymph nodes. J Exp Med 205, 2839-2850 (2008).

106. Hiroyuki Yoneyama, Kenjiro Matsuno, and Kouji Matsushima. Migration of Dendritic Cells. Int J Hematol 81, 204-207 (2005).

107. Laura S. Bursch et al.. Identification of a novel population of Langerin+ dendritic cells. J Exp Med 204, 3147-3156 (2007).

108. Lionel F. Poulin et al.. The dermis contains langerin+ dendritic cells that develop and function independently of epidermal Langerhans cells. J Exp Med 204, 3119-3131 (2007).

109. Florent Ginhoux et al.. Blood-derived dermal langerin+ dendritic cells survey the skin in the steady state. J Exp Med 204, 3133-3146 (2007).

110. Florent Ginhoux et al.. The origin and development of nonlymphoid tissue CD103+ DCs. J Exp Med 206, 3115-3130 (2009).

111. Chen Varol et al.. Intestinal Lamina Propria Dendritic Cell Subsets Have Different Origin and Functions. Immunity 31, 1-11 (2009).

112. Sandrine Henri et al.. The Dendritic Cell Populations of Mouse Lymph Nodes. J Immunol 167, 741-748 (2001).

113. Ken Shortman and Yong-Jun Liu. Mouse and Human Dendritic Cell Subtypes. Nature Rev Immunol 2, 151-161 (2002).

114. William R. Heath et al.. Cross-presentation, dendritic cell subsets, and the generation of immunity to cellular antigens. Immu Rev 199, 9-26 (2004).

115. Kenneth L. Rock and Lianjun Shen. Cross-presentatin: underlying mechanisms and role in immune surveillance. Immunol Rev 207, 166-183 (2005).

116. Sven Burgdorf and Christian Kurts. Endocytosis mechanisms and the cell biology of antigen presentation. Curr Opin Immunol 20, 89-95 (2008).

117. Sven Burgdorf, Andreas Kautz, Volker Boehnert, Percy A. Knolle, and Christian Kurts. Distinct Pathways of Antigen Uptake and Intracellular Routing in CD4 and CD8 T Cell Activation. Science 316, 612-616 (2007).

118. Anna I. Proietto et al.. Differential production of inflammatory chemokines by murine dendritic cell subsets. Immunobiology 1, 163-172 (2004).

119. Hideki Nakano, Manabu Yanagita, and Michael Dee Gunn. CD11c+B220+Gr-1+ Cells in Mouse Lymph Nodes and Spleen Display Characteristics of Plasmacytoid Dendritic Cells. J Exp Med 194, 1171-1178 (2001).

120. Lynn Corcoran et al.. The Lymphoid Past of Mouse Plasmacytoid Cells and Thymic Dendritic Cells. J Immunol 170, 4926-4932 (2003).

121. Martina Fuchsberger, Hubertus Hochrein, and Meredith O'Keeffe. Activation of plasmacytoid dendritic cells. Immunol Cell Biol 83, 571-577 (2005).

122. Jose A. Villadangos and Louise Young. Antigen-Presentation Properties of Plasmacytoid Dendritic Cells. Immunity 29, 352-361 (2008).

123. Natalya V. Serbina, Thais P. Salazar-Mather, Christine A. Biron, William A. Kuziel, and Eric G. Pamer. TNF/iNOS-Producing Dendritic Cells Mediate Innate Immune Defense against Bacterial Infection. Immunity 19, 59-70 (2003).

124. Cedric Auffray, Michael H. Sieweke, and Frederic Geissmann. Blood Monocytes: Development, Heterogeneity, and Relationship with Dendritic Cells. Annu Rev Immunol 27, 669-692 (2009).

125. Sean D. Conner and Sandra L. Schmid. Regulated portals of entry into the cell. Nature 422, 37-44 (2003).

126. Gary J. Doherty and Harvey T. McMahon. Mechanisms of Endocytosis. Annu Rev Biochem 78, 857-902 (2009).

127. J.M. Besterman and R.B. Low. Endocytosis: a review of mechanisms and plasma membrane dynamics. Biochem J 210, 1-13 (1983).

128. Marko Kaksonen, Christopher P. Toret, and David G. Drubin. Harnessing actin dynamics for clathrin-mediated endocytosis. Nature Rev Mol Cell Biol 7, 404-414 (2006).

129. Kohji Takei and Volker Haucke. Clathrin-mediated endocytosis: membrane factors pull the trigger. Trends Cell Biol 11, 385-391 (2001).

130. Ivan R. Nabi and Phuong U. Le. Caveolae/raft-dependent endocytosis. J Cell Biol 161, 673-677 (2003).

131. Satyajit Mayor and Richard E. Pagano. Pathways of clathrin-independent endocytosis. Nature Rev Mol Cell Biol 8, 603-612 (2007).

132. Kirsten Sandvig, Maria L. Torgersen, Hilde A. Raa, and Bo van Deurs. Clathrin-independent endocytosis: from nonexisting to an extreme degree of complexicity. Histochem Cell Biol 129, 267-276 (2008).

133. Alan Aderem and David M. Underhill. Mechanisms of phagocytosis in macrophages. Annu Rev Immunol 17, 593-623 (1999).

134. Lynda M. Stuart and Alan R. Ezekowitz. Phagocytosis and comparative innate immunity: learning on the fly. Nature Rev Immunol 8, 131-141 (2008).

135. Britta Qualmann and Michael M. Kessels. Endocytosis and the cytoskeleton. Int Review Cytol 220, 93-144 (2002).

136. Lynda M. Stuart and Alan R. Ezekowitz. Phagocytosis: Elegant Complexity. Immunity 22, 539-550 (2005).

137. Ken J. Ishii, Shohei Koyama, Atsushi Nakagawa, Cevayir Coban, and Shizuo Akira. Host Innate Immune Receptors and Beyond: Making Sense of Microbial Infections. Cell Host Microbe 3, 352-363 (2008).

138. Osamu Takeuchi and Shizuo Akira. Pattern Recognition Receptors and Inflammation. Cell 140, 805-820 (2010).

139. Himanshu Kumar, Taro Kawai, and Shizuo Akira. Toll-like receptors and innate immunity. Biochem Biophys Res Comm 388, 621-625 (2009).

140. Nicholas J. Gay and Monique Gangloff. Structure and Function of Toll Receptors and Their Ligands. Annu Rev Biochem 76, 141-165 (2007).

141. Kiyoshi Takeda and Shizuo Akira. Toll-like receptors in innate immunity. Int Immunol 17, 1-14 (2005).

142. Hua Shen, Bethany M. Tesar, Wendy E. Walker, and Daniel R. Goldstein. Dual Signaling of MyD88 and TRIF Is Critical for Maximal TLR4-Induced Dendritic Cell Maturation. J Immunol 181, 1849-1858 (2008).

143. Shizuo Akira, Kiyoshi Takeda, and Tsuneyasu Kaisho. Toll-like receptors: critical proteins linking innate and acquired immunity. Nature Immunol 2, 675-680 (2001).

144. Joerg H. Fritz, Richard L. Ferrero, Dana J. Philpott, and Stephen E.Girardin. Nod-like proteins in immunity, inflammation and disease. Nature Immunol 7, 1250-1257 (2006).

145. Maria Kaparakis, Dana J. Philpott, and Richard L. Ferrero. Mammalian NLR proteins; discriminating foe from friend. Immunol Cell Biol 85, 495-502 (2007).

146. Fabio Martinon and Juerg Tschopp. NLRs join TLRs as innate sensors of pathogens. Trends Immunol 26, 447-454 (2005).

147. Fabio Martinon and Juerg Tschopp. Inflammatory Caspases: Linking an Intracellular Innate Immune System to Autoinflammatory Diseases. Cell 117, 561-574 (2004).

148. Laetitia Agostini et al.. NALP3 Forms an IL-1ß-Processing Inflammasome with Increased Activity in Muckle-Wells Autoinflammatory Disorder. Immunity 20, 319-325 (2004).

149. Joost P.H. Drenth and Jos M.W. van der Meer. The Inflammasome - A Linebacker of Innate Defense. N Engl J Med 2006, 730-732 (2006).

150. Pamela Gasse et al.. IL-1R1/MyD88 signaling and the inflammasome are essential in pulmonary inflammation and fibrosis in mice. J Clin Invest 117, 3786-3799 (2007).

151. Mitsutoshi Yoneyama et al.. The RNA helicase RIG-I has an essential function in double-stranded RNA-induced innate antiviral responses. Nature Immunol 5, 730-737 (2004).

152. Veit Hornung et al.. 5'-Triphosphate RNA is the Ligand for RIG-I. Science 314, 994-997 (2006).

153. Mitsutoshi Yoneyama, Koji Onomoto, and Takashi Fujita. Cytoplasmic recognition of RNA. Advanced Drug Delivery Reviews 60, 841-846 (2008).

154. Andre Nel, Tian Xia, Lutz Maedler, and Ning Li. Toxic Potential of Materials at the Nanolevel. Science 311, 622-627 (2006).

155. Andre Nel et al.. Understanding biophysicochemical interactions at the nano-bio interface. Nature Mat 8, 543-557 (2009).

156. Younjin Min, Mustafa Akbulut, Kai Kristiansen, Yuval Golan, and Jacob Israelachvili. The role of interparticle and external forces in nanoparticle assembly. Nature Mat 7, 527-538 (2008).

157. Gunter Oberdorster et al.. Principles for characterizing the potential human health effects from exposure to nanomaterials: elements of a screening strategy. Particle Fibre Toxic 2, 1-35 (2005).

158. S. Mornet et al.. Magnetic nanoparticle design for medical applications. Progr Solid State Chem 34, 237-247 (2006).

159. Donald E. Owens and Nicholas A. Peppas. Opsonization, biodistribution, and pharmacokinetics of polymeric nanoparticles. Int J Pharmac 307, 93-102 (2006).

160. Marina A. Dobrovolskaia and Scott E. McNeil. Immunological properties of engineered nanomaterials. Nature Nanotech 2, 469-478 (2007).

161. Piritta Felker et al.. TGF-beta1 accelerates dendritic cell differentiation from common dendritic cell progenitors and directs subset specification toward conventional dendritic cells. J Immunol 185, 5326-5335 (2010).

162. John E. Wong, Akhilesh Gaharwar, Detlef Mueller-Schulte, Dhirendra Bahadur, and Walter Richtering. Magnetic Nanoparticle-Polyelectrolyte Interaction: A Layered Approach for Biomedical Applications. J Nanosci Nanotech 8, 1-8 (2008).

163. Michael Hodenius et al.. Synthesis, Physicochemical Characterization and MR Relaxometry of Aqueous Ferrofluids. J Nanosci Nanotech 8, 2399-2409 (2008).

164. S. Khalafalla and G. Reimers. Preparation of dilution-stable aqueous magnetic fluids. IEEE Trans Magn 16, 178-183 (1980).

165. Karen Gruenberg et al.. Biochemical and Proteomic Analysis of the Magnetosome Membrane in Magnetospirillum gryphiswaldense. Appl Environ Microbiol 70, 1040-1050 (2004).

166. Karen Gruenberg, Cathrin Wawer, Bradley M. Tebo, and Dirk Schueler. A Large Gene Cluster Encoding Several Magnetosome Proteins Is Conserved in Different Species of Magnetotactic Bacteria. Appl Environ Microbiol 67, 4573-4582 (2001).

167. Esther Amstad et al.. Surface Functionalization of Single Superparamagnetic Iron Oxide Nanoparticles for Targeted Magnetic Resonance Imaging. Small 5, 1334-1342 (2009).

168. Esther Amstad, Torben Gillich, Idalia Bilecka, Markus Textor, and Erik Reimhult. Ultrastable Iron Oxide Nanoparticle Colloidal Suspensions Using Dispersants with Catechol-Derived Anchor Groups. Nano Lett 9, 4042-4048 (2009).

169. Esther Amstad. Surface Functionalizing Superparamagnetic Iron Oxide Nanoparticles Using Nitrocatechol Anchors. Ph D Thesis ETH Zuerich, Switzerland (2010).

170. R.Massart. Preparation of aqueous magnetic liquids in alkaline and acidic media. IEEE Trans Magn 17, 1247-1248 (1981).

171. Sebastian Schwarz et al.. Synthetic and biogenic magnetite nanoparticles for tracking of stem cells and dendritic cells. J Magn Magn Mat 321, 1533-1538 (2009).

172. Christiane Becker et al.. Uptake of magnetic nanoparticles into cells for cell tracking. J Magn Magn Mat 311, 234-237 (2007).

173. Jan Riemer, Hans H. Hoepken, Hania Czerwinska, Stephen R. Robinson, and Ralf Dringen. Colorimetric ferrozine-based assay for the quantification of iron in cultured cells. Anal Biochem 331, 370-375 (2004).

174. Catherine C. Berry and Adam S.G. Curtis. Functionalization of magnetic nanoparticles for applications in biomedicine. J Phys D: Appl Phys 36, 198-206 (2003).

175. Sebastian Schwarz et al. Polyelectrolyte coating of iron oxide nanoparticles for MRI-based cell tracking. Nanomed: Nanotech Biol Med In press, (2011).

176. Akiyoshi Hoshino et al.. Physicochemical Properties and Cellular Toxicity of Nanocrystal Quantum Dots Depend on Their Surface Modification. Nano Lett 4, 2163-2169 (2004).

177. An-Hui Lu, E.L. Salabas, and Ferdi Schueth. Magnetic Nanoparticles: Synthesis, Protection, Functionalization, and Application. Angew Chem Int Ed 46, 1222-1244 (2007).

178. Gero Decher. Fuzzy Nanoassemblies: Toward Layered Polymeric Multicomposites. Science 277, 1232-1237 (1997).

179. Werner Jaeger, Mathias Hahn, Antje Lieske, Arvid Zimmermann, and Fabien Brand. Polymerization of water soluble cationic vinyl monomers. Macromol Symp 111, 95-106 (1996).

180. Michael Neu, Dagmar Fischer, and Thomas Kissel. Recent advances in rational gene transfer vector design based on poly(ethylene imine) and its derivatives. J Gene Med 7, 992-1009 (2005).

181. Sheng-Li Chen, L. Krishnan, S. Srinivasan, J. Benziger, and A.B. Bocarsly. Ion exchange resin/polystyrene sulfonate composite membranes for PEM fuel cells. J Membr Sci 243, 327-333 (2004).

182. Caroline Lemarchand, Ruxandra Gref, and Patrick Couvreur. Polysaccharide-decorated nanoparticles. Eur J Pharma Biopharma 58, 327-341 (2004).

183. Sunil Agnihotri, Nadagouda Mallikarjuna, and Tejraj Aminabhavi. Recent advances on chitosan-based micro- and nanoparticles in drug delivery. J Contr Rel 100, 5-28 (2004).

184. Rainer Mueller, Karsten Maeder, and Sven Gohla. Solid lipid nanoparticles (SLN) for controlled drug delivery - a review of the state of the art. Eur J Pharma Biopharma 50, 161-177 (2000).

185. Dan Peer et al.. Nanocarriers as an emerging platform for cancer therapy. Nature Nanotech 2, 751-760 (2007).

186. Uta Wattendorf and Hans P. Merkle. PEGylation as a tool for the biomedical engineering of surface modified microparticles. J Pharma Sci 97, 4655-4669 (2008).

187. Michael Hodenius et al.. Biotinylated Stealth® magnetoliposomes. Chem Physi Lipid 120, 75-85 (2002).

188. Jingkun Jiang, Gunter Oberdorster, and Pratim Biswas. Characterization of size, surface charge, and agglomeration state of nanoparticle dispersions for toxicological studies. J Nanop Res 11, 77-89 (2009).

189. Richard C. Murdock, Laura Braydich-Stolle, Amanda M. Schrand, John J. Schlager, and Saber M. Hussain. Characterization of Nanomaterial Dispersion in Solution Prior to In Vitro Exposure Using Dynamic Light Scattering Technique. Toxicol Sci 101, 239-253 (2008).

190. Fiona M. Watt and Brigid L. Hogan. Out of Eden: Stem Cells and Their Niches. Science 287, 1427-1430 (2000).

191. J. Garcia-Castro et al.. Mesenchymal stem cells and their use as cell replacement therapy and disease modelling tool. J Cell Mol Med 12, 2552-2565 (2008).

192. Anne Y. Lai and Motonari Kondo. Asymmetrical lymphoid and myeloid lineage commitment in multipotent hematopoietic progenitors. J Exp Med 203, 1867-1873 (2006).

193. Nastassja Lewinski, Vicki Colvin, and Rebekah Drezek. Cytotoxicity of Nanoparticles. Small 4, 26-49 (2008).

194. Andrea Kunzmann et al.. Toxicology of engineered nanomaterials: Focus on biocompatibility, biodistribution and biodegradation. Biochimica Biophysica Acta 1810, 361-373 (2011).

195. Urs O. Haefeli et al.. Cell Uptake and in Vitro Toxicity of Magnetic Nanoparticles Suitable for Drug Delivery. Mol Pharma 6, 1417-1428 (2009).

196. Stefaan Soenen and Marcel de Cuyper. Assessing cytotoxicity of (iron oxide-based) nanoparticles: an overview of different methods exemplified with cationic magnetoliposomes. Contrast Media Mol Imag 4, 207-219 (2009).

197. Thomas R. Pisanic, Jennifer D. Blackwell, Veronica I. Shubayev, Rita R. Finones, and Sungho Jin. Nanotoxicity of iron oxide nanoparticle internalization in growing neurons. Biomaterials 28, 2572-2581 (2007).

198. Hiromi Iwasaki and Koichi Akashi. Myeloid Lineage Commitment from the Hematopoietic Stem Cell. Immunity 26, 726-740 (2007).

199. Xianfeng Fang, Pan Zheng, Jie Tang, and Yang Liu. CD24: from A to Z. Cell Mol Immunol 7, 100-103 (2010).

200. Gengmei Xing et al.. The Strong MRI Relaxivity of Paramagnetic Nanoparticles. J Phys Chem B 112, 6288-6291 (2008).

201. I. Schmid, C.H. Uittenbogaart, B. Keld, and J.V. Giorgi. A rapid method for measuring apoptosis and dual-color immunofluorescence by single laser flow cytometry. J Immunol Meth 170, 145-157 (1994).

202. Claire Wilhelm and Florence Gazeau. Universal cell labelling with anionic magnetic nanoparticles. Biomaterials 29, 3161-3174 (2008).

203. Amy Chow, Derek Toomre, Wendy Garrett, and Ira Mellman. Dendritic cell maturation triggers retrograde MHC class II transport from lysosomes to the plasma membrane. Nature 418, 988-994 (2002).

204. Satomichi Yoshimura, Jan Bondeson, Brian Foxwell, Fionula Brennan, and Marc Feldmann. Effective antigen presentation by dendritic cells is NF-kB dependent: coordinate regulation of MHC, co-stimulatory molecules and cytokines. Int Immunol 13, 675-683 (2001).

205. Ralph M.Steinman and Kayo Inaba. Myeloid dendritic cells. J Leukocyte Biol 66, 205-208 (1999).

206. Q.A. Pankhurst, J. Connolly, S.K. Jones, and J. Dobson. Applications of magnetic nanoparticles in biomedicine. J Phys D: Appl Phys 36, 167-181 (2003).

207. Sanjeev Mariathasan and Denise Monack. Inflammasome adaptors and sensors: intracellular regulators of infection and inflammation. Nature Rev Immunol 7, 31-40 (2007).

208. Jennifer Lund, Ayuko Sato, Shizuo Akira, Ruslan Medzhitov, and Akiko Iwasaki. Toll-like Receptor 9-mediated Recognition of Herpes Simplex Virus-2 by Plasmacytoid Dendritic Cells. J Exp Med 198, 513-520 (2003).

209. Fakhrul Ahsan, Isabel P. Rivas, Mansoor A. Khan, and Ana T. Suarez. Targeting to macrophages: role of physicochemical properties of particulate carriers-liposomes and microspheres-on the phagocytosis by macrophages. J Contr Rel 79, 29-40 (2002).

210. Annabel F. Valledor, Francesc E. Borras, Martin Cullell-Young, and Antonio Celada. Transcription factors that regulate monocyte/macrophage differentiation. J Leukocyte Biol 63, 405-417 (1998).

211. Stephanie L. Constant and Kim Bottomly. Induction of TH1 and TH2 CD4+ T Cell Responses:The Alternative Approaches. Annu Rev Immunol 15, 297-322 (1997).

212. Danielle L. Drayton, Shan Liao, Rawad H. Mounzer, and Nancy H. Ruddle. Lymphoid organ development: from ontogeny to neogenesis. Nature Immunol 7, 344-353 (2006).

213. Arash Komeili. Molecular Mechanisms of Magnetosome Formation. Annu Rev Biochem 76, 351-366 (2007).

214. Masahiro Yamamoto, Kiyoshi Takeda, and Shizuo Akira. TIR domain-containing adaptors define the specificity of TLR signaling. Mol Immunol 40, 861-868 (2004).

215. Fran Balkwill and Alberto Mantovani. Inflammation and cancer: back to Virchow? Lancet 357, 539-545 (2001).

216. Daniel A. Muruve et al.. The inflammasome recognizes cytosolic microbial and host DNA and triggers an innate immune response. Nature 452, 103-107 (2008).

217. Martin Lundqvist et al.. Nanoparticle size and surface properties determine the protein corona with possible implications for biological impacts. PNAS 105, 14265-14270 (2008).

218. Ajay K. Gupta and Mona Gupta. Cytotoxicity suppression and cellular uptake enhancement of surface modified magnetic nanoparticles. Biomaterials 26, 1565-1573 (2005).

219. Yong Zhang, Nathan Kohler, and Miqin Zhang. Surface modification of superparamagnetic magnetite nanoparticles and their intracellular uptake. Biomaterials 23, 1553-1561 (2002).

220. A. Ito, M. Shinkai, H. Honda, and T. Kobayashi. Medical application of functionalized magnetic nanoparticles. J Biosci Bioeng 100, 1-11 (2005).

221. David E. Sosnovik and Ralph Weissleder. Emerging concepts in molecular MRI. Curr Opin Biotechn 18, 4-10 (2007).

222. Christof M. Niemeyer. Nanoparticles, Proteins, and Nucleic Acids: Biotechnology, Meets Materials Science. Angew Chem Int Ed 40, 4128-4158 (2001).

223. Veronica I. Shubayev, Thomas R. Pisanic, and Sungho Jin. Magnetic nanoparticles for theragnostics. Advanced Drug Delivery Reviews 61, 467-477 (2009).

224. Bruno G. de Geest, Niek N. Sanders, Gleb B. Sukhorukov, Joseph Demeester, and Stefaan C. de Smedt. Release mechanisms for polyelectrolyte capsules. Chem Soc Rev 36, 636-649 (2007).

225. Loretta L. del Mercato et al.. LbL multilayer capsules: recent progress and future outlook for their use in life sciences. Nanoscale 2, 458-467 (2010).

226. Georgina K.Such, Angus P.R. Johnston, and Frank Caruso. Engineered hydrogen-bonded polymer multilayers: from assembly to biomedical applications. Chem Soc Rev 40, 19-29 (2011).

227. Mara L. Macdonald et al.. Tissue integration of growth factor-eluting layer-by-layer polyelectrolyte multilayer coated implants. Biomaterials 32, 1446-1453 (2011).

228. Loretta L. del Mercato, Azhar Z. Abbasi, and Wolfgang J. Parak. Synthesis and Characterization of Ratiometric Ion-Sensitive Polyelectrolyte Capsules. Small 7, 351-363 (2011).

229. Stefaan Derveaux et al.. Layer-by-Layer Coated Digitally Encoded Microcarriers for Quantification of Proteins in Serum and Plasma. Anal Chem 80, 85-94 (2008).

230. Amy Sexton et al.. A Protective Vaccine Delivery System for In Vivo T Cell Stimulation Using Nanoengineered Polymer Hydrogel Capsules. ACS Nano 3, 3391-3400 (2009).

231. Jianjun Cheng et al.. Formulation of functionalized PLGA-PEG nanoparticles for in vivo targeted drug delivery. Biomaterials 28, 869-876 (2007).

232. Andre Scheffel et al.. An acidic protein aligns magnetosomes along a filamentous structure in magnetotactic bacteria. Nature 440, 110-114 (2006).

233. Shouheng Sun et al.. Polymer Mediated Self-Assembly of Magnetic Nanoparticles. JACS 124, 2884-2885 (2002).

234. Pedro Tartaj, Maria Morales, Sabino Veintemillas-Verdaguer, Teresita Gonzalez-Carreno, and Carlos Serna. The preparation of magnetic nanoparticles for applications in biomedicine. J Phys D: Appl Phys 36, 182-197 (2003).

235. Wei Wu, Quanguo He, and Changzhong Jiang. Magnetic Iron Oxide Nanoparticles: Synthesis and Surface Functionalization Strategies. Nanoscale Res Lett 3, 397-415 (2008).

236. Jeanne Skebo, Christin Grabinski, Amanda Schrand, John Schlager, and Saber Hussain. Assessment of Metal Nanoparticle Agglomeration, Uptake, and Interaction Using High-Illuminating System. Int J Toxicol 26, 135-141 (2007).

237. Liang Chen, Joseph Mccrate, James Lee, and Hao Li. The role of surface charge on the uptake and biocompatibility of hydroxyapatite nanoparticles with osteoblast cells. Nanotechnol 22, 1-10 (2011).

238. Belen Diaz et al.. Assessing Methods for Blood Cell Cytotoxic Responses to Inorganic Nanoparticles and Nanoparticle Aggregates. Small 4, 2025-2034 (2008).

239. Ravi Shukla et al.. Biocompatibility of Gold Nanoparticles and Their Endocytotic Fate Inside the Cellular Compartment: A Microscopic Overview. Langmuir 21, 10644-10654 (2005).

240. Stefaan Soenen, Nele Nuytten, Simon De Meyer, Stefaan De Smedt, and Marcel de Cuyper. High Intracellular Iron Oxide Nanoparticle Concentrations Affect Cellular Cytoskeleton and Focal Adhesion Kinase-Mediated Signaling. Small 6, 832-842 (2010).

241. Jae-Hyun Lee et al.. Artificially engineered magnetic nanoparticles for ultra-sensitive molecular imaging. Mature Medicine 13, 95-99 (2006).

242. H. Ittrich et al.. Labeling of Mesenchymal Stem Cells with Different Superparamagnetic Particles of Iron Oxide and Detectability with MRI at 3T. Fortschr Roentgenstr 177, 1151-1163 (2005).

243. Yoshinori Nagai et al.. Toll-Like Receptors on Hematopoietic Progenitor Cells Stimulate Innate Immune System Replenishment. Immunity 24, 801-812 (2006).

244. Young Jik Kwon, Steaphany M. Standley, Sarah Goh, and Jean Frechet. Enhanced antigen presentation and immunostimulation of dendritic cells using acid-degradable cationic nanoparticles. J Contr Rel 105, 199-212 (2005).

245. Ralph Weissleder, Kimberly Kelly, Eric Yi Sun, Timur Shtatland, and Lee Josephson. Cell-specific targeting of nanoparticles by multivalent attachment of small molecules. Nature Biotech 23, 1418-1423 (2005).

246. Dirk Baumjohann et al.. In vivo magnetic resonance imaging of dendritic cell migration into the draining lymph nodes of mice. Eur J Immunol 36, 2544-2555 (2006).

247. E.T. Ahrens, M. Feili-Hariri, H. Xu, G. Genove, and P.A. Morel. Receptor-Mediated Endocytosis of Iron-Oxide Particles Provides Efficient Labeling of Dendritic Cells for In Vivo MR Imaging. Magn Reson Med 49, 1006-1013 (2003).

248. Saho Kobukai et al.. Magnetic Nanoparticles for Imaging Dendritic Cells. Magn Reson Med 63, 1383-1390 (2010).

249. Frank Alexis, Eric Pridgen, Linda Molnar, and Omid Farokhzad. Factors Affecting the Clearance and Biodistribution of Polymeric Nanoparticles. Mol Pharma 5, 505-515 (2008).

250. L. Zhang et al.. Nanoparticles in Medicine: Therapeutic Applications and Developments. Clin Pharma Therap 83, 761-769 (2008).

251. S. Moein Moghimi, A. Christy Hunter, and J. Clifford Murray. Long-Circulating and Target-Specific Nanoparticles: Theory to Practice. Pharma Res 53, 283-318 (2001).

252. C. Chouly, D. Pouliquen, I. Lucet, J.J. Jeune, and P. Jallet. Development of superparamagnetic nanoparticles for MRI : effect of particle size, charge and surface nature on biodistribution. J Microencaps 13, 245-255 (1996).

253. S.M. Moghimi and J. Szebeni. Stealth liposomes and long circulating nanoparticles: critical issues in pharmacokinetics, opsonization and protein-binding properties. Progr Lipid Res 42, 463-478 (2003).

254. Kwangjae Cho, Xu Wang, Shuming Nie, Zhuo Chen, and Dong M. Shin. Therapeutic Nanoparticles for Drug Delivery in Cancer. Clin Cancer Res 14, 1310-1316 (2008).

255. Ariel Savina and Sebastian Amigorena. Phagocytosis and antigen presentation in dendritic cells. Immu Rev 219, 143-156 (2007).

256. C. Wilhelm et al.. Intracellular uptake of anionic superparamagnetic nanoparticles as a function of their surface coating. Biomaterials 24, 1001-1011 (2003).

257. Jayanth Panyam and Vinod Labhasetwar. Dynamics of Endocytosis and Exocytosis of Poly(D,L-Lactide-co-Glycolide) Nanoparticles in Vascular Smooth Muscle Cells. Pharma Res 20, 212-220 (2003).

258. M. Srinivas et al.. Imaging of cellular therapies. Advanced Drug Delivery Reviews 62, 1080-1093 (2010).

259. Mathias Hoehn, Uwe Himmelreich, Klaus Kruttwig, and Dirk Wiedermann. Molecular and Cellular MR Imaging: Potentials and Challenges for Neurological Applications. J Magn Res Imaging 27, 941-954 (2008).

260. Erik M. Shapiro et al.. MRI detection of single particles for cellular imaging. PNAS 101, 10901-10906 (2004).

261. Hyon Bin Na, In Chan Song, and Taeghwan Hyeon. Inorganic Nanoparticles for MRI Contrast Agents. Adv Mat 21, 2133-2148 (2009).

262. Willem J.M. Mulder, Gustav J. Strijkers, Geralda A.F. van Tilborg, Arjan W. Griffioen, and Klaas Nicolay. Lipid-based nanoparticles for contrast-enhanced MRI and molceular imaging. NMR in Biomedicine 19, 142-164 (2006).

263. Mark Allen et al.. Paramagnetic viral nanoparticles as potential high-relaxivity magnetic resonance contrast agents. Magn Reson Med 54, 807-812 (2005).

264. Karolina Palucka, Jacques Banchereau, and Ira Mellman. Designing Vaccines Based on Biology of Human Dendritic Cell Subsets. Immunity 33, 464-478 (2010).

265. U.Himmelreich et al.. A responsive MRI contrast agent to monitor functional cell status. NeuroImage 32, 1142-1149 (2006).

266. Stacey L. Demento et al.. Inflammasome-activating nanoparticles as modular systems for optimizing vaccine efficacy. Vaccine 27, 3013-3021 (2009).

6 Appendix

6.1 Abbreviations

7-AAD	7-Amino-Actinomycin D
APC	Antigen-Presenting cell
APC	AlloPhycoCyanin
ASC	Apoptosis-associated Speck-like protein containing a CARD
BCR	B-Cell Receptor
B_x	Magnetic field
CCL	CC-chemokine Ligand
CCR	CC-chemokine Receptor
CD	Cluster of Differentiation
cDC	conventional Dendritic Cell
CDP	Common DC Precursor
CFSE	CarboxyFluoresceine diacetate Succinimidyl Ester
Chit	Chitosan
CLR	C-type Lectin Receptor
CME	Clathrin-Mediated Endocytosis
CNR	Contrast to Noise Ratio
CT	Computed Tomography
DAMP	Danger-Associated Molecular Pattern
DC	Dendritic Cell
dd	double distilled
Dex	Dextran
D_h	Hydrodynamic diameter
DMEM	Dulbecco's Modified Eagle Medium (culturing medium)
DNA	Deoxy-Ribonucleic Acid
DTPA	Di-ethylene-Tri-amine-Pent-Acetate
ELISA	Enzyme-Linked Immunosorbent Assay
ER	Endoplasmatic Reticulum
EtOH	Ethanol
FACS	Fluorescence Activated Cell Sorting
Fc	Fragment crystallizable
FCS	Fetal Calf Serum

Fe	Iron
Fe_3O_4	Magnetite
FI	Fluorescence Intensity
FITC	Fluorescein-Iso-Thio-Cyanate
Flt3	FMS-Like Tyrosine kinase 3
Gd	Gadolinium
GM-CSF	Granulocyte Macrophage Colony-Stimulating Factor
h	Plank's constant
HSC	Hematopoietic Stem Cell
I	Nuclear spin angular momentum
iDC	inflammatory Dendritic Cell
IFN	Interferon
Ig	Immunoglobulin
IGF	Insulin-like Growth Factor
IL	InterLeukin
iNOS	inducible Nitric Oxide Synthase
k	Boltzmann constant
ko	Knockout
LbL	Layer-by-Layer
LC	Langerhans Cell
LP	Lymphoid Precursor
LPS	Lipo-Poly-Saccharide
M	Net magnetization vector
MBL	Mannose-Binding Lectin
M-CSF	Macrophage Colony-Stimulating Factor
MDP	Monocyte, macrophage and DC Precursor
MHC	Major Histocompatibility Complex
MION	Monocrystalline Iron Oxide Nanoparticles
MNP	Magnetic NanoParticle
MP	Myeloid Precursor
MR	Mannose Receptor
MRI	Magnetic Resonance Imaging
MTT	3-(4,5-Dimethylthiazol-2-yl)-2,5-diphenyltetrazoliumbromide (dye)
MyD88	Myeloid Differentiation primary response 88
NALP	NACHT, LRR and PYD domains-containing protein

NFκB	nuclear factor kappa B
NK cell	Natural Killer cell
NLR	NOD-Like Receptor
NO	Nitric Oxide
OLS	Oleate-Stabilized Shell
PAMP	Pathogen-Associated Molecular Pattern
PBS	Phosphate Buffered Saline
PDAD	Poly-DiAllyl-Dimethyl ammonium chloride
pDC	plasmacytoid Dendritic Cell
PE	PhycoErythrin
PEG	Poly-Ethylene-Glycol
PEI	Poly-Ethylene-Imine
PET	Positron Emission Tomography
PRR	Pattern Recognition Receptor
PSS	Poly-Styrene-Sulfonate
R	Relaxivity
RES	Reticulo-Endothelial System
RIG	Retinoic acid-Inducible Gene
RLH receptor	RIG-I-Like RNA Helicase receptor
RLR	RIG-I-Like Receptor
ROI	Region Of Interest
ROS	Reactive Oxygen Species
RPMI	Roswell Park Memorial Institute (culturing medium)
RT	Room Temperature
SCF	Stem Cell Factor
SDF	Stromal cell-derived factor
SPECT	Single Photon Emission Computed Tomography
SPIO	Small Particles of Iron Oxide
SR	Scavenger Receptor
T	Tesla
T1	Spin-lattice relaxation
T2	Spin-spin relaxation
TCR	T-Cell Receptor
TE	Echo Time
TEM	Transmission Electron Microscopy

TIR	Toll/Interleukin-1 Receptor
TLR	Toll-Like Receptor
TNF	Tumor Necrosis Factor
TR	Relaxation Time
TRIF	TIR-domain-containing adapter-Inducing IFN-β
USPIO	Ultra-Small Particles of Iron Oxide
v/v	Volume/volume
VDJ	Variable, Diversity, Joining
Wt	Wildtype
γFe_2O_3	Maghemite
ζ	Zeta potential
ω	Larmor frequency

6.2 List of Tables and Figures

Introduction

Figure 1.1 Physical principle of MRI relaxation 4
Figure 1.2 Developmental pathways originating from HSCs 7
Figure 1.3 Graphical depiction of terminally differentiated immune cells of both innate and adaptive immunity 9
Figure 1.4 Origin and differentiation capacity of bone marrow derived monocytes 11
Figure 1.5 Endocytic pathways of extracellular particle uptake 17
Figure 1.6 PRRs and their intracellular signaling mechanisms 19
Figure 1.7 Components comprising the Nano-bio interface 21

Results

Figure 3.1 Biocompatibility studies of MNP formulations using HSCs 46
Figure 3.2 Quantitative and qualitative uptake studies employing poly-electrolyte MNPs 47
Figure 3.3 Histological iron staining of MNP labeled HSCs 48
Figure 3.4 Phenotypical FACS analysis of MNP-pulsed HSCs 49
Figure 3.5 *In vitro* MRI phantom studies using MNP-labeled HSCs 51
Figure 3.6 Numerical evaluation of *in vitro* MRI phantom studies using MNP-labeled HSCs 52
Figure 3.7 Cytotoxic effects of various poly-electrolyte MNP concentrations on inflammatory DCs (iDCs) 55
Figure 3.8 Uptake properties of MNPs into iDCs 56
Figure 3.9 Histological stainings of cytospins after magnetic separation 57
Figure 3.10 Transmission electron microscopy (TEM) studies of MNP-labeled inflammatory DCs 58
Figure 3.11 Phenotypical surface marker profiling of labeled GM-CSF derived iDCs 59
Figure 3.12 *In vitro* migration assay in the context of MyD88 adaptor protein knockout mice 61
Figure 3.13 Relaxometry data of *in vitro* phantom studies 62
Figure 3.14 *In vitro* MRI detection limits and SNR ratios 63
Figure 3.15 FACS gating strategy of Flt3L generated conventional DCs (cDCs) 64
Figure 3.16 FACS profiling of Flt3L generated cDCs in the context of TLR receptor knockout mice 65
Figure 3.17 FACS gating strategy of Flt3L generated plasmacytoid DCs (pDCs) 66
Figure 3.18 FACS profiling of Flt3L generated pDCs in the context of receptor knockout models 67
Figure 3.19 Cytokine secretion of poly-electrolyte MNP-stimulated bulk DC generated using Flt3L 68
Figure 3.20 FACS gating strategy of M-CSF generated macrophages 70

Figure 3.21 FACS profiling of macrophages stimulation with poly-electrolyte MNPs in the context of TLR4 receptor knockout cells 71
Figure 3.22 Cytokine secretion of poly-electrolyte MNP-pulsed macrophages in the context of knockout mice 72
Figure 3.23 Mixed splenocyte reactions to evaluate T-cell proliferation capacity following poly-electrolyte MNP stimulation 74
Figure 3.24 Biocompatibility studies of MSR-1 MNP using HSCs 75
Figure 3.25 Quantitative and qualitative MNP uptake studies into HSCs 76
Figure 3.26 Phenotypical FACS analysis of MSR-1 pulsed HSCs 77
Figure 3.27 *In vitro* MRI studies using MSR-1 labeled HSCs 78
Figure 3.28 GM-CSF derived iDC uptake of bacterial MSR-1 magnetosomes 79
Figure 3.29 Phenotypic FACS gating strategy of GM-CSF derived inflammatory DC populations 80
Figure 3.30 Phenotypic FACS profiling of GM-CSF derived iDC populations employing bacterial MSR-1 magnetosomes 81
Figure 3.31 *In vitro* migration assay in the context of MyD88 adaptor protein knockout mice 82
Figure 3.32 FACS profiling of Flt3L generated cDCs in the context of TLR receptor and adaptor knockout mice 83
Figure 3.33 FACS profiling of Flt3L generated pDCs in the context of receptor knockout models 84
Figure 3.34 Cytokine secretion of MSR-1 stimulated bulk DCs 85
Figure 3.35 FACS profiling of macrophages in the context of TLR4 receptor knockout cells 86
Figure 3.36 Cytokine secretion of MNP-pulsed macrophages in the context of receptor knockout mice 87
Figure 3.37 Mixed splenocyte reactions to evaluate T-cell proliferation capacity of bacterial MSR-1 MNPs 88
Figure 3.38 Secreted IL-1ß and corresponding IL-6 and TNFα inflammatory cytokine levels of macrophages stimulated with bacterial magnetosome MSR-1 as an indication of the inflammasome pathway 89
Figure 3.39 Uptake properties of covalently linked “stealth” MNPs into GM-CSF derived iDCs 91
Figure 3.40 Phenotypic FACS profiling of GM-CSF derived iDC populations of covalently linked “stealth” MNPs 93
Figure 3.41 FACS profiling of Flt3L generated cDCs in the context of TLR receptor knockout mice 94
Figure 3.42 FACS profiling of Flt3L generated pDCs in the context of receptor knockout models 95
Figure 3.43 Cytokine secretion of “stealth” MNP-stimulated bulk DCs 96
Figure 3.44 FACS profiling of “stealth” MNP-pulsed macrophages in the context of TLR4 receptor knockout cells 97

Figure 3.45 Cytokine secretion of MNP-pulsed macrophages in the context of receptor knockout mice 98
Figure 3.46 Mixed splenocyte reactions to evaluate T-cell proliferation capacity of "stealth" MNPs employed 99
Figure 3.47 Influence of serum protein content on uptake properties of various MNPs into iDCs 100
Figure 3.48 Influence of serum proteins on intracellular iron concentration of various MNPs in iDCs 101
Figure 3.49 Influence of serum proteins on MRI properties of various MNP formulations within inflammatory iDCs 102
Figure 3.50 Concept of functionalized acrylated MNPs (acMNP) using CpG motifs linked to MNP surface moieties 104
Figure 3.51 Cytokine secretion of functionalized acMNPs using CpG motifs linked to MNP surface moieties 105

Table 3.1 Summary table of MNPs and their designed shell structures 42
Table 3.2 Physico-chemical characterization of MNP formulations 43
Table 3.3 Relaxation properties of MNPs 53

6.3 Scientific Publications and Presentations

Scientific Publications

Schwarz S., Fernandes F., Sanroman L., Hodenius M., Lang C., Himmelreich U., Schmitz-Rode T., Schueler D., Hoehn M., Zenke M., Hieronymus T..
Synthetic and biogenic magnetite nanoparticles for tracking of stem cells and dendritic cells.
J. Magn. Magn. Mater., 321, 1533-1538, 2009.

Schwarz S., Wong J.E., Bornemann J., Hodenius M., Himmelreich U., Richtering W., Hoehn M., Zenke M., Hieronymus T..
Polyelectrolyte coating of iron oxide nanoparticles for MRI-based cell tracking.
Nanomedicine: Nanotechnology, Biology and Medicine, epub ahead of print, 2011.

Poster Presentations

J. E. Wong, **S. Schwarz**, T. Hieronymus, M. Zenke, W. Richtering.
Influence of surface charge, size and functionality of magnetic nanoparticles on cell interaction.
4th Zsigmondy Colloquium, April 3-4, Essen, Germany, 2008.

J. E. Wong, **S. Schwarz**, T. Hieronymus, M. Zenke, W. Richtering.
Influence of surface charge, size and functionality of magnetic nanoparticles on cell interaction.
7th International Symposium on Polyelectrolytes, July 16-19, Coimbra, Portugal, 2008.

Schwarz S., Fernandes F., Sanroman L., Hodenius M., Lang C., Himmelreich U., Schmitz-Rode T., Schueler D., Hoehn M., Zenke M. and Hieronymus T..
Synthetic and biogenic magnetite nanoparticles for tracking of stem cells and dendritic cells.
10th International Symposium on Dendritic Cells, Oct 1-5, Kobe, Japan, 2008.

Schwarz S., Lang C., Wong J.E., Hodenius M., Richtering W., Schueler D., Hoehn M., Zenke M., Hieronymus T..
Influence of engineered magnetic nanoparticles on hematopoietic stem cells.
5th International Meeting Stem Cell Network NRW, March 24-25, Aachen, Germany, 2009.

Schwarz S., Lang C., Wong J.E., Hodenius M., Schueler D., Richtering W., Hoehn M., Zenke M., Hieronymus T..
MRI-tracking and phenotypic analysis of magnetic nanoparticle-pulsed dendritic cells.
World Congress – Medical Physics and Biomedical Engineering, Sept 7-12, Munich, Germany, 2009.

J.E. Wong, **S. Schwarz**, M. Zenke, T. Hieronymus, W. Richtering.
Polyelectrolyte-modified magnetic nanoparticles: influence of surface charge, size and functionality on dendritic cells.
23rd Conference of the European Colloid and Interface Society (ECIS2009), Sept 6-11, Antalya, Turkey, 2009.

J.E. Wong, **S. Schwarz**, M. Zenke, T. Hieronymus, W. Richtering.
Influence of polyelectrolyte-modified nanoparticles on Hematopoietic stem cells.
44th Biennial Meeting of the German Colloid Society, Sept 28-30, University of Hamburg, Germany, 2009.

Schwarz S., Kießling F., Wong J.E., Richtering W., Zenke M., Hieronymus T..
Labeling of Stem Cells and Immune Cells with Functionalized Iron-Oxide Nanoparticles for in vivo Cell Tracking.
1st Day of Medical Research, Dec 11, Aachen, Germany, 2009.

Schwarz S., Fahrenkamp D., Wong J.E., Hodenius M., Richtering W., Hoehn M., Zenke M., Hieronymus T..
Engineered Nanoparticles as Contrast Agents for Magnetic Resonance Imaging of Dendritic Cells.
Biomedica – Life Science Summit 2010, March 17-18, Aachen, Germany, 2010.

Oral Presentations

Magnetic Nanoparticles and Smart Contrast Agents for Tracking Dendritic Cells using MRI.
BMT 2007 – Annual Meeting Association of Biomedical Technologies, Sept 26-29, Aachen, Germany, 2007.

Nanoparticle Size and Surface Charge Determine Formation of Protein Corona, Cellular Uptake and Magnetic Resonance Imaging Properties.
8th International Conference on the Scientific and Clinical Applications of Magnetic Carriers, May 25-29, Rostock, Germany, 2010.

Acknowledgements

I would like to express my gratitude to Professor Martin Zenke, who provided me with the opportunity to work in the Institute for Biomedical Engineering (IBMT) at the RWTH Aachen. Furthermore, I wish to convey my appreciation to Dr. Thomas Hieronymus, the group leader of the "Nanoparticle and Imaging" group within IBMT, for his supervision and scientific insights. In addition, I am very grateful to Professor Wilhelm Jahnen-Dechent and Professor Walter Richtering for being members of my PhD committee.

In addition, I would like to thank Andrea Offergeld, who provided support in so many different ways! Thank you for your patience Andrea!

Furthermore, I would like to thank the following people involved in the study at hand:

Professor Mathias Hoehn from the MPI for Neurological Research in Cologne for giving me the amazing opportunity to perform MRI experiments in his Institute. I owe deepest gratitude to the members of his lab for giving me advice and teaching me the miracles of MRI. Especially Therese, Chrystelle, Jörg, Philipp, Markus, Tracy, and Daniel made my regular scientific visits successful.
In addition, I would like to thank Professor Uwe Himmelreich for his continuous support during experimental procedures as well as his amazing scientific input throughout these studies.

I owe special thanks to Prof. Shizuo Akira, Head of the World Premier Institute (WPI) Immunological Frontiers Research Center (IFReC) in Osaka, Japan, who gave me the opportunity to work in his institute for a period of six months as part of my PhD thesis. In that context, I would like to thank Dr. Ken Ishii and Dr. Cevayir Coban for their supervision and fruitful scientific discussions. Especially, I owe sincere gratitude to Prof. Yoshichika Yoshioka, Head of the Biofunctional Imaging Group within IFReC. He inspired me in so many ways during our scientific conversations and I have the utmost respect for his dedication and personality.

Martina Tappe and Beate Kratz from the IZKF Core Facilities of the RWTH University clinic for their scientific advice and guidance.

Dr. Jörg Bornemann and Hiltrud Königs from the TEM Facility of the Institute of Pathology at the RWTH Aachen for their scientific input and discussions related to the publications that resulted from this work.

Professor Fabian Kiessling and members of his Institute for fruitful scientific discussions and research. Especially Jabadurai Jayapaul for our scientific discussions and experimental strategies.

Professor Walter Richtering and Dr. Erik Wong from the Institute of Physical Chemistry at the RWTH Aachen for the synthesis and characterization of poly-electrolyte MNPs employed in this study. Furthermore, I would like to thank Ingeborg Tomulla for administrative support within the IZKF project.

Dr. Michael Hodenius from the Institute of Applied Medical Engineering (AME) at RWTH Aachen (formerly) for the synthesis and characterization of lipid-shell MNPs.

Professor Dirk Schueler, Claus Lang and Anna Lohsse from the "Magnetolab" at the LMU Munich for extracting bacterial magnetosomes. Special "thank you" goes out to Anna for her patience in our scientific discussions and her never-ending biological interest and dedication.

Professor Erik Reimhult and Dr. Esther Amstad from the ETH Zuerich (formerly) for synthesizing and optimizing the covalently linked MNPs and functionalizable particles on the basis of Nitro-DOPA employed in this study. Especially, I owe deepest gratitude to Esther for our insightful discussions on the subject.

Claudia and Stefan from the Kinderklinik and the Tissue Engineering group of the AME Institute at the RWTH Aachen, respectively. They brightened up the darkest day, especially during my isolated stay in Japan. Thank you so much for that!

A special "thank you" goes out to former members of IBMT, especially Ivonne, Piritta, Rebekka, Julia, Yea-Hyun, Nick, and David. Thank you for your friendship, good times and mental support during rough patches that we all encountered during our PhD!

Furthermore, I would like to thank all other lab members that I did not mention explicitly for their efforts to make IBMT a better place, both related to work itself as well as the working environment.

Last but not least, I would like to thank my family and closest friends: Especially my parents, Jörg, Lars, Ria, Moritz, Elena and Daniela for the patient listening to my complaints and their never-ending support in so many ways.

Thank you all!

Eidesstaatliche Erklärung

Hiermit erkläre ich, Sebastian Schwarz, an Eides statt, dass ich die vorliegende wissenschaftliche Dissertation selbständig verfasst und keine anderen als die angegebenen Quellen und Hilfsmittel benutzt habe. Jegliche Ausführungen, die anderen Schriften wörtlich oder sinngemäß entnommen wurden, sind als solche kenntlich gemacht. Die vorliegende Arbeit ist in gleicher oder ähnlicher Fassung noch nicht Bestandteil einer wissenschaftlichen Veröffentlichung oder ähnlicher Promotionsleistung gewesen.

Ich versichere außerdem, dass ich die beigefügte Dissertation nur in diesem und keinem anderen Promotionsverfahren eingereicht habe, und dass diesem Promotionsverfahren keine endgültig gescheiterten Promotionsverfahren vorausgegangen sind.

Darüber hinaus bestätige ich hiermit, dass mir die geltende Promotionsordnung der Fakultät für Mathematik, Informatik und Naturwissenschaften der RWTH Aachen University bekannt ist.

Aachen, den 05.12.2012

Sebastian Schwarz